



AFRL-OSR-VA-TR-2015-0141

---

## INTERACTIONS OF ULTRACOLD IMPURITY PARTICLES WITH BOSE-EINSTEIN CONDENSATES

Georg Raithel  
UNIVERSITY OF MICHIGAN

---

06/23/2015  
Final Report

DISTRIBUTION A: Distribution approved for public release.

Air Force Research Laboratory  
AF Office Of Scientific Research (AFOSR)/ RTB  
Arlington, Virginia 22203  
Air Force Materiel Command

REPORT DOCUMENTATION PAGE				Form Approved OMB No. 0704-0188	
<p>The public reporting burden for this collection of information is estimated to average 1 hour per response, including the time for reviewing instructions, searching existing data sources, gathering and maintaining the data needed, and completing and reviewing the collection of information. Send comments regarding this burden estimate or any other aspect of this collection of information, including suggestions for reducing the burden, to the Department of Defense, Executive Service Directorate (0704-0188). Respondents should be aware that notwithstanding any other provision of law, no person shall be subject to any penalty for failing to comply with a collection of information if it does not display a currently valid OMB control number.</p> <p><b>PLEASE DO NOT RETURN YOUR FORM TO THE ABOVE ORGANIZATION.</b></p>					
1. REPORT DATE (DD-MM-YYYY) 09/06/2015		2. REPORT TYPE Final		3. DATES COVERED (From - To) 8/15/2010-2/14/2015	
4. TITLE AND SUBTITLE Interactions of ultracold impurity particles with Bose-Einstein Condensates				5a. CONTRACT NUMBER FA9550-10-1-0453	
				5b. GRANT NUMBER	
				5c. PROGRAM ELEMENT NUMBER	
6. AUTHOR(S) Georg Raithel				5d. PROJECT NUMBER	
				5e. TASK NUMBER	
				5f. WORK UNIT NUMBER	
7. PERFORMING ORGANIZATION NAME(S) AND ADDRESS(ES) University of Michigan, Randall Lab, 450 Church Street, Ann Arbor, MI 48109				8. PERFORMING ORGANIZATION REPORT NUMBER	
9. SPONSORING/MONITORING AGENCY NAME(S) AND ADDRESS(ES) AFOSR				10. SPONSOR/MONITOR'S ACRONYM(S)	
				11. SPONSOR/MONITOR'S REPORT NUMBER(S)	
12. DISTRIBUTION/AVAILABILITY STATEMENT					
13. SUPPLEMENTARY NOTES					
14. ABSTRACT Research on interactions between quantum gases and impurities has become an active area of AMO. Here, two setups have been constructed and operated towards these goals. In the first, a metal tip (diameter 125 microns) is mounted close to a magneto-optic trap (MOT). Rydberg excitations are implanted in a cold-atom region (diameter about 10 microns, length about 50 microns). Interactions between the excitations cause excitation blockades, short- and medium-range order, as well as dynamics due to van-der-Waals interaction. All these topics were studied. The second setup is a double-trap system, in which magnetically trapped rubidium atom samples are prepared between 1 and 10 micro-Kelvin temperature and densities of about $10^{12} \text{ cm}^{-3}$ . Cold circular Rydberg atoms have been prepared and trapped. The dynamics of these highly dipolar atoms in the magnetic trap was studied, and collision-induced loss was observed and traced back to collisions between the long-lived circular atoms and cold ground state atoms. Novel D-type molecules between Rydberg and ground-state atoms were realized. These molecules are due to an attractive triplet s-wave low-energy electron scattering interaction. Five papers were published [two Phys. Rev. Lett, 2 Phys. Rev. A] and one submitted to PRL.					
15. SUBJECT TERMS					
16. SECURITY CLASSIFICATION OF:			17. LIMITATION OF ABSTRACT	18. NUMBER OF PAGES	19a. NAME OF RESPONSIBLE PERSON
a. REPORT	b. ABSTRACT	c. THIS PAGE			19b. TELEPHONE NUMBER (Include area code)

Reset

## INSTRUCTIONS FOR COMPLETING SF 298

**1. REPORT DATE.** Full publication date, including day, month, if available. Must cite at least the year and be Year 2000 compliant, e.g. 30-06-1998; xx-06-1998; xx-xx-1998.

**2. REPORT TYPE.** State the type of report, such as final, technical, interim, memorandum, master's thesis, progress, quarterly, research, special, group study, etc.

**3. DATES COVERED.** Indicate the time during which the work was performed and the report was written, e.g., Jun 1997 - Jun 1998; 1-10 Jun 1996; May - Nov 1998; Nov 1998.

**4. TITLE.** Enter title and subtitle with volume number and part number, if applicable. On classified documents, enter the title classification in parentheses.

**5a. CONTRACT NUMBER.** Enter all contract numbers as they appear in the report, e.g. F33615-86-C-5169.

**5b. GRANT NUMBER.** Enter all grant numbers as they appear in the report, e.g. AFOSR-82-1234.

**5c. PROGRAM ELEMENT NUMBER.** Enter all program element numbers as they appear in the report, e.g. 61101A.

**5d. PROJECT NUMBER.** Enter all project numbers as they appear in the report, e.g. 1F665702D1257; ILIR.

**5e. TASK NUMBER.** Enter all task numbers as they appear in the report, e.g. 05; RF0330201; T4112.

**5f. WORK UNIT NUMBER.** Enter all work unit numbers as they appear in the report, e.g. 001; AFAPL30480105.

**6. AUTHOR(S).** Enter name(s) of person(s) responsible for writing the report, performing the research, or credited with the content of the report. The form of entry is the last name, first name, middle initial, and additional qualifiers separated by commas, e.g. Smith, Richard, J, Jr.

**7. PERFORMING ORGANIZATION NAME(S) AND ADDRESS(ES).** Self-explanatory.

**8. PERFORMING ORGANIZATION REPORT NUMBER.** Enter all unique alphanumeric report numbers assigned by the performing organization, e.g. BRL-1234; AFWL-TR-85-4017-Vol-21-PT-2.

**9. SPONSORING/MONITORING AGENCY NAME(S) AND ADDRESS(ES).** Enter the name and address of the organization(s) financially responsible for and monitoring the work.

**10. SPONSOR/MONITOR'S ACRONYM(S).** Enter, if available, e.g. BRL, ARDEC, NADC.

**11. SPONSOR/MONITOR'S REPORT NUMBER(S).** Enter report number as assigned by the sponsoring/monitoring agency, if available, e.g. BRL-TR-829; -215.

**12. DISTRIBUTION/AVAILABILITY STATEMENT.** Use agency-mandated availability statements to indicate the public availability or distribution limitations of the report. If additional limitations/ restrictions or special markings are indicated, follow agency authorization procedures, e.g. RD/FRD, PROPIN, ITAR, etc. Include copyright information.

**13. SUPPLEMENTARY NOTES.** Enter information not included elsewhere such as: prepared in cooperation with; translation of; report supersedes; old edition number, etc.

**14. ABSTRACT.** A brief (approximately 200 words) factual summary of the most significant information.

**15. SUBJECT TERMS.** Key words or phrases identifying major concepts in the report.

**16. SECURITY CLASSIFICATION.** Enter security classification in accordance with security classification regulations, e.g. U, C, S, etc. If this form contains classified information, stamp classification level on the top and bottom of this page.

**17. LIMITATION OF ABSTRACT.** This block must be completed to assign a distribution limitation to the abstract. Enter UU (Unclassified Unlimited) or SAR (Same as Report). An entry in this block is necessary if the abstract is to be limited.

## **Subject: Final Report**

Contract/Grant Title: Interactions of ultracold impurity particles with Bose-Einstein Condensates

Contract/Grant #: FA9550-10-1-0453

Reporting Period: 8/15/2010 to 2/14/2015

### **Abstract.**

Research on interactions between quantum gases and impurities (ions, other atoms etc.) has become an active area of AMO research over the past couple of years. Among the topics of interest one finds the formation of mesoscopic ions, charge hopping and quantum transport, self trapping of impurities in Bose-Einstein Condensate (BECs), and the effect of impurity particles on the BEC density distribution. To study ion-BEC interactions, a method must be used that allows one to hold a cold ion in a BEC for a sufficiently long time that these phenomena become observable, in a way that does not heat the ion.

In the project two setups have been constructed and operated towards these goals. In the first, more basic one, a metal tip (diameter 125 microns) is mounted close to a magneto-optic trap (MOT). Rydberg excitations are implanted in a cold-atom region (diameter about 10 microns, length about 50 microns). Interactions between the excitations cause excitation blockades, short- and medium-range order, as well as dynamics due to van-der-Waals interaction. All these topics have been studied. Two papers were published [one PRL, one PRA, one submitted to PRL].

The second setup is a double-trap system, in which we prepare magnetically trapped rubidium atom samples between 1 and 10 micro-Kelvin and densities of about  $10^{12} \text{ cm}^{-3}$ . We have prepared and trapped, for the first time, cold circular Rydberg atoms in these traps. In addition to being able to study the dynamics of these highly dipolar atoms in the magnetic trap, we also observed a collision-induced loss we have traced back to collisions between the long-lived circular atoms and cold ground state atoms. These types of collisions are unexplored, to date. In this setup we also have prepared and studied D-type molecules between Rydberg and ground-state atoms. These are due to an attractive triplet s-wave low-energy scattering interaction between the Rydberg electron and a ground-state atom. We have published two papers, one in PRL, one in PRA.

### **Archival publications during reporting period (all attached):**

[\* ] "Measurement of van-der-Waals interaction by atom trajectory imaging," N. Thaicharoen, A. Schwarzkopf, and G. Raithel (submitted to Phys. Rev. Lett., June 2015).

[1] "Angular-momentum couplings in long-range Rb<sub>2</sub> Rydberg molecules," D. A. Anderson, S. A. Miller, G. Raithel, Phys. Rev. A **90**, 062518 (2014).

[2] "Photoassociation of long-range nD Rydberg molecules," D. A. Anderson, S. A. Miller, and G. Raithel, Phys. Rev. Lett. **112**, 163201 (2014).

[3] "Spatial correlations between Rydberg atoms in an optical dipole trap," A. Schwarzkopf, D. A. Anderson, N. Thaicharoen, and G. Raithel, Phys. Rev. A **88**, 061406(R) (2013); Editor's suggestion.

[4] "Production and trapping of cold circular Rydberg atoms," D. A. Anderson, A. Schwarzkopf, R. E. Sapiro, and G. Raithel, Phys. Rev. A **88**, 031401 (2013); Editor's suggestion.

[5] "Imaging Spatial Correlations of Rydberg Excitations in Cold Atom Clouds," A. Schwarzkopf, R. E. Sapiro, and G. Raithel, Phys. Rev. Lett. **107**, 103001 (2011).

**Activity (1):** We have imaged spatial correlations of Rydberg excitations in cold atom clouds. We use direct spatial imaging of cold  $85\text{Rb}$  Rydberg atom clouds to measure the Rydberg-Rydberg correlation function. Initially obtained results were in qualitative agreement with theoretical predictions elsewhere. We determined the blockade radius for several D-level Rydberg states and investigated the dependence of the correlation behavior on excitation conditions and detection delay. Experimental data hinted at the existence of long-range order. We then extended the research to include light-shift potentials generated by an optical dipole trap. The optical dipole trap is used to prepare dense ground-state atom samples and to add light-shifts to the ground-Rydberg transition. We studied and interpreted the effects of laser detuning and light-shifts on the Rydberg pair-correlation function. The result showed an enhancement of the probability of exciting two Rydberg atoms at a particular separation distance, which is interpreted as a result of direct two-photon excitation of Rydberg atom pairs. In another experiment, we investigated the effect of the time delay between the excitation pulses and the read-out sequence. We observed a time dependence of the pair-correlation signal which is consistent with the effect of van-der-Waals forces acting between Rydberg-atom pairs. The results are significant because of the wide use of optically trapped Rydberg atoms in both ongoing and in proposed research. **Three papers (one submitted, two published) are attached [\*,3,5].**

**Activity (2):** We have successfully prepared and trapped circular Rydberg atoms. Circular Rydberg atoms exhibit a unique combination of extraordinary properties: long lifetimes ( $\sim n^5$ ), large magnetic moments and angular momenta ( $|m|=l=n-1$ ), and no first order Stark shift. Here,  $n$ ,  $l$  and  $m$  are the principal, orbital and magnetic quantum numbers, respectively. These features have made circular Rydberg atoms attractive for a number of applications. We realized a magnetic trap for laser-cooled Rydberg atoms that are initially in a well-defined circular Rydberg state. The Rydberg-atom trap was characterized using state-selective electric-field ionization, direct spatial imaging of the atom distributions, and time-of-flight analysis of the ion signal. At room temperature, we observed 70 percent of the trapped atoms remaining after 6ms. We measured an enhancement of the center-of-mass trap oscillation frequency by the expected factor of  $\sqrt{m}$ . Simulations of the state-evolution of circular-state atoms in our magnetic trap, held at 300K radiation temperature, were performed and results were in good agreement with the observed phenomena. **One published paper is attached [4].**

**Activity (3):** One of the most prominent recent observations of impurities in dense cold atom clouds is that of Rydberg molecules. A recently discovered class of long-range Rydberg molecules generated through an attractive Fermi potential has generated a significant amount of theoretical and experimental interest. Here, we have observed long-range homonuclear diatomic  $nD$  Rydberg molecules photoassociated out of an ultracold gas of  $87\text{Rb}$  atoms for  $34 < n < 40$ . We measured the ground-state binding energies of  $87\text{Rb}(nD+5S_{1/2})$  molecular states to be larger than those of their  $87\text{Rb}(nS+5S_{1/2})$  counterparts, showing the dependence of the molecular bond on the angular momentum of the Rydberg atom. We probed the transition of  $87\text{Rb}(nD + 5S_{1/2})$  molecules from the molecular-binding-dominant regime at low  $n$  [Hund's cases (a)] to a fine-structure-dominant regime at high  $n$  [Hund's case (c)]. A Fermi model that includes the fine structure of the  $nD$  Rydberg atom and hyper fine structure of the  $5S_{1/2}$  perturber is presented that describes this transition. In ongoing work, we include  $3S$ ,  $3P$ ,  $1S$  and  $1P$  scattering channels for accurate modeling of the molecular spectra. **Two published papers are attached [1,2].**

# Measurement of van-der-Waals interaction by atom trajectory imaging

N. Thaicharoen\*, A. Schwarzkopf†, and G. Raithel

*Department of Physics, University of Michigan, Ann Arbor, MI 48109*

(Dated: June 6, 2015)

We study the repulsive van der Waals interaction of  $70S_{1/2}$  cold rubidium Rydberg atoms by analysis of time-delayed pair correlation functions. After excitation, Rydberg atoms are allowed to accelerate under the influence of the van der Waals force, before measuring their positions using a single-atom imaging technique. From the average pair correlation function of the atom positions we obtain the initial atom-pair separation and the terminal velocity, which yield the van der Waals interaction coefficient  $C_6$ . The measured  $C_6$  value agrees well with calculations. The experimental method has been validated by simulations. The data hint at anisotropy in the overall expansion, caused by the shape of the excitation volume. Our measurement implies that the interacting entities are individual Rydberg atoms, not groups of atoms that coherently share a Rydberg excitation.

PACS numbers: 32.80.Ee, 34.20.Cf

The van der Waals interaction is important in the description and control of interactions in few- and many-body dynamics studies. This interaction has been critical in the observation of Rydberg excitation blockades and collective excitations [1–4], Rydberg crystals [5, 6], and Rydberg aggregates [7, 8]. Rydberg interactions have been used in quantum information processing [9–12]. The van der Waals interaction between two Rydberg atoms has been measured using spectroscopic methods [13, 14]. Several measurements have been performed near surfaces to observe radiative Rydberg-level shifts caused by image charge interaction near metal surfaces [15, 16]. The van der Waals interaction between excited cesium atoms and a dielectric surface has been measured using selective reflection spectroscopy [17].

Here, we develop a method to study the van der Waals interaction between Rydberg atoms using direct spatial imaging of their trajectories [18–21]. Pairs of  $S_{1/2}$  rubidium Rydberg atoms are prepared with a well-defined initial separation by detuning an excitation laser and utilizing the  $r^{-6}$  dependence of the van der Waals interaction [21, 22]. After preparation, the atoms are subject to van der Waals forces (which are repulsive in this case). The effect of the forces is observed by tracking the interatomic distance between the Rydberg atoms, after they have been allowed to move for selected wait times (see Fig. 1). The atom trajectories and thereby the van der Waals interaction coefficient  $C_6$  are extracted from the pair correlation functions of the Rydberg atom positions.

The experimental setup is shown in Fig. 1(a).  $^{85}\text{Rb}$  ground-state atoms are prepared in a magneto-optical trap (MOT) at a density of  $\gtrsim 10^{10} \text{ cm}^{-3}$ . The two-photon Rydberg excitation to  $70S_{1/2}$  is driven by simultaneous 780 nm and 480 nm laser pulses with a 5  $\mu\text{s}$  duration and  $\approx 1$  GHz red-detuning from the  $5P_{3/2}$  intermediate state. Both beams propagate in the  $xy$  plane and are linearly polarized along  $\hat{z}$ . The 780 nm beam has a Gaussian beam parameter  $w_0$  of 0.75 mm and the 480 nm beam is focused to  $w_0 = 8 \mu\text{m}$ . The Rydberg atoms are ionized by applying a high voltage to a tip imaging probe (TIP) with a rounded tip of diameter 125  $\mu\text{m}$ . Ions are

accelerated by the TIP electric field towards a microchannel plate (MCP). Ion impacts result in blips produced by the MCP-phosphor detector assembly, revealing the Rydberg atom positions. In each experimental cycle we record one image, taken by a CCD camera, that typically contains several blips. For more detail see reference [21].

The excitation volume is  $\approx 470 \mu\text{m}$  above the tip, which, in combination with the radial divergence of the TIP electric field and the MCP front voltage, results in a measured magnification of 155 with an uncertainty of 2%. We have calibrated the magnification by projecting a known double-slit interference pattern of 480 nm excitation light into the object plane and measuring the distribution of counts in the image (MCP) plane. The

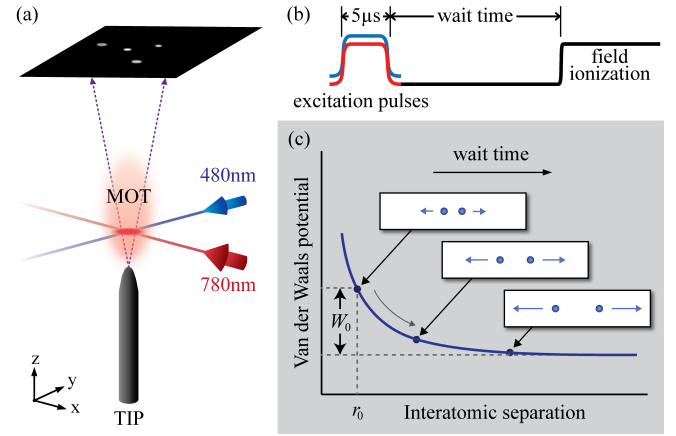


FIG. 1. Geometry (a) and timing sequence (b) of the experiment. The wait time is the time difference between the end of the excitation and the onset of the field ionization pulse. (c) Van der Waals potential versus separation between two Rydberg atoms. The separation increases due to the repulsive van der Waals force. We image the resulting trajectories by varying the wait time. In the insets in (c), circles represent two Rydberg atoms evolving under the influence of the van der Waals force. The kinetic energy release, indicated by the blue velocity arrows, equals the van der Waals potential  $W_0$  at the initial separation  $r_0$ .

magnification uncertainty follows from the variation of the peak positions from an equidistant series (which one would expect for the double-slit). The resolution in the object plane is  $\approx 1 \mu\text{m}$ ; it follows from the magnification and the point spread function of the detector. We can easily resolve the correlation length between the Rydberg atoms, which is on the order of  $10 \mu\text{m}$ . The field of view typically contains 5 to 10 detected atoms. In the image processing sequence, we first extract ion impact positions on the MCP by using a peak detection algorithm [21]. Out of 10000 images taken in each dataset, we select the 5000 images with the highest numbers of detected ions. From this subset, we calculate the average pair correlation image and normalize it such that at large distances it approaches the value of one.

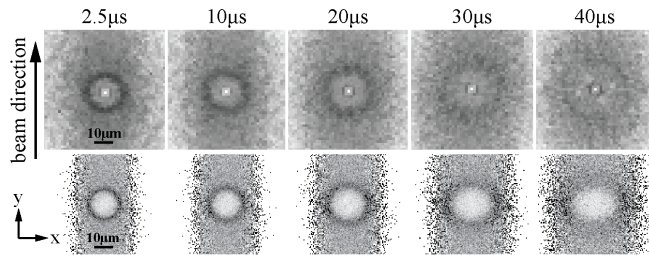


FIG. 2. Pair correlation images from experiment (top row) and simulation (bottom row) for the selected wait times. The linear grayscale ranges from 0 (white) to 2 (black). Values of 1,  $<1$ , and  $>1$  indicate no correlation, anticorrelation, and positive correlation, respectively.

The excitation of the  $70S_{1/2}$  Rydberg level is detuned by  $\delta\nu_L = 4 \pm 2$  MHz with respect to the two-photon resonance. The positive excitation detuning is compensated by the (repulsive) van der Waals interaction. We preferentially excite Rydberg atoms in pairs at a separation at which the van der Waals interaction is  $2\delta\nu_L = 8 \pm 4$  MHz. We determine  $r_0$  from pair-correlation images. After excitation, the Rydberg atoms are allowed to move within selected times before measuring their positions by applying a field ionization pulse [Fig. 1(b)]. The atom-position data are processed as explained above, yielding average pair correlation images. In Fig. 2, we present the pair correlation images for wait times  $2.5 \mu\text{s}$ ,  $10 \mu\text{s}$ ,  $20 \mu\text{s}$ ,  $30 \mu\text{s}$ , and  $40 \mu\text{s}$ . The average interaction time of the Rydberg atoms is the wait time plus half the excitation pulse length (wait time +  $2.5 \mu\text{s}$ ). The pair correlation image at  $2.5 \mu\text{s}$  exhibits strong correlation enhancement at a fairly well-defined radius. The initial correlation is critical for our trajectory experiment; it is sufficient to track Rydberg-pair trajectories out to approximately  $40 \mu\text{s}$ . With increasing wait time, the radius of enhanced pair correlation increases, reflecting an increase of interatomic separation due to the repulsive van der Waals interaction. At long wait times, the enhancement ring is blurred out due to initial thermal atom velocities in the MOT (temperature  $\sim 100 \mu\text{K}$ ).

To determine the most probable separation  $r_p(t)$  be-

tween Rydberg-atom pairs at wait time  $t$ , we first compute the angular integrals  $I(r)$  of the experimental pair correlation images in Fig. 2, as shown in Fig. 3(a). The values of  $r_p(t)$  are obtained from local parabolic fits centered approximately at the peak positions of the  $I(r)$  curves. We include 4 to 7 data points in the fit (depending on the shapes of the curves). The resulting separations  $r_p(t)$  are shown in Fig. 3(b). The visibility of the pair correlation enhancement, also shown in Fig. 3(b), is  $(I_{\text{max}} - I_{\text{min}})/(I_{\text{max}} + I_{\text{min}})$ , where  $I_{\text{max}}$  is the peak value of  $I(r)$  in the range  $\gtrsim 10 \mu\text{m}$  and  $I_{\text{min}}$  is the minimal value near  $7 \mu\text{m}$ . A cursory inspection of Fig. 3(b) already shows that the trajectory of the Rydberg-atom pairs is characterized by an initial acceleration phase, during which the initial van der Waals potential energy,  $W_0$ , is converted into kinetic energy, and a later phase during which the atoms keep separating at a fixed velocity. The drop in visibility is due to the thermally-induced blurring of the correlation ring at late times.

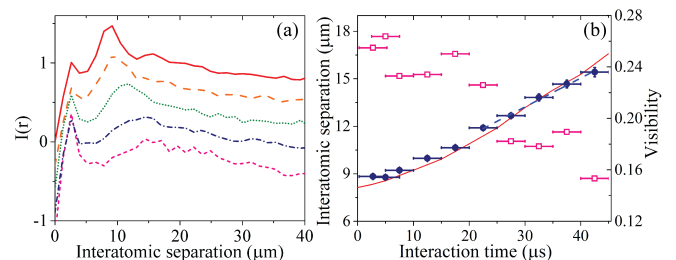


FIG. 3. (a) Angular integrals  $I(r)$  of the pair correlation images in Fig. 2 at wait times:  $2.5 \mu\text{s}$  (red solid),  $10 \mu\text{s}$  (orange dashed),  $20 \mu\text{s}$  (green dotted),  $30 \mu\text{s}$  (blue dot-dashed), and  $40 \mu\text{s}$  (pink short-dashed). The  $y$  axis is for the red-solid curve; for clarity, the other curves are shifted down in equidistant intervals of 0.3. (b) Interatomic separations between Rydberg-atom pairs as a function of interaction time (left axis, blue circles), obtained from the peak positions in the  $I(r)$  curves. The blue dashed line represents a linear fit at long wait times ( $20\text{--}40 \mu\text{s}$ ). The red solid line shows simulation results obtained for  $\delta\nu_L = 3$  MHz. The pink hollow squares show the visibility of the experimental pair correlation enhancement (right axis) as defined in text.

To extract the van der Waals  $C_6$  coefficient, one may consider an isolated atom pair excited at an initial separation  $r_0$ . The initial van der Waals energy is

$$W_0 = \frac{C_6}{r_0^6} = 2\delta\nu_L. \quad (1)$$

From Eq. 1,  $C_6 = 2\delta\nu_L r_0^6$  can, in principle, be obtained from spectroscopic measurement [14]. This method requires a well-defined  $r_0$ , a narrow laser linewidth, and accurate knowledge of  $\delta\nu_L$ . In our work, the relative uncertainty in  $r_0^6$  is about 12% (because the relative magnification uncertainty is 2%). In comparison, the uncertainty arising from  $\delta\nu_L = 4 \pm 2$  MHz is much larger. Taking all uncertainties into account, Eq. 1 leads to values of  $C_6$  ranging from  $7 \times 10^{-58} \text{ Jm}^6$  to  $40 \times 10^{-58} \text{ Jm}^6$ . There-

fore, Eq. 1 only allows us to perform a crude order-of-magnitude estimate for  $C_6$ . The main weakness of Eq. 1 is that the  $C_6$ -values derived from it directly reflect our large relative uncertainty in  $\delta\nu_L$ .

A better way for us to obtain  $C_6$  is to track the evolution of the Rydberg-atom trajectories. Over the experimentally investigated wait times, the entire initial van der Waals energy  $W_0$  becomes converted into kinetic energy. With the reduced mass of the atom pair,  $\mu$ , and the terminal relative velocity,  $v_t$ , it is

$$W_0 = \frac{C_6}{r_0^6} = \frac{1}{2}\mu v_t^2, \quad (2)$$

To obtain  $r_0$ , we take the weighted average of the fit results  $r_p(t)$  at the earliest times used in the experiment [the points in Fig. 3(b) at 250 ns and 2.5  $\mu$ s]. The averaging is valid because during the first few microseconds after excitation the Rydberg atoms are frozen in place due to their inertia. The statistical weights are given by the inverse squares of the fitting uncertainties of  $r_p$  at 250 ns and at 2.5  $\mu$ s. We obtain  $r_0 = 8.78 \mu\text{m}$  with a net fitting uncertainty of 0.02  $\mu\text{m}$ . To determine  $v_t$ , we perform a linear fit at long wait times (20-40  $\mu$ s) and obtain  $v_t = 0.182 \text{ m/s}$  with a fitting uncertainty of 0.008 m/s. It follows  $C_6 = \frac{1}{2}\mu v_t^2 r_0^6 = (5.4 \pm 0.5) \times 10^{-58} \text{ Jm}^6$ . Including the 2% magnification uncertainty, the total uncertainty of  $C_6$  becomes  $1.0 \times 10^{-58} \text{ Jm}^6$ .

The final relative uncertainty of  $C_6$  follows from three statistically independent contributions: the magnification uncertainty, the fit uncertainty for  $v_t$ , and the fit uncertainty for  $r_0$ . The respective powers at which these quantities enter into  $C_6$  are 8, 2, and 6. Factoring in these powers, the three quantities contribute respective independent uncertainties of 16%, 8.7%, and 1.4% to the relative uncertainty of  $C_6$ , leading to the total relative uncertainty of 18%. In our method, achieving a small magnification uncertainty is particularly important.

A semi-classical 3D simulation of the dynamics of Rydberg atoms interacting by an isotropic van der Waals force has been performed to interpret the experiment. The simulation volume of  $(140 \mu\text{m})^3$  exceeds the experimentally relevant volume by about a factor of two in each dimension. The 480 nm excitation beam propagates along the  $y$  direction. The excitation volume in the transverse directions ( $x$  and  $z$ ) is limited by the size of the excitation beam ( $w_0 = 8 \mu\text{m}$ ). The number of simulations is 5000, in keeping with the number of images analyzed in the experiment. Rydberg-atom positions and velocities are initialized as explained below, and the positions and velocities are then propagated using a Runge-Kutta integrator that includes all pair-wise interatomic forces. We use  $C_6 = 5.7 \times 10^{-58} \text{ Jm}^6$  [23] in the initialization and integration procedures. To avoid edge effects, we crop the  $xy$  processing area in the images to  $(70 \mu\text{m})^2$  before calculating the average pair-correlation images and the radial functions  $I(r)$ .

In each simulation, we start by drawing the number of Rydberg atoms to be used,  $n_{\text{Ryd}}$ , from a Poissonian

distribution. Initial trial positions of the Rydberg atoms are then drawn from a probability distribution that is Gaussian along  $x$  and  $z$ , with a  $w_0$  of 8  $\mu\text{m}$ , and uniform along  $y$  (in close analogy with the experiment). For an atom  $i$  at a trial position  $\mathbf{r}_i$ , the effective detuning  $\delta_{\text{eff}}(\mathbf{r}_i)$  due to all other atoms  $j$  at positions  $\mathbf{r}_j$  which are already excited into the Rydberg state is

$$\delta_{\text{eff}}(\mathbf{r}_i) = \sum_j \frac{C_6}{|\mathbf{r}_i - \mathbf{r}_j|^6} - \delta. \quad (3)$$

Since the detuning  $\delta\nu_L$  is substantial, the first pair of Rydberg atoms is simultaneously excited via off-resonant excitation [21] (because the intermediate state in which there is only one Rydberg atom present is off-resonant). Therefore the value of  $\delta$  in Eq. 3 for the first Rydberg-atom pair is set to be twice the laser detuning  $\delta\nu_L$ . For the excitation of additional atoms we use  $\delta = \delta\nu_L$  to simulate the stepwise addition of those atoms, which can be a near-resonant process with other atoms already present [8]. Detunings due to the Doppler effect are about 300 kHz and are neglected. The excitation probability  $P_{\text{ex}}(\delta_{\text{eff}})$  is a Gaussian centered at  $\delta_{\text{eff}} = 0$  with a FWHM of 4 MHz (given by the excitation bandwidth) and  $P_{\text{ex}}(\delta_{\text{eff}} = 0) = 1$ . A new Rydberg atom at position  $\mathbf{r}_i$  is created if the excitation probability is larger than a number randomly drawn between 0 and 1. This procedure is repeated with new trial positions until the desired number of  $n_{\text{Ryd}}$  Rydberg atoms has been reached. The initial center-of-mass velocities of the atoms are assigned using a Maxwell distribution at temperature 100  $\mu\text{K}$ .

In the simulation, we record the atom positions at the same wait times as used in the experiment. The resulting pair correlation images are shown for the case  $\delta\nu_L = 3 \text{ MHz}$  in the bottom row in Fig. 2. Black pixels along the left and right edges of each pair correlation are an artifact due to the normalization used in the image processing.

From the simulated pair correlation images we calculate the  $I(r)$  curves, as in the experiment, in order to obtain the most probable separations  $r_p(t)$  between Rydberg-atom pairs at each interaction time [see solid curve in Fig. 3(b), which is for  $\delta\nu_L = 3 \text{ MHz}$ ]. The simulated and experimental results for  $r_p(t)$  are in good agreement. In order to test how well our experimental procedure reproduces the  $C_6$  coefficient that underlies the atomic interactions, we evaluate the simulated results for  $r_p(t)$  using the same method that we also employ for the experimental data. The results for  $r_0$ ,  $v_t$  and  $C_6$  extracted from the simulated  $r_p(t)$  curves are shown in Table I for four choices of  $\delta\nu_L$ . These  $C_6$  values agree, within the uncertainties, with the value that has been entered as a fixed input into the simulation. This finding validates the experimentally used procedure; in particular it is seen that the method is not very sensitive on  $\delta\nu_L$ . The experimental and calculated [23]  $C_6$  values are also included in Table I for reference.

The experimental, simulated, and expected values for  $C_6$  in Table I are in reasonable agreement. Moreover, we observe that the entire simulated curve  $r_p(t)$  for  $\delta\nu_L =$



TABLE I. Comparison of calculated, experimental, and simulated results for  $C_6$ ,  $r_0$ , and  $v_t$ .

	$r_0$ ( $\mu\text{m}$ )	$v_t$ (m/s)	$C_6$ ( $\times 10^{-58} \text{Jm}^6$ )
Calculation			5.7
Experiment	$8.8 \pm 0.2$	$0.18 \pm 0.09$	$5.4 \pm 1.0$
Simulations			
$\delta\nu_L = 2 \text{ MHz}$	$8.85 \pm 0.06$	$0.17 \pm 0.02$	$4.9 \pm 1.0$
$\delta\nu_L = 3 \text{ MHz}$	$8.14 \pm 0.03$	$0.233 \pm 0.005$	$5.5 \pm 0.3$
$\delta\nu_L = 4 \text{ MHz}$	$7.76 \pm 0.05$	$0.278 \pm 0.003$	$6.0 \pm 0.3$
$\delta\nu_L = 5 \text{ MHz}$	$7.51 \pm 0.04$	$0.28 \pm 0.01$	$4.9 \pm 0.5$

3 MHz matches the experimental result very well [see Figs. 2 and 3(b)]. Overall, our findings lend credibility to our method of measuring  $C_6$ .

We note that higher-order quadrupole-dipole and quadrupole-quadrupole interaction potentials, which scale as  $r^{-7}$  and  $r^{-8}$ , are not important at the distances relevant in our work, at the current level of precision. We have verified this in a calculation of interaction potentials in which all terms up to the quadrupole-quadrupole interaction have been included [24].

A question of interest is whether the interatomic force is acting on “superatoms”, *i.e.* Rydberg excitations shared among a number of ground-state atoms, or on individual atoms. In our case, there are several tens of atoms within one blockade sphere. In our analysis, we have assumed that the effective mass of the interacting entities is half the rubidium atom mass, *i.e.* we have implied that the interacting entities are individual atoms and not superatoms. For our density and blockade radius, the total mass of a superatom equals that of several tens of atoms. The agreement between the  $C_6$  coefficients in Table I demonstrates that the interacting entities are indeed individual atoms. The finding implies that, during the course of the van der Waals interaction, excitations within superatoms become projected onto individual atoms, which are then ejected from the initial superatom volumes. The phenomenon has been predicted in [25] for superatom clouds interacting via a dipole-dipole interaction. In our work, we arrive at a similar conclusion for van-der-Waals-interacting Rydberg atoms in a 3D system.

Close inspection of the pair correlation functions from the simulation presented in Fig. 2 reveals anisotropic expansion behavior: the radius of enhanced pair correlation is larger in  $x$  than in  $y$  direction. In several experimental data sets we see some evidence of anisotropic expansion, such as in the experimental result shown in Fig. 4(a). The anisotropic expansion is due to the cylindrical shape of the excitation volume (not the interatomic interaction, which is isotropic). Since the blockade radius is close to the transverse size of the excitation region, at most two atoms can be excited side-by-side in  $x$  direction, leading to free, unimpeded expansion along that direction.

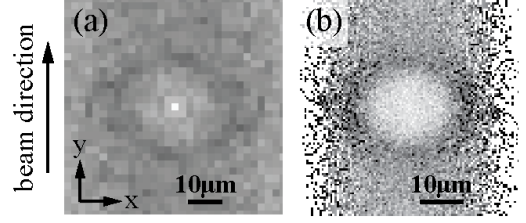


FIG. 4. Pair correlation function at wait time  $30 \mu\text{s}$  from (a) experiment and (b) simulation at  $\delta\nu_L = 3 \text{ MHz}$ . The anisotropic expansion of the atom ensemble causes the radius of enhanced pair correlation along the transverse direction ( $x$ ) to be larger than along the excitation beam direction ( $y$ ).

In contrast, more than two Rydberg atoms can be created along the  $y$  direction. Therefore, along  $y$  the expansion is slowed down due to multiple-atom repulsion. In our experiment, the overall Rydberg-atom density is high enough to sometimes observe this effect.

In summary, we have studied the trajectory of Rydberg-atom pairs interacting by repulsive, isotropic van der Waals interaction. We have extracted the  $C_6$  coefficient from the experiment and compared it with simulations and calculations, and have observed good agreement. The result implies that the interaction occurs between individual atoms, not superatoms. We have observed indications of an anisotropic effect in the expansion, caused by the excitation geometry. Future work may involve atom-atom interactions that are anisotropic, such as the dipole-dipole interaction.

This work was supported by the NSF (PHY-1205559) and the AFOSR (FA9550-10-1-0453). NT acknowledges support from DPST of Thailand.

\*nithi@umich.edu

†Present address: zeroK NanoTech Corporation, Gaithersburg, MD 20878, USA

- 
- [1] M. D. Lukin, M. Fleischhauer, R. Cote, L. M. Duan, D. Jaksch, J. I. Cirac, and P. Zoller, *Phys. Rev. Lett.* **87**, 037901 (2001).
  - [2] D. Tong, S. M. Farooqi, J. Stanojevic, S. Krishnan, Y. P. Zhang, R. Côté, E. E. Eyler, and P. L. Gould, *Phys. Rev. Lett.* **93**, 063001 (2004).
  - [3] T. C. Liebisch, A. Reinhard, P. R. Berman, and G. Raithel, *Phys. Rev. Lett.* **95**, 253002 (2005).
  - [4] M. Gärttner, S. Whitlock, D. W. Schönleber, and J. Evers, *Phys. Rev. Lett.* **113**, 233002 (2014).
  - [5] T. Pohl, E. Demler, and M. D. Lukin, *Phys. Rev. Lett.* **104**, 043002 (2010).
  - [6] P. Schauß, J. Zeiher, T. Fukuhara, S. Hild, M. Cheneau, T. Macrì, T. Pohl, I. Bloch, and C. Gross, *arXiv:1404.0980 [cond-mat, physics:physics]* (2014), *arXiv: 1404.0980*.
  - [7] I. Lesanovsky and J. P. Garrahan, *Phys. Rev. A* **90**, 011603 (2014).
  - [8] A. Urvoy, F. Ripka, I. Lesanovsky, D. Booth, J. Shaffer, T. Pfau, and R. Löw, *Phys. Rev. Lett.* **114**, 203002 (2015).
  - [9] L. Isenhower, E. Urban, X. L. Zhang, A. T. Gill, T. Henage, T. A. Johnson, T. G. Walker, and M. Saffman, *Phys. Rev. Lett.* **104**, 010503 (2010).
  - [10] T. Wilk, A. Gaëtan, C. Evellin, J. Wolters, Y. Miroshnychenko, P. Grangier, and A. Browaeys, *Phys. Rev. Lett.* **104**, 010502 (2010).
  - [11] T. Keating, K. Goyal, Y.-Y. Jau, G. W. Biedermann, A. J. Landahl, and I. H. Deutsch, *Phys. Rev. A* **87**, 052314 (2013).
  - [12] D. Petrosyan and K. Mølmer, *Phys. Rev. Lett.* **113**, 123003 (2014).
  - [13] A. Reinhard, K. C. Younge, T. C. Liebisch, B. Knuffman, P. R. Berman, and G. Raithel, *Phys. Rev. Lett.* **100**, 233201 (2008).
  - [14] L. Béguin, A. Vernier, R. Chicireanu, T. Lahaye, and A. Browaeys, *Phys. Rev. Lett.* **110**, 263201 (2013).
  - [15] V. Sandoghdar, C. I. Sukenik, E. A. Hinds, and S. Haroche, *Phys. Rev. Lett.* **68**, 3432 (1992).
  - [16] P. Nordlander and F. B. Dunning, *Phys. Rev. B* **53**, 8083 (1996).
  - [17] M. Fichet, G. Dutier, A. Yarovitsky, P. Todorov, I. Hamdi, I. Maurin, S. Saltiel, D. Sarkisyan, M.-P. Gorza, D. Bloch, and M. Ducloy, *Europhysics Letters (EPL)* **77**, 54001 (2007).
  - [18] A. Schwarzkopf, R. E. Sapiro, and G. Raithel, *Phys. Rev. Lett.* **107**, 103001 (2011).
  - [19] P. Schauß, M. Cheneau, M. Endres, T. Fukuhara, S. Hild, A. Omran, T. Pohl, C. Gross, S. Kuhr, and I. Bloch, *Nature* **491**, 87 (2012).
  - [20] P. McQuillen, X. Zhang, T. Strickler, F. B. Dunning, and T. C. Killian, *Phys. Rev. A* **87**, 013407 (2013).
  - [21] A. Schwarzkopf, D. A. Anderson, N. Thaicharoen, and G. Raithel, *Phys. Rev. A* **88**, 061406 (2013).
  - [22] F. Robicheaux, *J. Phys. B: At. Mol. Opt. Phys.* **38**, S333 (2005).
  - [23] A. Reinhard, T. C. Liebisch, B. Knuffman, and G. Raithel, *Phys. Rev. A* **75**, 032712 (2007).
  - [24] fixme.
  - [25] S. Möbius, M. Genkin, S. Wüster, A. Eisfeld, and J. M. Rost, *Phys. Rev. A* **88**, 012716 (2013).

# Measurement of van-der-Waals interaction by atom trajectory imaging

*N. Thaicharoen, A. Schwarzkopf, and G. Raithel*

Department of Physics, University of Michigan, Ann Arbor, MI 48109

## Supplement

We have used the model presented in detail in [1] to calculate the interaction potential between a pair of  $70S_{1/2}$  rubidium Rydberg atoms with dipole-dipole interaction terms only, as well as with dipole-dipole, dipole-quadrupole and quadrupole-quadrupole terms. The projection of the electron angular momenta onto the internuclear axis,  $M$ , can take the values 0 or  $\pm 1$ . For  $M=0$  there are two Rydberg-pair  $70S_{1/2}$  -  $70S_{1/2}$  levels, labeled A and B, while for  $M=\pm 1$  there is only one (see table). QQ means all interactions up to and including quadrupole-quadrupole terms are included. DD means only dipole-dipole terms are included.

It is seen that all the atom pair has very similar shifts on all potentials, and that interaction terms beyond the dipole-dipole term are not important in the atom distance range of interest ( $R > 7\mu\text{m}$ ). The results also agree well with a perturbative level-shift calculation in [2].

	M=0 Level A		M=0 Level B		M=1	
R	QQ	DD	QQ	DD	QQ	DD
$\mu\text{m}$	MHz	MHz	MHz	MHz	MHz	MHz
6	18.215	18.223	19.046	19.052	18.424	18.431
7	7.263	7.268	7.604	7.609	7.349	7.353
8	3.267	3.269	3.421	3.424	3.305	3.307
9	1.613	1.614	1.690	1.691	1.632	1.633
10	0.858	0.858	0.898	0.899	0.868	0.868

[1] J. Deiglmayr, H. Saßmannshausen, P. Pillet, and F. Merkt, Phys. Rev. Lett. **113**, 193001 (2014).

[2] A. Reinhard, T. C. Liebisch, B. Knuffman, and G. Raithel, Phys. Rev. **A 75**, 032712 (2007).



## Spatial correlations between Rydberg atoms in an optical dipole trap

A. Schwarzkopf, D. A. Anderson, N. Thaicharoen, and G. Raithel

*Department of Physics, University of Michigan, Ann Arbor, Michigan 48109, USA*

(Received 25 July 2013; revised manuscript received 1 November 2013; published 23 December 2013)

We use direct spatial ion imaging of cold  $^{85}\text{Rb}$  Rydberg atom clouds to measure the Rydberg-Rydberg correlation function, with and without light-shift potentials generated by an optical dipole trap. We find that the blockade radius depends on laser detunings and spatially varying light shifts. At certain laser detunings the probability of exciting Rydberg atoms at particular separations is enhanced, which we interpret to be a result of direct two-photon excitation of Rydberg atom pairs. The results are in accordance with predictions [F. Robicheaux and J. V. Hernández, *Phys. Rev. A* **72**, 063403 (2005)] and a model we develop that accounts for a one-dimensional dipole-trap potential.

DOI: [10.1103/PhysRevA.88.061406](https://doi.org/10.1103/PhysRevA.88.061406)

PACS number(s): 32.80.Ee, 32.80.Rm, 34.20.Cf, 42.50.Hz

Rydberg-Rydberg interactions are essential in recently proposed [1,2] and demonstrated [3,4] neutral-atom quantum information processing schemes. They also play important roles in many-body Rydberg-atom physics [5–9] and specifically in proposals to produce Rydberg crystals [10–13]. Much recent work uses or assumes the presence of an optical trap for ground or Rydberg atoms. Indeed, in many quantum information schemes a trap is important to assist single-qubit addressability [14–16]. Nonetheless, to our knowledge the influence of the trap on the Rydberg blockade, a signature of the Rydberg-Rydberg interactions [17,18], has not been explicitly studied. In this work, we demonstrate that laser detunings and background optical potentials each have significant effects on the Rydberg blockade. We focus on the blockade-induced correlations between Rydberg atom positions.

We start with a magneto-optic trap (MOT) of  $^{85}\text{Rb}$  atoms (density  $\gtrsim 10^{10} \text{ cm}^{-3}$ ) and, after switching off the MOT light, produce Rydberg atoms via a two-photon excitation from the  $5S_{1/2}$  ground state by using 780- and 480-nm laser pulses. (The MOT magnetic field is always on.) The excitation is detuned from the intermediate  $5P_{3/2}$  state by 1 GHz. We use crossed excitation beams, as shown in Fig. 1(a). The 780-nm beam has a Gaussian beam parameter of  $w_0 = 0.75 \text{ mm}$  while the 480-nm beam is focused to  $w_0 \lesssim 8 \mu\text{m}$ . Beam powers are 2 and 36 mW, respectively. Each is linearly polarized along  $\hat{z}$ , giving Rydberg atoms with  $m_j = \pm 1/2$ . In part of the work we excite the Rydberg atoms in an optical dipole trap (ODT) with 4 W of power and a focal spot of  $w_0 = 23 \mu\text{m}$ , crossed with the 480-nm beam focus. The ground-state atom density in the ODT is  $\gtrsim 10^{11} \text{ cm}^{-3}$ . We use Stark spectroscopy to reduce the electric field to  $\lesssim 20 \text{ mV/cm}$ . This is sufficient to avoid effects on the excitation blockade for the Rydberg states we excite [19].

We achieve spatially resolved detection of the Rydberg atoms by using a needle-shaped beryllium-copper field ionization electrode with a rounded tip of diameter  $125 \mu\text{m}$  [Fig. 1(b)], referred to as the tip imaging probe (TIP) [18]. The photoexcitation region is  $\approx 220 \mu\text{m}$  above the TIP. The ions resulting from field ionization are accelerated along the radially divergent electric field lines produced by the TIP. The ions are detected  $\approx 15 \text{ cm}$  away by a microchannel plate (MCP) spatially sensitive ion detector assembly. The magnification factor (the ratio between the ion separations in the MCP

plane and the Rydberg-atom separations in the excitation plane) is  $\approx 300$ , providing submicron resolution ( $\approx 0.5 \mu\text{m}$ ). This is comparable to existing [20,21] and proposed [22] diffraction-limited optical detection schemes and scanning electron microscope schemes [23].

To measure the Rydberg-Rydberg correlation function, we first acquire 10 000 CCD (charge-coupled device) images of the MCP phosphor screen, each image showing ion impact positions for a single experimental cycle of Rydberg excitation and ionization. We calculate the Rydberg pair correlation for each experimental cycle and then average these results. We use a peak detection algorithm to detect individual ion positions in each image; we then calculate the pair correlation from these discrete positions. Discrete peak detection is reliable because the minimum separation between Rydberg atoms (the blockade radius) is substantially larger than the imaging resolution.

We measure the Rydberg-Rydberg correlation function for excitation to states  $59S_{1/2}$ ,  $66S_{1/2}$ ,  $74S_{1/2}$ ,  $57D_{5/2}$ ,  $64D_{5/2}$ , and  $72D_{5/2}$ . Laser excitation pulse lengths are  $5 \mu\text{s}$  for  $S$  states and  $1 \mu\text{s}$  for  $D$  states, to account for differences in oscillator strength and to make count rates comparable. To eliminate

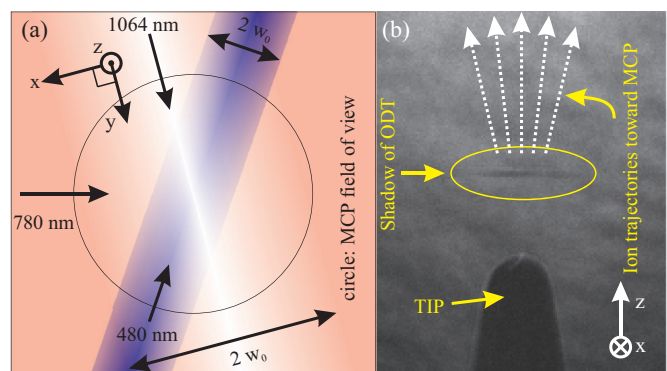


FIG. 1. (Color online) Experimental geometry: (a) A top view showing the crossed 780- and 480-nm excitation beams and the 1064-nm trap beam, with the  $2w_0$  widths marked for the 480- and 1064-nm beams. The circle shows an estimate of the field of view of the microchannel plate (MCP) in the excitation plane (radius  $25 \mu\text{m}$ ). (b) A shadow image of the ODT above the tip imaging probe (TIP), and a sketch of the ion trajectories toward the MCP.

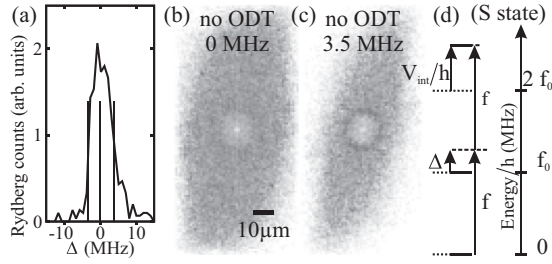


FIG. 2. (a) Excitation spectrum without ODT for  $66S_{1/2}$ . Note the line asymmetry, with interaction-induced broadening for  $\Delta > 0$ . The vertical lines show frequencies at which correlation functions are measured. Panels (b) and (c): Pair correlations for excitation of  $66S_{1/2}$  at the indicated detunings. (d) Level diagrams for off-resonant excitation without ODT. The laser frequency is  $f$ , and the frequency to excite one Rydberg atom without interactions is  $f_0$ . Dotted lines indicate energy levels without interactions. Solid lines are energy levels with interactions. The diagram is for the case of blue detuning from  $f_0$  ( $\Delta > 0$ ). The “two-photon resonance” for the direct excitation of two Rydberg atoms occurs when the interaction energy  $V_{\text{int}}/h = 2\Delta$ .

most images with fewer than two counts, we only use the 5 000 (of the 10 000 taken) that have the highest count numbers for calculating the average pair correlation.

For each state, we adjust the 480-nm laser frequency to excite at selected frequency points on the excitation spectra without and with the ODT, as indicated by vertical lines in Figs. 2(a) and 3(e), respectively. Resulting Rydberg pair correlations are shown in Figs. 2(b), 2(c), and 3(a)–3(d). Correlation values indicate the likelihood of finding Rydberg atoms with a given projection of their separation vector into the  $xy$  plane. The linear grayscale is set such that white is 0 and black is 2. With the normalization used, a value of 1 indicates no correlation, i.e., the equivalent of random Rydberg positions. Values  $<1$  indicate anticorrelation and those  $>1$  indicate positive correlation.

We first perform on-resonant excitation of state  $66S_{1/2}$  without ODT, with the result shown in Fig. 2(b). For Rydberg separations  $r < 8.5 \mu\text{m}$ , correlation values are suppressed due to the Rydberg excitation blockade. The single white pixel in the center reflects the inability to resolve two Rydberg atoms with a separation less than the imaging resolution. We next detune the 480-nm laser frequency to the blue of resonance, exciting at the point where the count rate has dropped by half [see Fig. 2(a)]. The resulting pair correlation is shown in Fig. 2(c). The dark ring in Fig. 2(c) reflects a clear enhancement of the probability of exciting two Rydberg atoms at a particular separation distance, as predicted in Refs. [7,9]. One expects this result for a detuning of the same sign as the van der Waals shift  $V_{\text{int}}$  (positive for rubidium  $S$  states, negative for  $D$  states [19,24]). The preferred separation is such that the laser resonantly excites two ground-state atoms directly to two Rydberg atoms, without populating an intermediate state that carries a single Rydberg excitation. An energy level diagram for this “two-photon” process is shown in Fig. 2(d). (Experimentally, this is a four-photon transition because each Rydberg transition involves both a 780- and 480-nm photon.) For  $S$  states we find that blue detunings yield these correlation

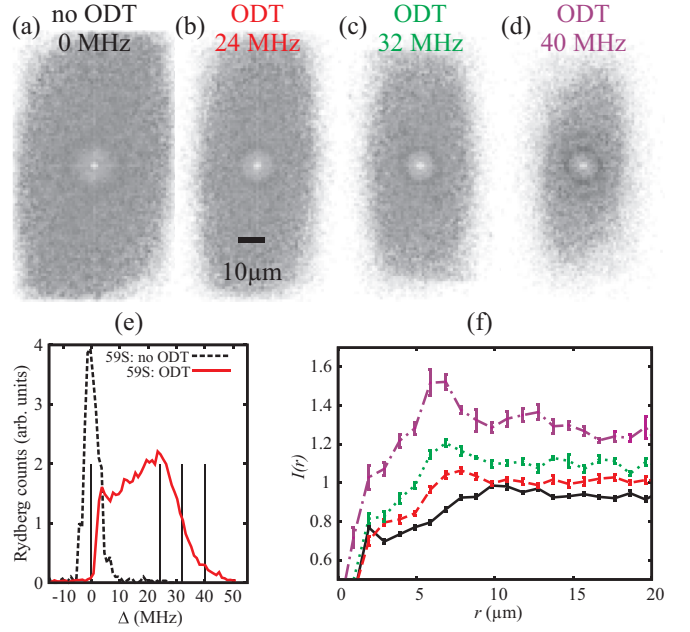


FIG. 3. (Color online) (a) Correlation function for resonant excitation of  $59S_{1/2}$  without ODT. Panels (b)–(d): Correlation functions for excitation in the ODT, at the indicated detunings. (e) Spectra for excitation of  $59S_{1/2}$  without ODT (black dashed curve) and with ODT (red [gray] solid curve). Vertical lines indicate the excitation frequencies used to acquire the correlation functions in panels (a)–(d). The 0-MHz line is for excitation without ODT; for the other lines the ODT is on. (f) Angular averages,  $I(r)$ , for the correlation functions in panels (a)–(d). The curves correspond to correlation functions as follows: black solid (a), red (gray) dashed (b), green (gray) dotted (c), and purple (dark gray) dot-dash (d). The vertical scale is labeled for the black solid curve; a vertical offset of 0.1 is applied between subsequent curves to allow visual discrimination. For  $r$  less than the imaging resolution, each curve  $I(r)$  drops to zero.

enhancements, while red detunings do not. For  $D_{5/2}$  states we observe the opposite behavior, since  $V_{\text{int}} < 0$ .

Our interpretation accords with the asymmetric broadening of the excitation lines, such as the  $S$  lines in Figs. 2(a) and 3(e) (dashed line). This indicates the presence of the two-photon process shown in Fig. 2(d), with a positive  $V_{\text{int}}/h$  of several megahertz.  $D_{5/2}$  lines (not shown) are broadened on the low-frequency side, corresponding to a negative  $V_{\text{int}}$ .

In subsequent experiments, we excite Rydberg atoms in the ODT at selected frequencies on the ODT spectrum, as depicted in Fig. 3(e). Pair correlations for  $59S_{1/2}$  are shown in Figs. 3(a)–3(d); Fig. 3(a) is for excitation without ODT, shown for comparison with ODT results in Figs. 3(b)–3(d). With increasing detuning, a ring of enhanced pair correlation both grows in visibility and shrinks in radius. At 40-MHz detuning a second ring emerges. We believe this is due to exciting a string of three equally spaced Rydberg excitations, with the middle excitation at the center of the ODT. The second ring is seen especially well in the angular averages  $I(r)$  shown in Fig. 3(f). The error bars in Fig. 3(f) are obtained by testing the variability of the results using subsets of the data. The uncertainty increases significantly for datasets at large laser detunings due to reduced count rates. A model for



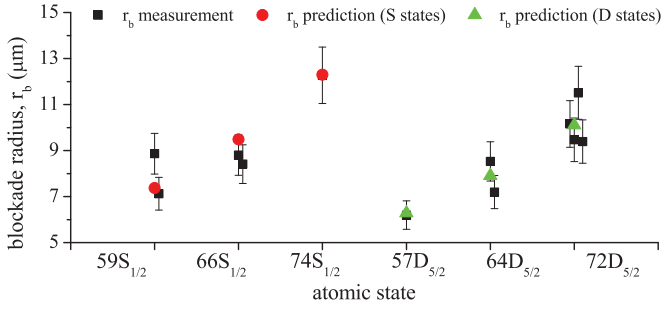


FIG. 4. (Color online) Measurements and predictions of the blockade radius  $r_b$  for several  $nS_{1/2}$  and  $nD_{5/2}$  states, for zero detuning without ODT. Error bars on measurements are  $\pm 10\%$  of the measured value, due to uncertainty in the magnification ratio calibration.

the excitation process, which explains the trends in Fig. 3, is presented below.

We measure the blockade radius  $r_b$  for each  $I(r)$  curve using the point closest to the origin where  $I(r)$  crosses its asymptotic value for large  $r$ . This method is suggested by results of a stochastic, nonquantum simulation of the excitation-blockade process, which accounts for our geometry including the  $z$  projection during detection. The hard-sphere blockade radii entered as inputs, and the resulting asymptote crossings of the simulated  $I(r)$  curves, agree to within  $\pm 1 \mu\text{m}$ .

In Fig. 4 we compare measurements and predictions of blockade radii for exciting on-resonance without ODT. One can estimate  $r_b$  by equating the Rydberg-Rydberg interaction strength with the laser excitation bandwidth [18,19,25,26]. Predictions in Fig. 4 are based on van der Waals interactions of the form  $V_{\text{int}} = C_6/|\mathbf{R}|^6$ , where  $\mathbf{R}$  is the Rydberg-Rydberg separation vector. The coefficient  $C_6$  is dependent on the interacting Rydberg states,  $|n, \ell, j, m_j\rangle$ , as well as (for  $D$  states) the angle  $\theta$  between  $\mathbf{R}$  and the quantization axis,  $\hat{z}$ . Our calculations use interaction strengths from Ref. [19], where for  $D$  states we use  $C_6$  for our experimental excitation conditions:  $\theta = \pi/2$  and, for  $\hat{z}$  light polarizations,  $m_j = \pm 1/2$ . Power-broadening dominates the excitation bandwidths, which are therefore taken to be each state's two-photon Rabi frequency (ranging from 500 kHz for  $74S$  to 1.5 MHz for  $57D$ ). Agreement between these predictions and our measurements is quite good.

We further measure the blockade radius when exciting from the ODT. Results for  $59S_{1/2}$  and  $57D_{5/2}$  are shown in Fig. 5 as a function of  $\Delta$ , the laser detuning from the trap-free transition. As the detuning  $\Delta$  increases, Rydberg atoms are excited deeper in the ODT. The data show an initial drop in  $r_b$  of several micrometers with the application of the ODT. With increasing  $\Delta$ ,  $r_b$  decreases for  $59S_{1/2}$  and increases for  $57D_{5/2}$ . The trends of  $59S_{1/2}$  and  $57D_{5/2}$  also differ near the maximum light shift in the trap ( $s_{\text{max}} \approx 30$  MHz for our ODT parameters; see Fig. 5). For  $59S_{1/2}$  we observe that Rydberg excitation is possible at detunings exceeding  $s_{\text{max}}$  by about 10 MHz [Figs. 3(e) and 5].

We model the system to predict the blockade radius, accounting for spatially dependent light shifts of the Rydberg transition. We consider the dimension with strongly varying light shifts [ $x$ ; see Fig. 1(a)]. Our model uses ODT parameters as described for the experiment and has no free parameters.

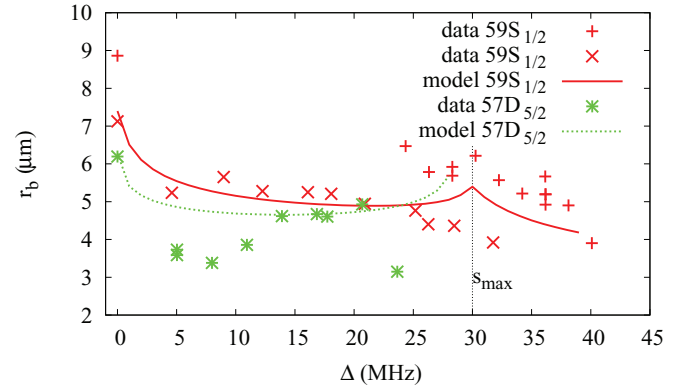


FIG. 5. (Color online) Blockade radius  $r_b$  as a function of  $\Delta$ , the laser detuning from the trap-free transition. Measurements are for exciting states  $59S_{1/2}$  [run 1 (+), run 2 ( $\times$ )] and  $57D_{5/2}$  (\*). Measurements at  $\Delta = 0$  are without ODT as in Fig. 4; other measurements are with ODT. Uncertainties are  $\pm 10\%$ . Predictions are lines, using the same excitation bandwidths as in Fig. 4. The light shift of the ground-Rydberg transition at the center of the ODT is  $s_{\text{max}} \approx 30$  MHz.

The light shifts of the two Rydberg atoms,  $s_1$  and  $s_2$ , are determined by the dynamic polarizabilities of both the  $5S_{1/2}$  ground state and the Rydberg state for 1064-nm laser light. For the ground state this is [27]  $\alpha_{5S} = 4\pi\epsilon_0 \times 711.4a_0^3$ ; for the Rydberg state it is calculated via the ponderomotive effect to be [28]  $\alpha_{\text{Ryd}} = -4\pi\epsilon_0 \times 545a_0^3$ . The resonant atomic excitation frequencies are then  $f_1 = f_0 + s_1$  and likewise  $f_2 = f_0 + s_2$  [with  $f_0$  defined in Fig. 2(d)]. The interaction energy between Rydberg atoms is modeled as

$$V_{\text{int}} = \frac{C_6}{(x_1 - x_2)^6}, \quad (1)$$

where  $x_1$  and  $x_2$  are the positions of the Rydberg atoms measured transverse to the ODT beam axis [see Fig. 6(a)]. For  $S$  states  $C_6 > 0$ , while for  $D$  states  $C_6 < 0$  [19,24].

We first consider  $S$ -state atoms for the case  $\Delta < s_{\text{max}}$ . We assume a stepwise excitation of two Rydberg atoms, with the first Rydberg atom resonantly excited ( $s_1 = \Delta$ ) at a position  $x_1$  in the ODT. To excite a second atom at location  $x_2$ , energy conservation requires

$$\Delta = s_2 + V_{\text{int}}/h \pm \delta, \quad (2)$$

as illustrated in Fig. 6(b), with an uncertainty  $\delta$  given by the excitation bandwidth. The position  $x_2$  of the second Rydberg atom is thus determined by balancing the positive interaction energy  $V_{\text{int}}$  with a smaller (positive) light shift,  $s_2 < s_1$ , to yield a second on-resonant transition. Among the solutions for  $|x_1 - x_2|$ , the smallest one will manifest itself as a blockade radius, so we take this one as the predicted  $r_b$ . The results of the model, shown as lines in Fig. 5, agree quite well with the  $59S_{1/2}$  data. The model accords with intuition: The smallest blockade radii are expected near the inflection point of the potential, where the light shift varies most rapidly with  $x$ .

As noted, for  $S$  states we measure that excitation is possible at much larger detunings, with  $\Delta > s_{\text{max}}$ . We model this domain by direct two-photon excitation of two Rydberg atoms; the off-resonant intermediate state carries one Rydberg

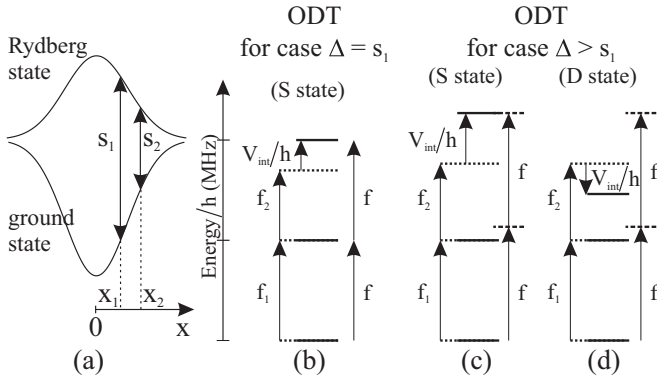


FIG. 6. (a) Spatially dependent light shifts of the ground and Rydberg states, with  $x$ ,  $s_1$ , and  $s_2$ , defined in text. Panels (b)–(d): Level diagrams for excitation of two Rydberg atoms from the ODT with the first step (b) on-resonant ( $f_1 = f$ ) for  $S$  states and [(c), (d)] off-resonant ( $f_1 < f$ ) for (c)  $S$  states and (d)  $D$  states.

excitation [see Fig. 6(c)]. The intermediate-state detuning,  $|s_1 - \Delta|$ , is minimized by placing the first Rydberg atom at the center of the ODT. Energy conservation for the direct two-photon excitation of the Rydberg atom pair then requires

$$s_1 + s_2 + V_{\text{int}}/h \pm \delta = 2\Delta. \quad (3)$$

With  $\Delta > s_{\text{max}}$  and  $V_{\text{int}} > 0$ , increasing  $\Delta$  gives solutions for Eq. (3) with increasing  $V_{\text{int}}$  (and thus diminishing  $r_b$ ). Blockade radii predicted in this region agree well with data in Fig. 5. The described two-photon excitation process is similar to that seen earlier for excitation without ODT [Fig. 2(d)]. The two-photon excitation leads to the production of Rydberg atom pairs at well-defined separations, giving rise to ring structures in the pair correlations. We can estimate the relative importance of stepwise and two-photon excitation based on the visibility of these structures. Two-photon excitation gradually increases in importance as  $\Delta$  approaches  $s_{\text{max}}$ , so the rings in Figs. 3(a)–3(d) smoothly shrink in radius and increase in visibility. The cusp in the solid curve in Fig. 5 is an artifact due to the model's piecewise nature, assuming that two-photon excitation occurs only when the more efficient stepwise excitation is impossible.

For  $D$  states ( $V_{\text{int}} < 0$ ), the two-photon process described by Eq. (3) cannot occur for  $\Delta > s_{\text{max}}$ , as illustrated in Fig. 6(d). Thus the excitation spectra of  $D$  lines in the ODT (not shown) do not extend beyond  $\Delta = s_{\text{max}}$ , which is why Fig. 5 does not show  $D$  data for  $\Delta > s_{\text{max}}$ . However, we believe that two-photon processes are responsible for the low  $r_b$  values measured in the range  $5 \text{ MHz} < \Delta < 12 \text{ MHz}$ . In this range, the laser is red-detuned from the Rydberg transitions of most atoms in the ODT (i.e.,  $\Delta < s$ ). Two-photon excitation is energetically allowed for pairs of such atoms, because a positive value of  $s_1 + s_2 - 2\Delta$  can be balanced with a negative  $V_{\text{int}}$ . This situation can be described by a diagram similar to Fig. 6(d) but with  $f < f_1, f_2$ . The two-photon process causes the  $r_b$  data to be smaller than predicted by the stepwise model. With increasing  $\Delta$  (range  $12 \text{ MHz} < \Delta < s_{\text{max}}$ ) the number of atoms that are available to this process (i.e., atoms with  $s > \Delta$ ) diminishes and the likelihood of direct two-photon excitation decreases. The data then approach the stepwise model (dashed line in Fig. 5). We note that excitation of a  $D$ -state atom at the center of the trap leads to a perfect blockade, as neither Eq. (2) nor Eq. (3) can be solved for  $x_1 = 0$  and  $V_{\text{int}} < 0$ .

Our one-dimensional model in  $x$  quantitatively explains our observations; we believe it captures the essential physics. In the experiment there is a perpendicular axis,  $y$ , along which there is no substantial light-shift gradient. Along this direction one might expect the trap-free blockade radius, but no clear anisotropy is observed in the experimental two-dimensional pair correlations.

In summary, we have measured the blockade radius for rubidium  $S_{1/2}$  and  $D_{5/2}$  Rydberg states and measured the effect of laser detunings and of light-shift potentials on the Rydberg pair correlation. We have observed a variation of the blockade radius as well as the appearance of additional structures in the pair-correlation functions, which we explain to be a result of direct two-photon excitation of Rydberg atom pairs at certain separations. Future studies may reveal the dynamics of these structures under the influence of decoherence and controlled shaping of the excitation pulses [10,29].

This work was supported by the NSF (PHY-1205559) and the AFOSR (FA9550-10-1-0453). N.T. acknowledges support from DPST of Thailand.

- [1] M. D. Lukin *et al.*, *Phys. Rev. Lett.* **87**, 037901 (2001).
- [2] D. Jaksch *et al.*, *Phys. Rev. Lett.* **85**, 2208 (2000).
- [3] L. Isenhower *et al.*, *Phys. Rev. Lett.* **104**, 010503 (2010).
- [4] T. Wilk *et al.*, *Phys. Rev. Lett.* **104**, 010502 (2010).
- [5] I. Mourachko *et al.*, *Phys. Rev. Lett.* **80**, 253 (1998).
- [6] W. R. Anderson, J. R. Veale, and T. F. Gallagher, *Phys. Rev. Lett.* **80**, 249 (1998).
- [7] F. Robicheaux and J. V. Hernández, *Phys. Rev. A* **72**, 063403 (2005).
- [8] J. V. Hernández and F. Robicheaux, *J. Phys. B* **39**, 4883 (2006).
- [9] C. Ates, T. Pohl, T. Pattard, and J. M. Rost, *Phys. Rev. A* **76**, 013413 (2007).
- [10] T. Pohl, E. Demler, and M. D. Lukin, *Phys. Rev. Lett.* **104**, 043002 (2010).
- [11] J. Schachenmayer, I. Lesanovsky, A. Micheli, and A. J. Daley, *New J. Phys.* **12**, 103044 (2010).
- [12] R. M. W. van Bijnen *et al.*, *J. Phys. B* **44**, 184008 (2011).
- [13] I. Lesanovsky, *Phys. Rev. Lett.* **106**, 025301 (2011).
- [14] E. Urban *et al.*, *Nat. Phys.* **5**, 110 (2009).
- [15] A. Gaetan *et al.*, *Nat. Phys.* **5**, 115 (2009).
- [16] C. Weitenberg *et al.*, *Nature (London)* **471**, 319 (2011).
- [17] D. Tong *et al.*, *Phys. Rev. Lett.* **93**, 063001 (2004).
- [18] A. Schwarzkopf, R. E. Sapiro, and G. Raithel, *Phys. Rev. Lett.* **107**, 103001 (2011).
- [19] A. Reinhard, T. C. Liebisch, B. Knuffman, and G. Raithel, *Phys. Rev. A* **75**, 032712 (2007).

- [20] W. S. Bakr *et al.*, [Nature \(London\)](#) **462**, 74 (2009).
- [21] J. F. Sherson *et al.*, [Nature \(London\)](#) **467**, 68 (2010).
- [22] G. Günter *et al.*, [Phys. Rev. Lett.](#) **108**, 013002 (2012).
- [23] T. Gericke *et al.*, [Nat. Phys.](#) **4**, 949 (2008).
- [24] K. Singer, J. Stanojevic, M. Weidemüller, and R. Côté, [J. Phys. B](#) **38**, S295 (2005).
- [25] J. V. Hernández and F. Robicheaux, [J. Phys. B](#) **41**, 045301 (2008).
- [26] M. Saffman, T. G. Walker, and K. Mølmer, [Rev. Mod. Phys.](#) **82**, 2313 (2010).
- [27] M. Marinescu, H. R. Sadeghpour, and A. Dalgarno, [Phys. Rev. A](#) **49**, 5103 (1994).
- [28] S. K. Dutta, J. R. Guest, D. Feldbaum, A. Walz-Flannigan, and G. Raithel, [Phys. Rev. Lett.](#) **85**, 5551 (2000).
- [29] S. Wüster, J. Stanojevic, C. Ates, T. Pohl, P. Deuar, J. F. Corney, and J. M. Rost, [Phys. Rev. A](#) **81**, 023406 (2010).





## Production and trapping of cold circular Rydberg atoms

D. A. Anderson,<sup>\*</sup> A. Schwarzkopf, R. E. Sapiro, and G. Raithel

*Department of Physics, University of Michigan, Ann Arbor, Michigan 48109, USA*

(Received 21 May 2013; published 16 September 2013)

Cold circular Rydberg atoms are produced and magnetically trapped. The trap is characterized by direct spatial imaging of ion distributions, ion counting, and state-selective field ionization. At room temperature, we observe about 70% of the trapped atoms remaining after 6 ms. We measure a trap oscillation frequency increase of the circular Rydberg atom trap relative to the ground-state atom trap due to the larger magnetic moment of the circular Rydberg atoms. Simulations of the center-of-mass and internal-state evolution of circular states in our magnetic trap are performed and results are in good agreement with experimental observations.

DOI: [10.1103/PhysRevA.88.031401](https://doi.org/10.1103/PhysRevA.88.031401)

PACS number(s): 32.10.Ee, 32.10.Dk, 37.10.Jk

Circular Rydberg states [1] correspond to highly excited, Bohr-like electron trajectories with maximal orbital angular momenta. Circular-state (CS) atoms exhibit a unique combination of extraordinary properties: long lifetimes, large magnetic moments, and no first-order Stark shift. These features have made CS atoms attractive for cavity quantum electrodynamics experiments [2,3], where the CS atoms provide a near-perfect two-level system for probing atom-cavity interactions. Precision measurements [4,5] benefit from the reduced nuclear and QED perturbations of these high-angular-momentum states. The large angular momenta also make CS atoms intriguing candidates for studies of interactions between Rydberg and ground-state atoms, such as the generation of Rydberg-ground molecules with GHz binding energies [6,7].

Several applications would benefit from trapping CS Rydberg atoms. While optical, electrostatic, and high-gradient magnetic trapping methods have been considered [8–10] and demonstrated [11–14] for atoms in other Rydberg states, cold, pure CS atoms have, to our knowledge, neither been prepared nor trapped. Additionally, magnetic Rydberg trapping has previously only been achieved for mixtures of Rydberg states, not for well-defined quantum states. In this Rapid Communication we describe the generation and trapping of cold, pure CS atoms in a conventional magnetic trap. We produce CS atoms at temperatures several orders of magnitude lower than in previous experiments (see, for example, [1,3,15,16]) and magnetically trap them. We employ the trapping force to measure their magnetic moments, which are the largest used in atom trapping to date. We characterize the trap using ion detection schemes that provide information on the center-of-mass (COM) oscillations in the trap, trap losses, and the atomic internal-state evolution.

We begin with a sample of  $\sim 10^7$   $^{87}\text{Rb}$  atoms magnetically trapped in the  $|F = 2, m_F = 2\rangle$  ground state at a temperature  $\sim 100$   $\mu\text{K}$  and density  $\sim 10^{10}$   $\text{cm}^{-3}$ . The Ioffe-Pritchard-type magnetic trap is generated using a Z-shaped wire [17]. The cigar-shaped trap has trap frequencies  $(\omega_{x'}, \omega_{y'}, \omega_{z'}) = 2\pi \times (7.9 \pm 0.3, 39.6 \pm 0.1, 37.4)$  Hz, where  $\omega_{x'}$  and  $\omega_{y'}$  are measured and  $\omega_{z'}$  is calculated. The trap field minimum is measured to be  $5.7 \pm 0.6$  G and is located  $3.5 \pm 0.2$  mm from the surface of the Z wire. A schematic of the experiment and a plot of the magnetic field strength are shown in Fig. 1. The

magnetic trapping region is enclosed by an electrode structure consisting of six individually addressable electrodes. Electric fields are controlled with an accuracy of  $\leq 30$  mV/cm in all coordinates using voltage-to-field calibration factors and field zeros obtained from Stark spectroscopy [18] on  $85D$  Rydberg states. Electrode “T” is used for Rydberg-atom field ionization and electrode “B” produces an electric-field ramp required for the CS production. A microchannel plate (MCP) is located 10 cm from the excitation region, outside of the electrode package, and is used for ion detection (30% efficiency) and imaging.

We generate CS atoms with principal quantum number  $n = 57$  by the crossed-fields method [19]. We first optically excite, in the presence of an electric field  $\mathbf{E} = -E\hat{z}$  from the B electrode (see Fig. 1), into the highest-lying state of the manifold of  $n = 57$  states that exhibit the linear Stark effect (“hydrogenic states”). The excitation is done with counterpropagating 480 and 780 nm laser beams. The fixed-frequency 780 nm laser is 1 GHz off-resonance from the  $5S_{1/2}$  to  $5P_{3/2}$  transition; the 480 nm laser is tunable to excite Rydberg levels. The combined excitation bandwidth is  $\nu_L \approx 2$  MHz. The 480 nm beam is focused to a waist of  $w_0 = 50$   $\mu\text{m}$  and the 780 nm beam is collimated to  $w_0 = 1.5$  mm, with powers of 35 and 2 mW, respectively. Both beams are linearly polarized perpendicular to the axis of the applied electric field. At a field of  $\approx 1.8$  V/cm the  $60P$  states intersect with the  $n = 57$  hydrogenic states. This field also mixes enough  $S$  and  $D$  character into the  $P$  Rydberg states to enable two-photon excitation from the  $5S_{1/2}$  ground state. Experimental and calculated two-photon excitation spectra are shown in Fig. 2. In the experimental spectrum the hydrogenic states appear only in regions where they intersect with  $60P$  states. Due to the coupling between the states, the intersections are anticrossings with splittings of 20 MHz or more, as seen in Fig. 2(b). For our initial step in the CS production we excite to regions labeled I and II in Fig. 2(a).

After a 15  $\mu\text{s}$  excitation pulse to region I, the electric field is ramped down over 40  $\mu\text{s}$  from its initial value of 1.76 V/cm to 0 V/cm, within the residual electric-field uncertainty. This is slow enough to ensure adiabatic evolution of the Rydberg atoms within the anticrossings in Fig. 2. Regions labeled IV are not chosen because of state crossings at lower electric-field values that would cause state mixing during the electric-field ramp. The 5.7 G magnetic field at the bottom of the atom trap is always on and is perpendicular to the

<sup>\*</sup>anderda@umich.edu

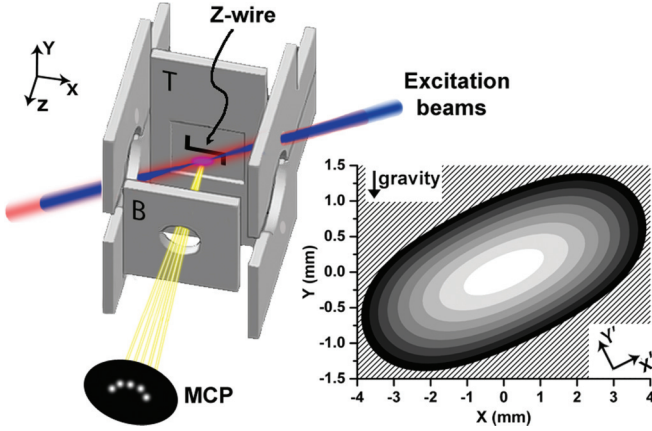


FIG. 1. (Color online) Left: schematic of the experiment (to scale). Six gold-coated, copper electrodes enclose a magnetically trapped atom sample to control the electric fields at the excitation location. An MCP is used for ion detection. The location of the Z wire and the counterpropagating 480 and 780 nm beams for excitation to Rydberg states are also shown. Right: plot of the magnetic field strength in the  $xy$  plane through the center of the trap. The linear gray scale ranges from  $|B| = 5.5$  G (white) to 9.5 G (black) in steps of 0.5 G. The hatched region indicates  $|B| \geq 10$  G.

ramped electric field. At the end of the ramp, the Larmor frequency ( $\omega_L = 2\pi \times 8$  MHz) is larger than the residual Stark frequency ( $\omega_S = \frac{3nEea_0}{2\hbar} \lesssim 2\pi \times 3$  MHz, where  $e$  and  $a_0$  are the electron charge and Bohr radius, respectively). In the adiabatic sweep from the Stark-dominated ( $\omega_S > \omega_L$ ) to the Zeeman-dominated regime ( $\omega_S < \omega_L$ ) the atoms initially prepared into region I in Fig. 2(a) evolve with near-unity probability into the  $|n = 57, \ell = 56, m_\ell = 56, m_s = +0.5\rangle$  CS. The CS has good quantum numbers  $m_\ell$  and  $m_s$  because in high- $\ell$  states the Zeeman effect dominates the fine structure. The magnetic field stabilizes the CS by lifting its degeneracy with any other hydrogenic state. The angular momentum of the trapped CS atom is parallel to the magnetic field at the trap minimum, which points along  $\mathbf{x}'$  in Fig. 1. This CS is low-field seeking; the complementary  $|n = 57, \ell = 56, m_\ell = -56, m_s = -0.5\rangle$  CS is unsuitable for magnetic atom trapping because it is high-field seeking.

Due to their large magnetic moments, CS atoms in a magnetic trap experience significantly deeper confining potentials than ground-state atoms. The magnetically trapped  $|F = 2, m_F = 2\rangle$  atoms (Landé factor  $g_F = \frac{1}{2}$ ) have a magnetic moment of one Bohr magneton,  $\mu_{GS} = -\mu_B$ . The CS atoms described above have a magnetic moment  $\mu_{CS} = -\mu_B(m_\ell + g_s m_s) = -57\mu_B$ , where  $g_s \approx 2$ . In a harmonic magnetic trap, the CS atom experiences a potential increase,  $U_{CS} = (\frac{\mu_{CS}}{\mu_{GS}})U_{GS} = 57U_{GS}$ , and a corresponding trap frequency increase,  $\omega_{CS} = \sqrt{57}\omega_{GS}$ , where  $U_{CS}$  and  $U_{GS}$  are the CS and ground-state magnetic potentials, and  $\omega_{CS}$  and  $\omega_{GS}$  are the CS and ground-state trap frequencies, respectively.

The minimum of the ground-state trap is substantially shifted due to gravity, while in the much stronger CS trap gravity can be ignored. The displacement vector pointing from the minimum of the ground-state trap to the minimum of the CS trap is calculated to be  $\delta\mathbf{r} = (\delta x, \delta y, \delta z) = (710, 290, 0) \mu\text{m}$  (using calculated force constants and the  $12 \pm 0.2$  degree tilt of

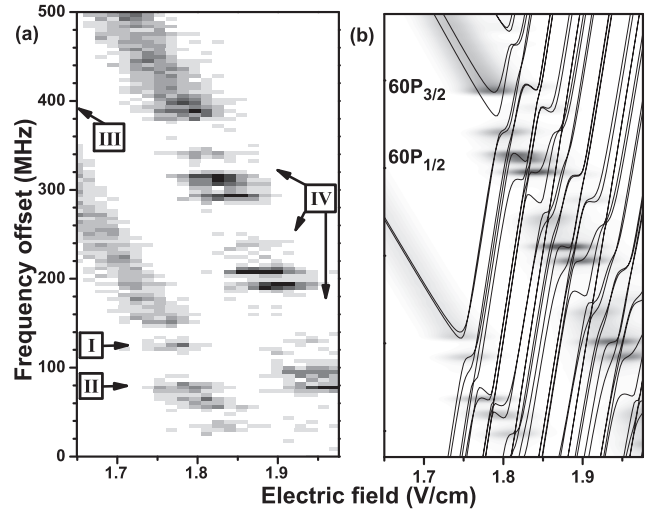


FIG. 2. (a) Experimental Stark spectrum showing the intersection of  $60P$  with the  $n = 57$  hydrogenic manifold. Plotted are average counts per excitation pulse [linear scale ranging from 0 (white) to  $>3.5$  (black)] as a function of applied electric field and frequency offset of the 480 nm laser from an arbitrary reference frequency. Each data point is an average of 50 excitation pulses. The electric-field axis is scaled by a factor of 0.98 to match the calculation in (b). (b) Energy levels (solid lines) and excitation rates per atom calculated for our laser polarizations and intensities (overlay; linear gray scale from 0 to  $150 \text{ s}^{-1}$ ). In the excitation-rate calculation we assume Gaussian distributions for the excitation frequency and electric field, with FWHM of 5 MHz and 50 mV/cm, respectively. Minor deviations in frequency between (a) and (b) are attributed to long-term excitation-laser drifts.

the trap with respect to gravity; see Fig. 1). This displacement allows us to initiate sloshing-mode oscillations of trapped CS atoms in the  $\mathbf{x}'$  and  $\mathbf{y}'$  directions.

To observe these oscillations we first generate the  $|CS - 1\rangle \equiv |n = 57, \ell = 56, m_\ell = 55, m_s = +0.5\rangle$  near CS by initial excitation to region II in Fig. 2. We excite to II because it provides a stronger experimental signal than I; both regions result in high- $\ell$  states that exhibit quantitatively similar trapping behavior. The expected trap period for the near CS is  $T_{CS-1} = \frac{T_{GS}}{\sqrt{n-1}}$ , which equals 16.9 and 3.4 ms in  $\mathbf{x}'$  and  $\mathbf{y}'$ , respectively. Since the excitation and circularization time interval of  $55 \mu\text{s}$  is much smaller than  $T_{CS-1}$ , the atoms are prepared on the side of their trapping potential  $U_{CS-1}$ , at the location  $-\delta\mathbf{r}$ . A field-ionization pulse is applied at varying time delays  $t_d$  from the end of the  $|CS - 1\rangle$  production. The ion positions are projected onto the MCP, where they generate spatially resolved light pulses on a phosphor screen, which is imaged by a CCD camera. The COM coordinates of the ion distributions in the MCP plane are obtained from sums of 2000 images at each  $t_d$  [20]. Plots of the  $x$  and  $y$  COM coordinates as a function of  $t_d$  are shown in Fig. 3. The  $y$  COM data [Fig. 3(a)] is fit to a sinusoid out to 4 ms from which we obtain an oscillation period of  $3.4 \pm 0.1$  ms. This is in excellent agreement with the predicted value. The  $y$  COM data is only considered out to 4 ms because of distortions in the ion trajectories thereafter, as suggested by the  $x$  COM data. Since  $\delta x \approx 2.5\delta y$ , we expect a larger COM oscillation

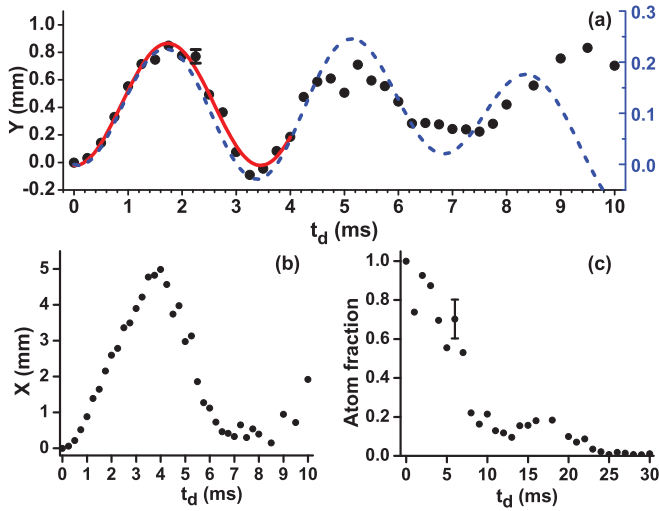


FIG. 3. (Color online) (a) Experimental COM displacement in  $y$  vs  $t_d$  (circles) in the MCP plane (left axis) with a fit to a sinusoid out to 4 ms (solid curve). The RMS spread of the data about the fit is 0.05 mm, indicated by the representative error bar. The simulated COM displacement in  $y$  vs  $t_d$  in the object plane (right axis) is shown out to 10 ms (dashed curve). A linear offset is subtracted to match the experimental data, accounting for ion-imaging aberrations. (b) Experimental COM displacement in  $x$  vs  $t_d$ . (c) Fraction of detected atoms remaining vs  $t_d$ . Based on the variance of the data points, we estimate an uncertainty shown by the representative error bar.

amplitude in  $x$ . The  $x$  COM coordinate plotted in Fig. 3(b) develops a large displacement over about 4 ms. At  $t_d = 4$  ms there is an apparent reversal in the direction of motion of the  $x$  COM coordinate, which occurs about a factor of 2 earlier than expected. We believe that the  $x$  COM oscillation amplitude is so large that it brings the ions produced by field ionization far enough off of the ion-imaging axis to cause distortion and obstruction [see Fig. 3(c) and discussion]. This prevents a direct measurement of the  $x$  COM oscillation period, as well as the  $y$  COM oscillation period after 4 ms.

To model the system, we perform Monte Carlo simulations of the internal-state evolution of a sample initially in the state  $|CS - 1\rangle$  in a  $T = 300$  K radiation background; atom trajectories inside the magnetic trapping field are computed classically. The internal-state evolution and trajectories are coupled. The simulations account for all radiative transitions, including thermal photoionization, but no collisions. Typically, the rate of thermally induced transitions per atom is  $6 \times 10^3 \text{ s}^{-1}$ . (For comparison, in a  $T = 4$  K cryogenic enclosure it would be  $0.1 \times 10^3 \text{ s}^{-1}$ .) The rapid state evolution from the  $|CS - 1\rangle$  due to the 300 K thermal radiation results in  $n$ ,  $\ell$ , and  $m$  redistribution of the initially prepared sample, leading to a time dependence of the average magnetic dipole force as well as a diffusive component of that force. The change in average  $m$  amounts to less than 1% over the 10 ms observation time. The corresponding change in average oscillation frequency is too small to be seen in the experiment. The diffusive component of the  $m$  evolution is more significant, reaching an rms spread of  $\pm 15\%$  about the average  $m$  over 10 ms. This is large enough that we would expect some damping effect on the COM oscillations. From the simulations we

obtain COM oscillation periods and decay constants of 16.5 and 36.2 ms in  $x'$  and 3.4 and 10.2 ms in  $y'$ , respectively. In Fig. 3(a) we plot the simulated  $y$  COM oscillation with a linear offset subtracted to match the experiment, accounting for ion-imaging aberrations. We test the importance of thermally driven  $m$ -state diffusion by turning off all radiative transitions in the simulation, leaving anharmonicity-induced dephasing as the sole source of damping. We find that  $m$  diffusion and trap anharmonicity contribute in approximately equal parts to the decay of the COM oscillations over 10 ms.

To measure the magnetic trapping time we plot the number of detected Rydberg atoms as a function of  $t_d$ . Figure 3(c) shows the fraction of Rydberg atoms detected relative to  $t_d = 0$ . We observe as much as 70% of the initially prepared sample remaining in the trap after 6 ms. If any  $60P$  atoms remained after the circularization sequence, our simulations show that only a  $\sim 5 \times 10^{-5}$  fraction of them would survive after 6 ms. From this we conclude that our circularization procedure is very efficient. Between 7 and 13 ms we measure a rapid drop in signal, as well as a significant resurgence at about 16 ms. We believe that the rapid drop is due to atoms moving out of the ion-imaging field of view (in the  $x$  direction), while the resurgence occurs because of atoms moving back into view. This scenario is consistent with both the expected  $x$  oscillation period (16.5 ms) as well as the early reversal of the  $x$  COM in Fig. 3(b).

From Fig. 3(c) we estimate an overall loss rate of  $\gtrsim 50 \text{ s}^{-1}$  for the trapped CS population. This loss rate cannot be explained at a quantitative level, as low-velocity CS atoms were not available until now and data on their collision cross sections are not available. However, the loss rate is consistent with collisions between Rydberg and ground-state atoms being the primary loss mechanism. This is determined from collisional cross sections between Rb low- $\ell$  Rydberg and ground-state atoms provided in [21] and the estimated background Rb pressure. Losses from Rydberg-Rydberg collisions are not expected at the low Rydberg atom densities used (initially a few  $10^6 \text{ cm}^{-3}$ ). Our simulations of the state evolution show a loss rate of about  $0.5 \text{ s}^{-1}$  (at 300 K and accounting for all noncollisional loss channels), which is negligible in comparison to the measured loss rate.

Given the influence of the internal-state dynamics on the trapping behavior, we probe the internal-state evolution by performing state-selective field ionization (SSFI) on the trapped Rydberg atom sample. A near-linear SSFI ramp is applied reaching a field of  $>120 \text{ V/cm}$  over the course of  $50 \mu\text{s}$ . Different Rydberg states ionize at different points on the ramp, and can be distinguished by arrival time at the detector. Figure 4(a) shows SSFI traces for excitation to region III in Fig. 2, where only  $60P_{1/2}$  atoms are excited. In this case, the electric-field ramp in the circularization procedure fails to populate any atoms in the CS; all atoms remain in  $60P_{1/2}$ . Figure 4(b) shows SSFI traces for excitation to region I in Fig. 2, where the CS generation procedure is expected to circularize most of the atoms. In both cases we obtain SSFI traces for  $t_d = 0$  and 1 ms. We first compare the integrals of the SSFI curves. Excitation to region I produces a long-lived signal (0.59 remaining fraction), while excitation to III does not (0.09 remaining fraction), reaffirming the high yield of long-lived CS atoms.



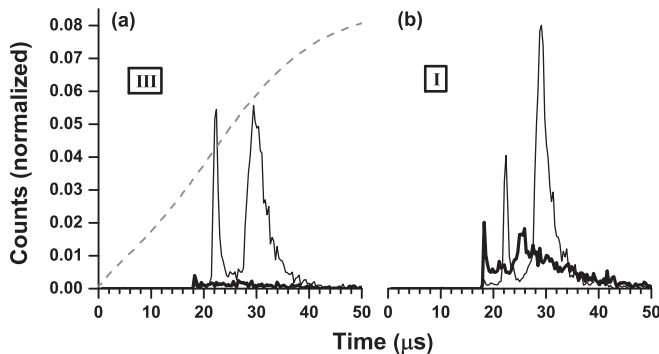


FIG. 4. SSFI traces for an initial excitation into two different regions in Fig. 2: (a) into III, the  $60P_{1/2}$  state and (b) into I, the first anticrossing at the  $60P$ -manifold intersection to generate the CS after the circularization procedure. In both (a) and (b) the thin and thick traces correspond to  $t_d = 0$  and 1 ms, respectively. Each trace is a sum of 20 000 experiments. The data are normalized such that for  $t_d = 0$  ms the curves integrate to the same value. The dashed curve in (a) shows the field-ionization ramp used in both experiments.

Next we compare the structures of the SSFI curves. In both Figs. 4(a) and 4(b), with  $t_d = 0$ , there are two distinct peaks: an early (22  $\mu$ s) peak, which we attribute to adiabatic field-ionization events, and a later (29  $\mu$ s) diabatic, high-field-ionizing peak [22]. In Fig. 4(b), the diabatic peak for  $t_d = 1$  ms arrives earlier than for  $t_d = 0$  ms, and is substantially broadened. This indicates a reduced average ionization field for the trapped sample at later times (corresponding to a higher average  $n$ ) and rapid state diffusion, respectively. An additional peak emerges at an even earlier arrival time (18  $\mu$ s). This peak is attributed to atoms accumulating in extremely

high- $n$  Rydberg states. The trends in Fig. 4 are in qualitative agreement with our simulations, which also show a thermally driven redistribution of population to longer-lived, very high- $n$  states. For experimental reasons the field ionization is performed in crossed electric and magnetic fields; a detailed modeling of the SSFI curves in Fig. 4 is beyond the scope of this paper.

In summary, we have demonstrated a room-temperature magnetic trap for cold CS Rydberg atoms with  $n = 57$ . The trap oscillation period and trapping time have been measured and are in good agreement with predicted values and detailed simulations. The internal-state evolution of the atom sample was probed, showing the effect of the 300 K blackbody radiation background on the  $n$  distribution in the trap. Our trapping method could be employed in a 4 K cryogenic environment to suppress thermal transitions and provide a source of long-lived CS atoms for precision measurements [4,5]. Our work on cold, trapped CS Rydberg atoms paves the way for studies of exotic quantum states. For example, at sufficiently high ground-state atom density high- $\ell$  Rydberg-ground molecules [6] may be produced in the generation of the CS. Due to their increased mass, these molecules would manifest as trailing signals in the COM oscillations of the CS in the magnetic trap. Another intriguing quantum object, which one could prepare in a setup similar to ours, would consist of a hollow electron wave function (that of the CS Rydberg atom) surrounding the ionic Rydberg-atom core and a Bose-Einstein condensate. This system would present an ideal platform to study interactions between ions and condensates [23–25].

This work was supported by the AFOSR (Grant No. FA9550-10-1-0453).

- [1] R. G. Hulet and D. Kleppner, *Phys. Rev. Lett.* **51**, 1430 (1983).
- [2] R. G. Hulet, E. S. Hilfer, and D. Kleppner, *Phys. Rev. Lett.* **55**, 2137 (1985).
- [3] M. Brune, E. Hagley, J. Dreyer, X. Maitre, A. Maali, C. Wunderlich, J. M. Raimond, and S. Haroche, *Phys. Rev. Lett.* **77**, 4887 (1996).
- [4] J. Hare, A. Nussenzweig, C. Gabbanini, M. Weidemuller, P. Goy, M. Gross, and S. Haroche, *IEEE Trans. Instrum. Meas.* **42**, 331 (1993).
- [5] R. Lutwak, J. Holley, P. P. Chang, S. Paine, D. Kleppner, and T. Ducas, *Phys. Rev. A* **56**, 1443 (1997).
- [6] C. H. Greene, A. S. Dickinson, and H. R. Sadeghpour, *Phys. Rev. Lett.* **85**, 2458 (2000).
- [7] V. Bendkowsky, B. Butscher, J. Nipper, J. P. Shaffer, R. Löw, and T. Pfau, *Nature (London)* **458**, 1005 (2009).
- [8] S. K. Dutta, J. R. Guest, D. Feldbaum, A. Walz-Flannigan, and G. Raithel, *Phys. Rev. Lett.* **85**, 5551 (2000).
- [9] W. H. Wing, *Phys. Rev. Lett.* **45**, 631 (1980).
- [10] B. Hezel, I. Lesanovsky, and P. Schmelcher, *Phys. Rev. Lett.* **97**, 223001 (2006).
- [11] S. E. Anderson, K. C. Younge, and G. Raithel, *Phys. Rev. Lett.* **107**, 263001 (2011).
- [12] S. Zhang, F. Robicheaux, and M. Saffman, *Phys. Rev. A* **84**, 043408 (2011).
- [13] S. D. Hogan and F. Merkt, *Phys. Rev. Lett.* **100**, 043001 (2008).
- [14] J.-H. Choi, J. R. Guest, A. P. Povilus, E. Hansis, and G. Raithel, *Phys. Rev. Lett.* **95**, 243001 (2005).
- [15] J. Hare, M. Gross, and P. Goy, *Phys. Rev. Lett.* **61**, 1938 (1988).
- [16] R. Brecha, G. Raithel, C. Wagner, and H. Walther, *Opt. Commun.* **102**, 257 (1993).
- [17] J. Reichel, W. Hänsel, and T. W. Hänsch, *Phys. Rev. Lett.* **83**, 3398 (1999).
- [18] J. Neukammer, H. Rinneberg, K. Vietzke, A. König, H. Hieronymus, M. Kohl, H. J. Grabka, and G. Wunner, *Phys. Rev. Lett.* **59**, 2947 (1987).
- [19] D. Delande and J. C. Gay, *Europhys. Lett.* **5**, 303 (1988).
- [20] See Supplemental Material at <http://link.aps.org/supplemental/10.1103/PhysRevA.88.031401> for a video sequence of composite images with increasing  $t_d$ .
- [21] T. F. Gallagher, *Rydberg Atoms* (Cambridge University Press, New York, 1994), pp. 220–221.
- [22] R. Stebbings and F. Dunning, *Rydberg States of Atoms and Molecules* (Cambridge University Press, New York, 1983), pp. 100–101.
- [23] R. Côté, V. Kharchenko, and M. D. Lukin, *Phys. Rev. Lett.* **89**, 093001 (2002).
- [24] R. Côté, *Phys. Rev. Lett.* **85**, 5316 (2000).
- [25] R. Côté and A. Dalgarno, *Phys. Rev. A* **62**, 012709 (2000).

# Imaging Spatial Correlations of Rydberg Excitations in Cold Atom Clouds

A. Schwarzkopf, R. E. Sapiro, and G. Raithel

*FOCUS Center, Department of Physics, University of Michigan, Ann Arbor, Michigan 48109, USA*

(Received 3 May 2011; published 31 August 2011)

We use direct spatial imaging of cold  $^{85}\text{Rb}$  Rydberg atom clouds to measure the Rydberg-Rydberg correlation function. The results are in qualitative agreement with theoretical predictions [F. Robicheaux and J. V. Hernández, *Phys. Rev. A* **72**, 063403 (2005)]. We determine the blockade radius for states  $44D_{5/2}$ ,  $60D_{5/2}$ , and  $70D_{5/2}$  and investigate the dependence of the correlation behavior on excitation conditions and detection delay. Experimental data hint at the existence of long-range order.

DOI: 10.1103/PhysRevLett.107.103001

PACS numbers: 32.80.Ee, 32.80.Rm, 34.20.Cf

When cold atoms are laser-excited to Rydberg states, the strong interactions between Rydberg excitations can lead to complex many-body entanglement in the system. The excitation process results in spatial correlations between excitations. In most cases, Rydberg excitation positions are anticorrelated such that no two excitations are within a “blockade radius”  $r_b$  of each other. Such systems are well-suited for studying basic many-body physics [1–3], as well as for future technological applications such as quantum computation [4,5]. Theory for the laser excitation process that leads to the Rydberg blockade is considered in Refs. [6,7]. Previous experiments have shown the blockade effect to cause a suppression of excitation in an atom sample [8] and sub-Poissonian excitation-number statistics [9]. The underlying energy level shifts were measured spectroscopically [10].

We are presently interested in the spatial aspect of the blockade. In spatially resolved studies, the distance [11] and angle dependence [12] of Rydberg-Rydberg interactions were examined. The blockade effect was shown to be effective between spatially separated atom pairs in adjacent dipole traps [13,14]. In this Letter, we directly image a system containing multiple Rydberg excitations to obtain the Rydberg-Rydberg correlation function. We find evidence of the Rydberg excitation blockade and measure the blockade radius for several principal quantum numbers  $n$ .

The experimental setup is sketched in Fig. 1. The key feature enabling spatial resolution of the Rydberg sample is the ionization electrode: a beryllium-copper needle with a rounded tip of diameter  $125\text{ }\mu\text{m}$ . This tip imaging probe (TIP) is surrounded by a closed cage of electrodes whose voltages can be controlled to a precision of several millivolts. These electrodes allow independent control of the electric field in three orthogonal directions. To provide temporal and spatial electric-field stability, the apertures in the electrodes are covered with wire mesh, which has  $0.51\text{ mm}$  grid spacing and 88% transparency.

The experiment runs at a repetition rate of 30 Hz. We collect  $^{85}\text{Rb}$  atoms for about 30 ms in a magneto-optic trap (MOT) located  $\sim 500\text{ }\mu\text{m}$  above the TIP. After turning off

the MOT light, we optically pump the ground state atoms into the  $5S_{1/2}|F=3, m_F=3\rangle$  state, with the quantization axis along the beam direction. We then excite Rydberg atoms in a two-step process, using counterpropagating 480 and 780 nm beams. The excitation region is  $\sim 360\text{ }\mu\text{m}$  above the TIP. The beams are  $\sigma^+$  polarized and resonantly drive the transitions  $5S_{1/2}|F=3, m_F=3\rangle \rightarrow 5P_{3/2}|F'=4, m'_F=4\rangle \rightarrow nD_{5/2}|F''=5, m''_F=5\rangle$ . The red beam has a Gaussian beam parameter of  $w=0.75\text{ mm}$ , while the blue beam is focused to  $w_0 \leq 8\text{ }\mu\text{m}$  with a theoretical confocal parameter of  $0.3\text{ mm}$ . Because of the much larger size of the red beam, the intermediate-state population is uniform across the width of the excitation region. We establish with CCD imaging that the intensity distribution of the blue focus is only weakly altered by diffraction from the mesh. Laser linewidths are on the order of 1 MHz. Typical Rydberg atom densities are  $\sim 10^9\text{ cm}^{-3}$ , dependent on atomic state and laser power.

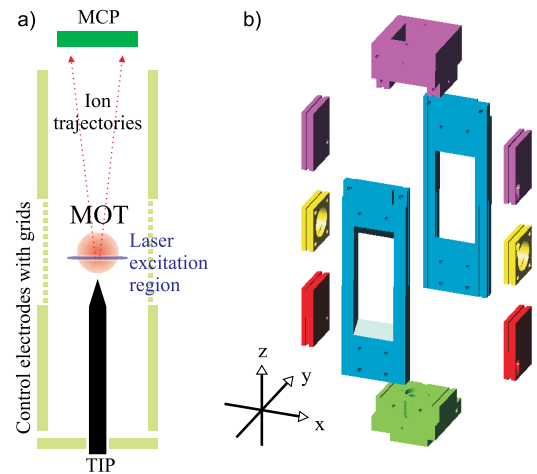


FIG. 1 (color online). (a) Overview of excitation region and ion detection. (b) Exploded view of electrodes that surround the excitation region, used for electric-field control. The purple, blue, and yellow electrodes allow electric-field control in the  $z$ ,  $y$ , and  $x$  directions, respectively. Green and red electrodes are grounded.

After excitation, the TIP is switched to high voltage to produce a strong, radially divergent electric field. This field ionizes the Rydberg atoms, and the ions are extracted along the divergent field lines. The ions are detected approximately 15 cm away by a microchannel plate detector (MCP), which has a spatial resolution of  $\geq 10$  lines/mm. The method resembles field ion microscopy and leads to magnified ion images of the initial Rydberg atom locations. This image is captured by a CCD video camera, synchronized with the experiment.

In most cases we use 100 ns excitation pulses with a subsequent negligible delay before the field ionization pulse. Under these conditions the atoms can be considered “frozen” in space during the experiment. These parameters are later varied to study their effect on the Rydberg-Rydberg correlation function.

To observe an excitation blockade, it is essential to avoid electric fields during the excitation pulse. Electric fields would cause undesired modifications of the Rydberg-Rydberg interaction potentials. Furthermore, electric-field inhomogeneity would induce inhomogeneous line broadening and alter the many-body energy level spectrum, potentially breaking the excitation blockade. By measuring the Stark spectra of  $nD$  manifolds as a function of the potentials on the TIP and the electrodes shown in Fig. 1, we zero the electric field to below  $\sim 100$  mV/cm. This is low enough to avoid the aforementioned problems [15].

The system’s magnification factor is determined by the combined ion-lensing effects of the TIP, pulsed to about 400 V, and the MCP front plate, held at  $-800$  V. To calibrate the magnification, we scan the focused 480 nm beam laterally across the MCP field of view by using a mirror with a piezo actuator on the horizontal axis. Using the known physical displacement of the beam, we determine the scale in the MCP picture. We find a linear magnification factor of  $45\times$  between the excitation region and the MCP front surface.  $1\text{ }\mu\text{m}$  in the excitation region corresponds to 2.2 pixels in the digital CCD images, with an uncertainty of 10%.

The procedure of data acquisition and processing begins with taking 10 000 CCD images of the MCP phosphor screen, each image showing the ion impact positions for a single experimental cycle [as in Fig. 2(a)]. A CCD image consists of these blips plus background noise from the camera. To eliminate the background, we determine the maximum background level and subtract it from the image, setting all negatives to zero. This procedure yields filtered images, denoted by  $X$  [Fig. 2(b)]. The autocorrelation of each filtered image is calculated and is denoted  $A$ . The individual autocorrelations  $A$  are then added to construct  $\bar{A}$  [Fig. 2(d)]. We can write this as follows, by using subscripts for the pixel coordinates and superscript  $\alpha$  to enumerate the images:

$$A_{i,j}^{\alpha} = f(i, j, N, M) \sum_{n,m} X_{n,m}^{\alpha} X_{n-i, m-j}^{\alpha}, \quad (1)$$

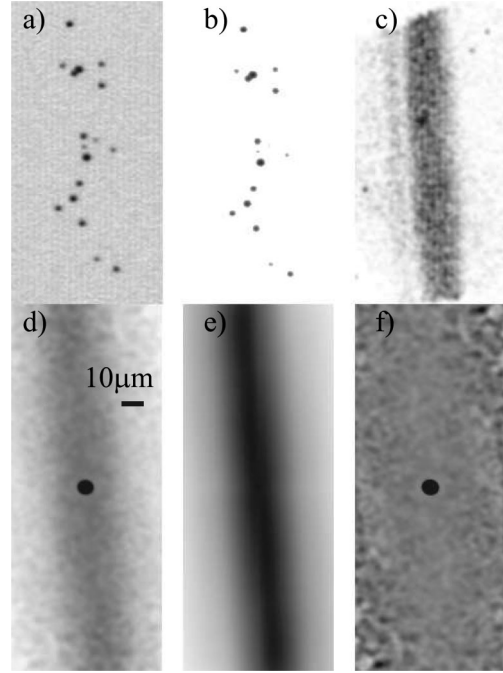


FIG. 2. Stages in the image analysis process, using state  $44D_{5/2}$ . All have the same scale. (a) Raw image (cropped), (b)  $X$ , filtered image, (c) sum of filtered images, (d)  $\bar{A}$ , sum of autocorrelations, (e)  $B$ , autocorrelation of the sum of images, (f)  $\bar{A}^1$ , normalized autocorrelation.

$$\bar{A}_{i,j} = \sum_{\alpha} A_{i,j}^{\alpha}, \quad (2)$$

where

$$f(i, j, N, M) = \frac{NM}{(N-i)(M-j)}, \quad (3)$$

$N \times M$  is the image size, and  $(i, j)$  is the displacement. The normalization factor  $f$  eliminates finite-array effects in Eqs. (2) and (4), as it causes flat images to have flat autocorrelation functions rather than pyramidal ones.

The signal  $\bar{A}$  has three main structures: a central peak due to the correlation of a blip with itself, an overall cigar shape due to the geometry of the excitation region, and structure due to correlations between ion positions. It is this third structure that we wish to isolate in our analysis. The raw autocorrelation  $\bar{A}$  is useful for qualitative analysis, as it is the easiest to interpret by eye. However, for quantitative analysis we must eliminate the shape of the beam. To do so we first sum the images [Fig. 2(c)] and take the autocorrelation [Fig. 2(e)]:

$$B_{i,j} = f(i, j, N, M) \sum_{n,m} \left( \sum_{\alpha} X_{n,m}^{\alpha} \right) \left( \sum_{\beta} X_{n-i, m-j}^{\beta} \right). \quad (4)$$

The autocorrelation  $B$  does not contain any information about Rydberg-Rydberg correlations but still shows the overall shape of the excitation region. This allows us to divide out the beam shape by defining a normalized  $\bar{A}^1$ :

$$\bar{A}_{i,j}^1 = \bar{A}_{i,j}/N_p B_{i,j}, \quad (5)$$

where  $N_p$  is the number of pictures in the data set. The normalization of  $\bar{A}^1$  is such that a value  $>1$  ( $<1$ ) should indicate a correlation (anticorrelation) of ion positions.

We take data at several combinations of red and blue laser powers. For the intensity of the lower transition beam we use intensities of  $1.7I_{\text{sat}}$  and  $3.4I_{\text{sat}}$ , where the saturation intensity  $I_{\text{sat}} = 1.6 \text{ mW/cm}^2$ . For each of these intensities we measure the atom number as a function of the intensity of the upper transition beam and observe saturation behavior as in Ref. [8]. To acquire images for the autocorrelation analysis described above, we select several intensities of the upper transition beam around and beyond the knee of the measured saturation curves. We find that the autocorrelations nearest the knee tend to show the clearest correlation-induced structures.

Figure 3 shows  $\bar{A}$  measured for states  $44D_{5/2}$ ,  $60D_{5/2}$ , and  $70D_{5/2}$ . For all three states, we observe a ring-shaped dip around the central self-correlation peak in the autocorrelation. Such dips are present in most of our data, with the degree of visibility depending on excitation parameters. The absence of dips in some data indicates that they are not artifacts of the imaging or image processing. We find that laser frequency fluctuations can make the dips change in depth and diameter. Furthermore, laser power affects the results, as described below.

To quantitatively compare the autocorrelations  $\bar{A}^1$  of different states, in Fig. 4 we plot  $I(r)$ , defined as the angular average of  $\bar{A}^1$ .  $I(r)$  is analogous to the radial autocorrelation function calculated in Ref. [6]. The self-term fills the region  $r < 5 \mu\text{m}$ . We do not remove the self-term due to the risk of producing a false blockade signal. Between 5 and  $10 \mu\text{m}$ , each curve has a dip indicating an anticorrelation in Rydberg atom positions, as was qualitatively observed in Fig. 3. The minima of  $I(r)$  do not approach zero in part because we are projecting a three-dimensional sample onto the detector plane, which reduces the visibility for even a perfect blockade.

Figure 4 shows that the blockade radius increases with principal quantum number  $n$ . However, there is no obvious choice for a method to measure a blockade radius from

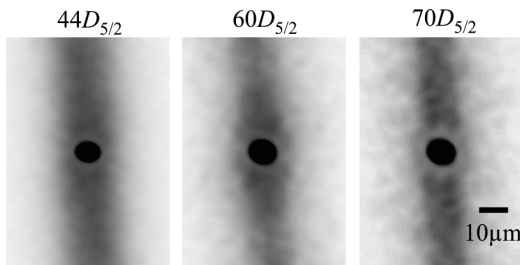


FIG. 3. Autocorrelations  $\bar{A}$  for  $44D_{5/2}$ ,  $60D_{5/2}$ , and  $70D_{5/2}$ . In the data sets shown we use a laser intensity of  $3.4I_{\text{sat}}$  for the lower transition and the lowest intensity setting (nearest the saturation knee) for the upper transition.

each curve, as the curve's shape is determined by both the blockade-induced dip and the self-term.

To determine a good measure for the blockade radius, we simulate the excitation-blockade process for our geometry and  $z$ -projection conditions, by using a stochastic, nonquantum model. We find that the inflection point after the minimum of each  $I(r)$  curve is close to the input hard-sphere blockade radius. We thus use this inflection point as our measure of the blockade radius. We note that in the simulations the self-term diminishes the dip depth and can shift the dip position. If the input blockade radius is close to the self-term width, the radius indicated by the inflection point is  $1\text{--}2 \mu\text{m}$  higher than the blockade radius. When the blockade radius is much larger than the self-term width, the inflection point method underestimates the input blockade radius by  $\lesssim 1 \mu\text{m}$ .

For the states  $44D_{5/2}$ ,  $60D_{5/2}$ , and  $70D_{5/2}$  we measured the radii on nine, six, and nine curves. One additional curve was discarded for  $70D_{5/2}$ ; although its dip minimum was consistent with other data, the position of its inflection point was unclear. Five additional curves for  $44D_{5/2}$  were thrown out because there was no dip, as discussed below. The measured blockade radii are shown in Fig. 5. The error bars indicate the 10% uncertainty from the magnification calibration; this systematic uncertainty dominates the uncertainty due to measurement statistics by a factor of at least 2.

In Fig. 5, we compare the measurements to predictions based on an excitation bandwidth  $\delta\nu_L$  ranging from 5 to 12 MHz and interaction strengths as determined from Ref. [15]. The blockade radius for the van der Waals interaction has been calculated to be

$$r_b \approx \left[ \frac{\Delta \tilde{W}^{(2)}(n^*)^{11}}{h(\delta\nu_L)} \right]^{1/6}, \quad (6)$$

where  $n^* = n - \delta_l$  is the effective principal quantum number,  $\delta_l$  is the quantum defect, and  $\Delta \tilde{W}^{(2)}$  is a scaled, second-order, state-dependent van der Waals coefficient

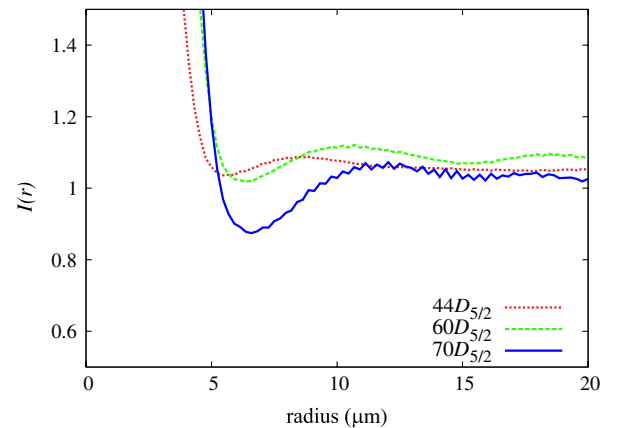


FIG. 4 (color online). Angular average of  $\bar{A}^1$ ,  $I(r)$ , for  $44D_{5/2}$ ,  $60D_{5/2}$ , and  $70D_{5/2}$ . Curves correspond to images in Fig. 3.



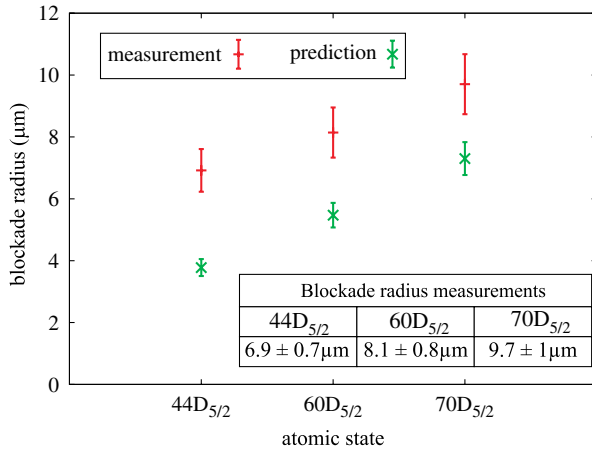


FIG. 5 (color online). Comparison of blockade radius measurements (+) with predictions (×) based on Ref. [15].

defined in Ref. [15].  $\Delta\tilde{W}^{(2)}$  is scaled such that it would be independent of  $n^*$  in the absence of resonant level shifts. The assumed value for  $\delta\nu_L$  has little effect due to the sixth-root dependence.

Figure 5 shows that the measured blockade radii are within a factor of 2 of the predictions. Further, the amount by which the blockade radius increases between the probed  $n$  levels is as expected. The measured blockade radii exceed the calculated radii by 2–3 μm. The difference may be because Eq. (6) models the interaction between two atoms and excludes many-body effects [3]. Ates *et al.* have previously seen evidence that theory based on pairwise interactions underestimates the blockade radius [7].

To test if atomic motion or the degree of excitation saturation modifies the observed correlation behavior, we vary laser powers, excitation pulse duration, and field extraction delays. In general, increasing the laser power, or the excitation duration at constant power, diminishes the dip depth (defined as the curve asymptote minus the dip minimum). For instance, increasing the excitation duration for state 70D<sub>5/2</sub> from 100 to 400 ns causes the dip depth to decrease from 0.24 to 0.04. This behavior could be caused by an increased  $z$  depth of the saturated part of the excitation region. In our simulations the degree to which the dip depth is diminished depends on the assumed beam focus quality. Adding wings to a Gaussian focus, as suggested by Fig. 2(c), yields better qualitative agreement with our data.

Laser power has a greater effect for the case of excitation to 44D<sub>5/2</sub> than for the other states: In five  $I(r)$  curves the dip disappeared entirely. We expect that this is partly due to saturating the atomic transition for 44D<sub>5/2</sub> more strongly than for 60D<sub>5/2</sub> or 70D<sub>5/2</sub>. It is also possible that, of the three states we studied, 44D<sub>5/2</sub> is the most susceptible to laser parameters due to having the shallowest dip, closest to the radius of the self-term. Another possibility is that the blockade efficiency is diminished due to the proximity of the Förster resonance, as suggested by Refs. [3,16].

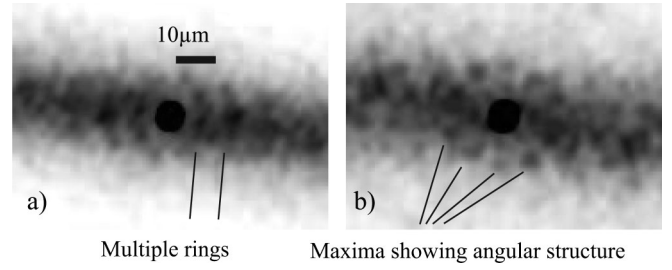


FIG. 6. Some autocorrelations ( $\bar{A}$ ) showing possible long-range and angular structure for state 44D<sub>5/2</sub>.

By varying the delay between excitation and field ionization, we test the longevity of the correlations. They are remarkably long-lived. The dip depth decreases by about half over 10 μs, despite possible atomic motion and ionization during this time [17,18]. This result awaits a future theoretical explanation.

Some of our data, using linear laser polarization and a few megahertz of detuning, show additional structures. The autocorrelation in Fig. 6(a) exhibits multiple rings, indicating long-range Rydberg-Rydberg correlations. The autocorrelation in Fig. 6(b) hints at multiple maxima in a ring about the center, indicating possible angular dependence of the Rydberg-Rydberg correlation function. There have been predictions of crystal-like structure in Rydberg systems [19], but the detailed excitation conditions are important in generating these structures. At present we are working to improve our experimental control in order to systematically study these effects.

In summary, we have obtained spatially resolved images of blocked Rydberg atom samples and evaluated the Rydberg-Rydberg correlation function. Having observed a blockade, we measured the blockade radius for several quantum states. We have also tested the dependence of the blockade on parameters such as laser power, excitation duration, and detection delay. Future work could include investigation of longer-range correlation structures, extending beyond one blockade radius, as in Fig. 6. One could further attempt to excite a Rydberg crystal as proposed in Ref. [19].

We acknowledge the help of Dr. Brenton Knuffman in the design phase of the experiment. This work was supported by the NSF (PHY-0855871), AFOSR (FA9550-10-1-0453), and FOCUS (PHY-0114336).

- 
- [1] I. Mourachko *et al.*, *Phys. Rev. Lett.* **80**, 253 (1998).
  - [2] P.J. Tanner *et al.*, *Phys. Rev. Lett.* **100**, 043002 (2008).
  - [3] K.C. Younge *et al.*, *Phys. Rev. A* **79**, 043420 (2009).
  - [4] M.D. Lukin *et al.*, *Phys. Rev. Lett.* **87**, 037901 (2001).
  - [5] D. Jaksch *et al.*, *Phys. Rev. Lett.* **85**, 2208 (2000).
  - [6] F. Robicheaux and J.V. Hernández, *Phys. Rev. A* **72**, 063403 (2005).
  - [7] C. Ates *et al.*, *Phys. Rev. A* **76**, 013413 (2007).



- 
- [8] D. Tong *et al.*, *Phys. Rev. Lett.* **93**, 063001 (2004).
  - [9] A. Reinhard, K. C. Younge, and G. Raithel, *Phys. Rev. A* **78**, 060702 (2008).
  - [10] A. Reinhard *et al.*, *Phys. Rev. Lett.* **100**, 233201 (2008).
  - [11] C. S. E. van Ditzhuijzen *et al.*, *Phys. Rev. Lett.* **100**, 243201 (2008).
  - [12] T. J. Carroll *et al.*, *Phys. Rev. Lett.* **93**, 153001 (2004).
  - [13] A. Gaetan *et al.*, *Nature Phys.* **5**, 115 (2009).
  - [14] E. Urban *et al.*, *Nature Phys.* **5**, 110 (2009).
  - [15] A. Reinhard *et al.*, *Phys. Rev. A* **75**, 032712 (2007).
  - [16] T. G. Walker and M. Saffman, *J. Phys. B* **38**, S309 (2005).
  - [17] T. Amthor *et al.*, *Phys. Rev. Lett.* **98**, 023004 (2007).
  - [18] F. Robicheaux, *J. Phys. B* **38**, S333 (2005).
  - [19] T. Pohl, E. Demler, and M. D. Lukin, *Phys. Rev. Lett.* **104**, 043002 (2010).

# Angular-momentum couplings in long-range $\text{Rb}_2$ Rydberg molecules

D. A. Anderson, S. A. Miller, and G. Raithel

*Department of Physics, University of Michigan, Ann Arbor, Michigan 48109, USA*

(Received 8 September 2014; published 31 December 2014)

We study angular-momentum couplings in  $^{87}\text{Rb}_2$  Rydberg molecules formed between a Rydberg and  $5S_{1/2}$  ground-state atom. We use a Fermi model that includes  $S$ -wave and  $P$ -wave singlet and triplet scattering of the Rydberg electron with the  $5S_{1/2}$  atom, along with the fine-structure coupling of the Rydberg atom and hyperfine-structure coupling of the  $5S_{1/2}$  atom. We discuss the effects of these couplings on the adiabatic molecular potentials. We obtain bound-state energies, lifetimes, and electric and magnetic dipole moments for the vibrational ground states of the  $^{87}\text{Rb}(nD + 5S_{1/2})$  molecules in all adiabatic potentials, with fine and hyperfine structure included. The hyperfine structure gives rise to mixed singlet-triplet potentials. We also study the effect of the hyperfine structure on the deep  $^3S$ -wave- and  $^3P$ -wave-dominated adiabatic molecular potentials, which support high- $\ell$   $^{87}\text{Rb}_2$  Rydberg molecules.

DOI: [10.1103/PhysRevA.90.062518](https://doi.org/10.1103/PhysRevA.90.062518)

PACS number(s): 33.15.-e, 33.80.Rv, 31.10.+z, 32.80.Ee

## I. INTRODUCTION

Rydberg molecules formed by the low-energy scattering of a Rydberg electron and a ground-state atom constitute a distinct class of molecular states that have in recent years become the subject of significant theoretical and experimental interest. Developments include studies of diatomic Rydberg molecules in low-angular-momentum Rydberg  $S$  states [1,2],  $P$  states [3], and  $D$  states [4,5], the realization of coherent bonding and dissociation of  $S$ -type molecules [6], and the first observation of a permanent electric dipole moment in a homonuclear molecule [7]. Polyatomic Rydberg molecules have also been generated [8] and employed in a demonstration of the continuous transition between a few-body to many-body regime in an ultracold quantum gas [9].

The theoretical framework for these molecules is generally well established. The interaction between a low-energy Rydberg electron and ground-state atom can be described using a Fermi pseudopotential approach [10–12]. In the Fermi model, the ground-state atom is treated as a  $\delta$ -function perturber of the Rydberg-electron wave function, resulting in oscillatory potential curves with localized minima capable of sustaining bound molecular states. In alkali systems, the potential curves are strongly affected by low-energy  $^3S$ -wave and  $^3P$ -wave electron-atom scattering resonances [13–15]. The influence of these scattering resonances on the potentials has been studied in  $\text{Rb}_2$ . The  $^3S$  interaction leads to so-called trilobite molecules [12], which are very long range (their size is on the order of  $n^2$ , where  $n$  is the principal quantum number of the Rydberg level). The  $^3P$  interaction produces potentials [16] that are about an order of magnitude deeper and about a factor of five shorter range than the trilobite potentials. The molecular potentials, wave functions, and electric dipole moments for both  $\text{Rb}_2$  and  $\text{Cs}_2$  have also been calculated using a Green's function approach, accounting for the finite size of the perturbing ground-state atom via an effective short-range electron-atom interaction potential [17,18].

In addition to the electron-atom scattering interaction, the molecular potentials and properties of long-range Rydberg molecules are dependent on the Rydberg-atom wave function as well as the angular-momentum couplings of the Rydberg- and ground-state constituents. Rydberg molecules exhibit

a broad range of different angular momentum coupling schemes. For low- $\ell$  Rydberg molecules ( $\ell \lesssim 2$  in rubidium), the angular-momentum coupling configurations span three Hund's cases [(a)–(c)], dictated by the relative strength of the Rydberg atom's fine-structure coupling compared to that of the  $e^- + 5S_{1/2}$  scattering interaction. The  $\text{Rb}(nD_j + 5S_{1/2})$  molecules are unique among the low- $\ell$  molecules because their Rydberg fine-structure couplings are comparable to the scattering interaction strength, and they fall anywhere between two Hund's cases (a) and (c) by a mere change in principal quantum number  $n$ . For high- $\ell$  Rydberg molecules, the molecular binding interaction is stronger than the fine-structure coupling, and is comparable to the hyperfine coupling of the ground-state perturber. Inclusion of the  $5S_{1/2}$  hyperfine coupling in the model generates additional adiabatic potentials of mixed triplet and singlet character. For both high- and low- $\ell$  molecules, the hyperfine structure results in additional adiabatic potentials deep enough to sustain bound states.

In this work we present a study on the influence of angular-momentum couplings on the properties of long-range Rydberg molecules. We first describe a Fermi model for Rydberg molecules with the relevant angular-momentum couplings included. In our analysis we include singlet and triplet  $S$ - and  $P$ -wave scattering. By selectively enabling the different interactions in the model, the effects of each of these individual interactions on the adiabatic molecular potentials are revealed. Typical vibrational-state wave functions, binding energies, lifetimes, and dipole moments are discussed with an emphasis on the role of angular-momentum couplings. We conclude with describing hyperfine effects on the relatively deeply bound trilobite Rydberg molecules [12].

## II. FERMİ MODEL

We describe diatomic Rydberg molecules with a Fermi model [10,11] taking into account the angular-momentum couplings in the Rydberg atom and perturbing ground-state atom system whose strengths are comparable to the Rydberg  $e^- +$  perturber interaction. A schematic of the relevant couplings is shown in Fig. 1(a). The perturbing  $^{87}\text{Rb } 5S_{1/2}$  atom is located at a position  $Z$  from the ionic core of the Rydberg atom,

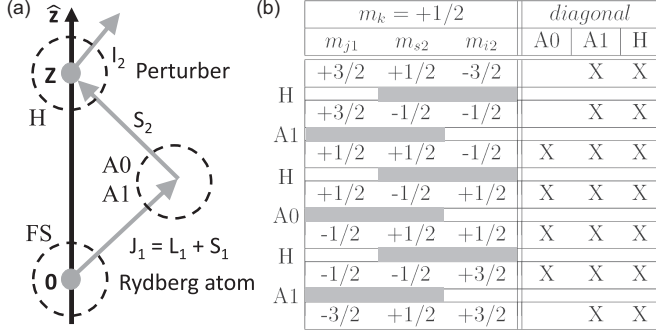


FIG. 1. (a) Angular momentum coupling scheme for diatomic  $^{87}\text{Rb}(nD_j + 5S_{1/2}, F)$  Rydberg molecules. The relevant interactions are circled. Here, A0 and A1 denote  $e^- + 5S_{1/2}$  scattering interactions involving the  $m_{i1} = 0$  ( $S$ -wave and  $P$ -wave) and the  $|m_{i1}| = 1$  ( $P$ -wave only) components of the Rydberg electron's state, respectively, and H denotes the hyperfine interaction of the  $5S_{1/2}$  atom. FS denotes the fine-structure coupling. (b) States in the  $m_k = m_{j1} + m_{s2} + m_{i2} = +1/2$  subspace and their relevant interactions. In the left column, horizontal gray bars are placed between  $(m_{j1}m_{s2})$  or  $(m_{s2}m_{i2})$  for states in neighboring rows that are coupled by either the scattering or the hyperfine interaction. The Xs in the right column indicate the interactions that have terms diagonal in  $(m_{j1}m_{s2}m_{i2})$ .

which is fixed at the origin. The internuclear axis is along  $\hat{z}$ . The orbital and spin angular momenta of the Rydberg atom are denoted by  $L_1$  and  $S_1$ , respectively. For  $L_1 \leq 2$  and within the  $n$  range of interest, the Rydberg-atom fine structure is of the same order as the  $e^- + 5S_{1/2}$  scattering interaction and is therefore included. The hyperfine coupling of the electron spin  $S_2$  and nuclear spin  $I_2$  of the perturbing  $5S_{1/2}$  ground-state atom is also included, because it is several GHz and is, in most cases, stronger than the Rydberg electron's fine-structure coupling and the  $e^- + 5S_{1/2}$  scattering interaction. The orbital angular momentum of the  $5S_{1/2}$  atom is  $L_2 = 0$ . The Rydberg atom's hyperfine structure decreases as  $n^{-3}$ ; for the lowest  $S$  states relevant to our work it does not exceed several MHz [19,20], and it is much lower for higher- $\ell$  states [21]. The Rydberg atom's hyperfine structure is therefore not included.

For a Rydberg atom with its ionic core at the origin and the Rydberg electron located at  $\mathbf{r}$ , and with a  $5S_{1/2}$  atom located at  $Z\hat{z}$ , the Hamiltonian is written as

$$\begin{aligned} \hat{H}(\mathbf{r}, Z) = & \hat{H}_0 + \sum_{i=S,T} 2\pi A_s^i(k) \delta^3(\mathbf{r} - Z\hat{z}) \hat{\mathbb{I}}_i \\ & + \sum_{i=S,T} 6\pi A_p^i(k) \delta^3(\mathbf{r} - Z\hat{z}) \hat{\nabla} \cdot \hat{\nabla} \hat{\mathbb{I}}_i \\ & + \hat{\mathbf{A}}\hat{\mathbf{S}}_2 \cdot \hat{\mathbf{I}}_2. \end{aligned} \quad (1)$$

In the unperturbed Rydberg Hamiltonian  $\hat{H}_0$  we use published quantum defects [22], which account for core penetration and fine structure. For  $\ell \geq 5$  we use the fine-structure correction of hydrogen as well as a small quantum defect to account for core polarization,  $\delta_\ell = 0.75\alpha_D/\ell^5$  [22], with a dipolar polarizability for  $\text{Rb}^+$  of  $\alpha_D = 9.023$  atomic units [23]. The energy-dependent  $S$ -wave ( $\ell = 0$ ) and  $P$ -wave ( $\ell = 1$ ) scattering lengths ( $A_s$  and  $A_p$ , respectively) have the general form  $A_l(k) = -\tan \delta_l/k^{2l+1}$ , where  $\delta_l$  is the  $l$ - and

energy-dependent scattering phase shift. For the calculations in the present work we use nonrelativistic scattering phase shifts  $\delta_{l=0}$  and  $\delta_{l=1}$  provided by I. I. Fabrikant based on Ref. [17]. The electron momentum is given by  $k = \sqrt{-1/n_0^* + 2/r}$  (atomic units) in the classically allowed range of the Rydberg electron and  $k = 0$  elsewhere. Here,  $n_0^*$  is the effective Rydberg quantum number of the level of interest. To account for configuration interactions, we employ basis sets  $\{|n, L_1, J_1, m_{j1}\rangle \otimes |m_{s2}, m_{i2}\rangle\}$  that include all Rydberg levels with effective quantum numbers  $|n^* - n_0^*| \lesssim 2.5$ . For the Rydberg atom, all  $L_1$ ,  $J_1$ , and  $m_{j1}$  are included (as in Ref. [24]), and for the perturber atom all  $m_{s2}$  and  $m_{i2}$  are included. The singlet ( $S$ ) and triplet ( $T$ ) channels of the  $e^- + 5S_{1/2}$  scattering interaction include projectors  $\hat{\mathbb{I}}_{(S,T)}$ , defined as  $\hat{\mathbb{I}}_T = \hat{\mathbf{S}}_1 \cdot \hat{\mathbf{S}}_2 + \frac{3}{4}$ , which has an eigenvalue of one (zero) for the triplet (singlet) states, and  $\hat{\mathbb{I}}_S = \hat{\mathbb{I}} - \hat{\mathbb{I}}_T$ . The operators  $\hat{\mathbf{S}}_1$  and  $\hat{\mathbf{S}}_2$  are the spins of the Rydberg electron and  $5S_{1/2}$  atom, respectively, and  $\hat{\mathbb{I}}$  is the identity operator. The last term in Eq. (1) accounts for the hyperfine interaction of the perturber. The  $^{87}\text{Rb}$   $5S_{1/2}$  perturber atom has nuclear spin  $\hat{\mathbf{I}}_2$  with  $I_2 = 3/2$ , and hyperfine levels  $F_- = 1$  and  $F_+ = 2$ , with a hyperfine coupling parameter  $A = h \times 6.8 \text{ GHz}/F_+ = h \times 3.4 \text{ GHz}$  (in SI units).

Only levels with  $m_{\ell 1} = 0, \pm 1$  components have nonvanishing wave functions or wave function gradients on the internuclear axis. The  $S$ -wave interactions couple Rydberg states with  $m_{\ell 1} = 0$  components. The  $P$ -wave interactions couple states with  $m_{\ell 1} = 0$  components through the radial derivative of the Rydberg wave function, and states with  $m_{\ell 1} = \pm 1$  components through the polar-angle derivative of the wave function. The electron scattering term in Eq. (1) conserves  $m_{j1} + m_{s2}$ , while the hyperfine term conserves  $m_{s2} + m_{i2}$ . The full Hamiltonian conserves  $m_k := m_{j1} + m_{s2} + m_{i2}$ . Hence, the Hilbert space can be broken up into subspaces of fixed quantum number  $m_k$ . As an example, the subspace for  $m_k = +1/2$  and its couplings via the  $S$ -wave,  $P$ -wave, and hyperfine interactions is shown in Fig. 1(b). The gray bars in Fig. 1(b) illustrate that the couplings are organized in an interlaced block-diagonal structure in the magnetic quantum numbers. Since the couplings via the scattering terms require  $|m_{j1}| \leq 3/2$ , the  $^{87}\text{Rb}_2$  Rydberg molecules have  $|m_k| \leq 7/2$ .

### III. ADIABATIC POTENTIALS

Adiabatic molecular potentials  $V_i(Z)$  ( $i$  is an arbitrary label) are obtained by diagonalizing the Hamiltonian in Eq. (1) for a grid of perturber atom positions,  $Z\hat{z}$ , through the extent of the Rydberg wave function. To highlight the effects of the different terms in Eq. (1) on  $V_i(Z)$ , in Figs. 2 and 3 we show adiabatic potentials calculated for  $D$ -type Rydberg molecules with the different interaction terms in Eq. (1) selectively turned on.

First, we consider adiabatic potentials without hyperfine coupling. Figure 2(a) shows adiabatic potentials for the  $31D + 5S_{1/2}$  molecule with only the  $^3S$  interaction turned on and no fine-structure coupling. This results in three degenerate oscillatory potentials, one corresponding to each triplet state, and a flat potential corresponding to the singlet state (which has no  $^3S$  interaction). The triplet potential curves are similar to those calculated in Ref. [12], in which the  $S$ -wave scattering length  $-\tan \delta_s/k$  is taken to first order in

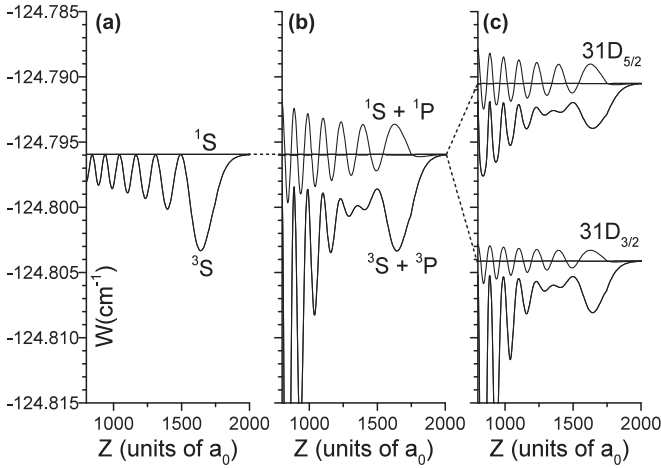


FIG. 2. Adiabatic potentials for the  $31D + 5S_{1/2}$  molecule with the following interaction terms in Eq. (1) selectively turned on (without the hyperfine interaction): (a)  $^3S$  scattering, (b)  $^3S$ ,  $^1S$ ,  $^3P$ , and  $^1P$  scattering, and (c)  $^3S$ ,  $^1S$ ,  $^3P$ , and  $^1P$  scattering with fine-structure coupling.

the electron momentum [11]. With an appropriate choice of the zero-energy  $S$ -wave scattering length, the  $^3S$  interaction reproduces measured binding energies of vibrational ground states of  $S$ -type Rydberg molecules [1]. Similarly, the  $^3S$  interaction with the addition of the fine structure reproduces vibrational ground states of  $D$ -type Rydberg molecules [4]. The effect of the fine-structure coupling on the molecules is discussed further below.

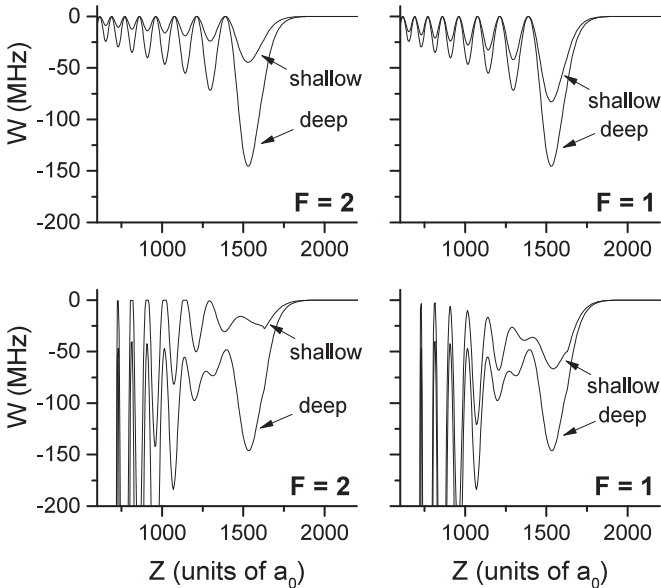


FIG. 3. Binding adiabatic potentials for the  $^{87}\text{Rb}(30D_{3/2} + 5S_{1/2}, F = 1, 2)$  molecules with fine and hyperfine structure included, with  $^3S$  scattering only (top row) and with  $^3S$ ,  $^1S$ ,  $^3P$ , and  $^1P$  scattering (bottom row). The hyperfine coupling leads to the shallow adiabatic potentials of mixed singlet-triplet character. The shallow potentials are different for the  $F = 1$  and  $F = 2$  hyperfine levels. The deep potentials have pure triplet character and do not depend on the hyperfine structure.

Figure 2(b) shows adiabatic potentials resulting from the  $^3S$ ,  $^1S$ ,  $^3P$ , and  $^1P$  scattering interactions turned on and no fine-structure coupling. At smaller internuclear separations, the influence of  $P$ -wave scattering becomes more significant due to higher electron energies closer to the Rydberg atom's ionic core (and therewith larger wave function gradients). The effect of the  $^3P$  scattering interaction is evident in Fig. 2(b), where the inner wells become notably deeper, while the outermost well remains relatively unaffected. The increasing contribution of  $P$ -wave scattering at smaller  $Z$  generates deep molecular potentials. The repulsive  $^1S$  and attractive  $^1P$  scattering interactions turn the flat singlet potential in Fig. 2(a) into an oscillatory singlet potential with maxima above and wells below the dissociation threshold, as seen in Fig. 2(b).

Figure 2(c) shows adiabatic potentials resulting from the addition of the fine-structure coupling of the Rydberg atom to the  $^3S$ ,  $^1S$ ,  $^3P$ , and  $^1P$  scattering interactions. The top and bottom plots show  $31D_j + 5S_{1/2}$  potentials for the  $j = 5/2$  and  $3/2$  fine-structure states, respectively. Qualitatively, the fine-structure coupling splits the molecular bonding strength (adiabatic-potential depth) of the fine-structure-free case between the two fine-structure levels, resulting in less deep potentials. The splitting ratio depends on which Hund's case is more relevant (see Sec. V).

The hyperfine interaction of the ground-state perturber in Eq. (1) mixes the singlet and some triplet scattering channels, resulting in the replacement of the pure singlet potentials in Fig. 2 with shallow adiabatic potentials of mixed singlet-triplet character. As an example, in Fig. 3 we show the adiabatic potentials for the  $30D_{3/2} + 5S_{1/2}, F = 1, 2$  molecules including the hyperfine interaction. The deep adiabatic potentials are of pure triplet character and are unaffected by the hyperfine interaction of the  $5S_{1/2}$  atom. The  $F = 1$  shallow, mixed singlet-triplet potentials are always deeper than the  $F = 2$  shallow potentials. The shallow potentials can typically sustain a few bound states that should be observable in experiments.

#### IV. QUASIBOUND MOLECULAR STATES AND LIFETIMES

Due to the lack of an inner potential barrier, the molecular vibrational states have the character of metastable scattering resonances in potentials that are unbound on the inside. Figure 4 shows the (deep) adiabatic potential for the  $^{87}\text{Rb}(31D_{3/2} + 5S_{1/2}, F = 2)$  molecule and its quasibound states. These are qualitatively similar to those of  $S$ -type molecules [8]. The molecular wave functions consist of low-amplitude standing waves formed by outgoing and reflected incoming waves in the region  $Z \lesssim 1000a_0$ , and a high-amplitude, resonantly enhanced portion in the outer adiabatic-potential wells at  $Z \sim 1500a_0$ . The latter are identified with quasibound molecular vibrational states that are metastable against tunneling-induced decay (decay into the region  $Z \lesssim 1000a_0$ ).

The resonances are found by computing the wave function phase at a fixed location in the unbound region (we use  $Z = 300a_0$ ) as a function of energy  $W$ . The phase and its derivative are plotted as a function of energy in the right and middle panels of Fig. 4, respectively. The quasibound molecular states occur at energies at which the phase undergoes sudden changes of  $\Delta\Phi = \pi$ , and are centered at energies where the derivative of the phase is maximal (circles in the middle panel of Fig. 4).



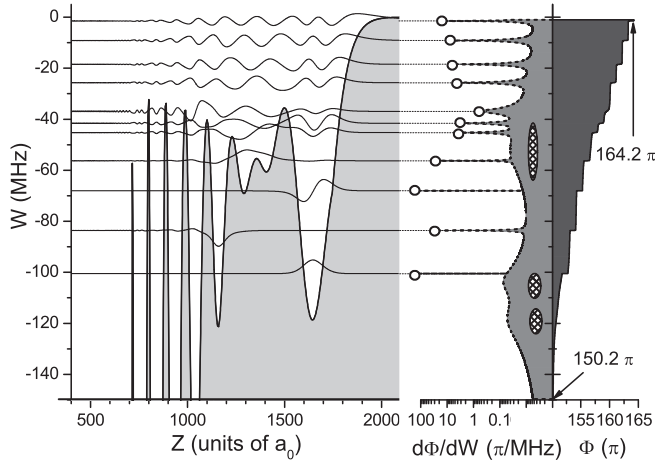


FIG. 4. (Left) Adiabatic potential of the  $^{87}\text{Rb}(31D_{3/2} + 5S_{1/2}, F=2)$  Rydberg molecule and vibrational wave functions. Each wave function corresponds to a narrow scattering resonance, characterized by a sudden change in the wave function phase by  $\pi$  in the unbound, inner region of the potential. (Right) Wave function phase at location  $Z = 300a_0$ . (Middle) The maxima of  $d\Phi/dW$ , indicated by circles, are used to determine resonance widths and lifetimes. Several broad resonances (hatched regions) are spread out over the displayed energy range.

The resonances obey a single-level Breit-Wigner formula with frequency linewidths of the quasibound molecular states given by  $\Gamma_v = 2/(\hbar \times d\Phi/dW)$  [25], corresponding to lifetimes of  $\tau = (\hbar/2)d\Phi/dW$ . The lifetimes scale as the Wigner tunneling time delay [26]. Resonances with larger slopes  $d\Phi/dW$  in Fig. 4 correspond to longer-lived quasibound states. In addition to the sharp resonances there are broad resonances, as indicated by hatched regions in the middle panel of Fig. 4. While the broad resonances are not likely to cause observable effects in molecular spectra, they add to the total phase change over an energy range. For instance, within the energy range displayed in Fig. 4 the broad resonances account for a phase change of  $3\pi$  and the quasibound molecular states for a change of  $11\pi$ , corresponding to a total change of  $14\pi$ . The distinction between broad and narrow resonances may, in practice, depend on experimental parameters such as excitation bandwidth and atom temperature (which affects Frank-Condon factors).

In Table I we give the binding energies, linewidths, decay times, and average internuclear separation of the scattering resonances shown in Fig. 4. Each quasibound state is assigned a vibrational quantum number  $\nu$ , sequentially increasing from 0 for the most strongly bound state in the outermost well to 10 for the most weakly bound state. Generally, one expects bound states furthest from the dissociation threshold to have the longest lifetimes. Here, the ground and first excited states of the outermost potential well (labeled  $\nu = 0$  and 2, respectively) are well confined and have lifetimes in the range of hours and seconds, respectively. These lifetimes only reflect tunneling-induced decay. The actual lifetimes of these molecular states are, in fact, much shorter due to additional decay mechanisms, such as radiative decay of the Rydberg state and collisions with ground-state atoms [27]. An early dissociation process via the energy exchange between the

TABLE I. For the  $^{87}\text{Rb}(31D_{3/2} + 5S_{1/2}, F=2)$  Rydberg molecule, we show the vibrational quantum number  $\nu$ , binding energy, linewidth  $\Gamma_\nu$ , decay time, and bond length.

$\nu$	Energy (MHz)	Linewidth (MHz)	Decay time ( $\mu\text{s}$ )	$\langle Z \rangle$ ( $a_0$ )
0	-100.52	$1.79 \times 10^{-11}$	$8.89 \times 10^9$	1647.5
1	-83.59	$2.18 \times 10^{-2}$	7.30	1160.0
2	-68.03	$6.00 \times 10^{-8}$	$2.65 \times 10^6$	1655.3
3	-56.27	$2.37 \times 10^{-2}$	6.72	1324.0
4	-45.24	$1.48 \times 10^{-1}$	1.08	1413.0
5	-41.58	$1.87 \times 10^{-1}$	0.85	1527.9
6	-36.91	$1.01 \times 10^0$	0.16	1169.3
7	-26.58	$1.28 \times 10^{-1}$	1.24	1428.4
8	-18.48	$9.99 \times 10^{-2}$	1.59	1467.0
9	-9.14	$7.78 \times 10^{-2}$	2.05	1481.8
10	-1.48	$3.71 \times 10^{-2}$	4.29	1697.0

Rydberg electron and ground-state atom has also been used to explain shorter molecular lifetimes observed in experiments [28]. Nevertheless, the relatively long lifetimes and large Frank-Condon factors associated with these outermost states make them the easiest to isolate experimentally [1,4,9]. There are also several resonances in the inner potential wells ( $\nu = 1$  and 3) with lifetimes on the order of that of the Rydberg atom (which for  $^{87}\text{Rb } 31D_{3/2}$  is about  $20 \mu\text{s}$  in a 300 K black-body radiation field). The resonances at higher energies ( $\nu = 4 - 6$ ) exhibit shorter lifetimes because of the smaller potential barrier through which they more readily tunnel inward. Surprisingly, above these short-lived resonances additional resonances with longer lifetimes appear ( $\nu = 7 - 10$ ). Here, the inner oscillatory wells act like an aperiodic Bragg reflector of the molecular wave functions, resulting in unexpectedly long-lived resonances near the dissociation threshold. The lifetime of these states is largest when a Bragg reflection condition is met. This occurs in a range of Rydberg principal quantum numbers  $n$  at which the periodicity of the vibrational wave function approximately equals that of the Rydberg-electron wave function. This Bragg-reflection has previously been described as an internal quantum reflection process in  $S$ -type molecules [8].

## V. HUND'S CASES FOR $nD$ RYDBERG MOLECULES

Hund's coupling cases are widely used for classification of angular momentum couplings in diatomic molecules [29]. Low- $\ell$  diatomic Rydberg molecules ( $\ell \lesssim 2$  in rubidium) exhibit a variety of coupling cases, determined by the relative strength of the Rydberg atom's fine-structure coupling to the  $e^- +$  perturber scattering interaction. For  $^{87}\text{Rb}(nD_j + 5S_{1/2})$  molecules the fine-structure coupling is comparable to the scattering interaction strength. Due to this,  $D$ -type molecules trend from Hund's case (c) at large  $n$ , where the fine-structure coupling exceeds the scattering interaction strength, to Hund's case (a) for  $n \lesssim 35$ , where the scattering interaction strength exceeds the fine-structure coupling. In previous work, we observed  $^{87}\text{Rb}(nD_j + 5S_{1/2}, F=2)(\nu=0)$  molecules in transition between the two Hund's coupling cases (a) and (c) [4]. In

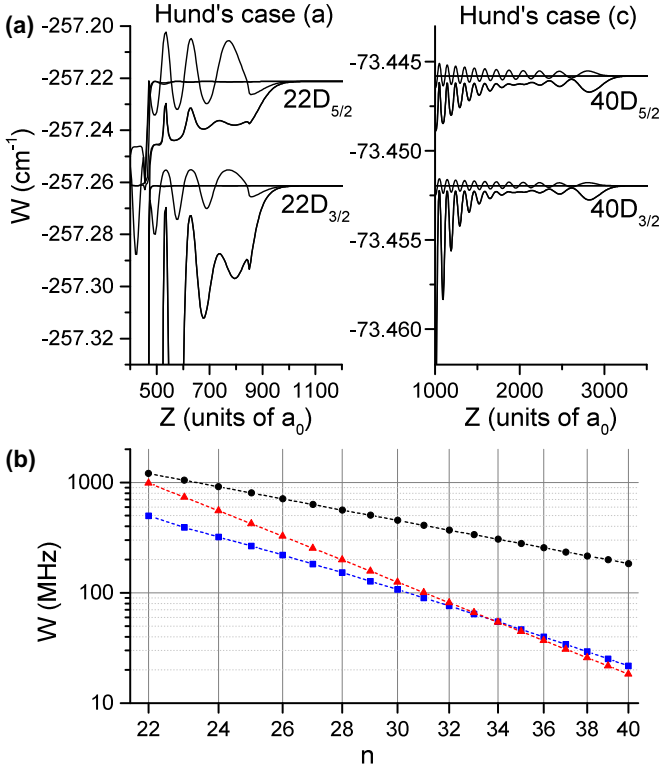


FIG. 5. (Color online) (a) Adiabatic potentials for  $^{87}\text{Rb}(22D_j + 5S_{1/2})$  (left) and  $^{87}\text{Rb}(40D_j + 5S_{1/2})$  (right) with  $^3S, ^1S, ^3P, ^1P$  interactions and no HFS interaction. (b) Binding energies for the  $v = 0$  ground vibrational state of the  $nD_{5/2} + 5S_{1/2}$  (blue squares) and  $nD_{3/2} + 5S_{1/2}$  (red triangles) molecular potentials versus  $n$ . The  $D$  fine-structure splitting is also plotted (black circles).

this section, we focus on the potentials and quasibound states of the  $^{87}\text{Rb}(nD_j + 5S_{1/2})$ ,  $j = 3/2$  and  $5/2$  molecules in the two limiting Hund's cases and in the transition regime.

Figure 5(a) shows  $V_i(Z)$  for the  $j = 3/2$  and  $5/2$  ( $22D_j + 5S_{1/2}$ ) molecules (left) and  $j = 3/2$  and  $5/2$  ( $40D_j + 5S_{1/2}$ ) molecules (right) calculated with all interaction terms in Eq. (1), excluding hyperfine-structure coupling. At high  $n$ , the molecules trend towards Hund's case (c), where the dominant adiabatic molecular potentials are reduced by the product of two Clebsch-Gordan coefficients of the type  $\langle m_\ell = 0, m_s = \pm 1/2 | j, m_j = \pm 1/2 \rangle$ . This leads to adiabatic potentials whose depths carry spin-dependent factors  $\ell/(2\ell + 1)$  for  $j = \ell - 1/2$  and  $(\ell + 1)/(2\ell + 1)$  for  $j = \ell + 1/2$  [25]. For  $nD$  ( $\ell = 2$ ) molecules at high  $n$ , the depth ratio of the potentials for  $j = 3/2$  and  $j = 5/2$  approaches  $2/3$ . This is seen in the depths of the outermost wells of the high- $n$   $j = 3/2$  and  $5/2$  ( $40D_j + 5S_{1/2}$ ) molecular potentials in Fig. 5(a). For decreasing  $n$ , the fine-structure splitting increases as  $n^{-3}$  while the scattering interaction strength increases as  $n^{-6}$ , and the molecules tend towards Hund's case (a). The  $j = 3/2$  and  $5/2$  ( $22D_j + 5S_{1/2}$ ) molecular potentials in Fig. 5 exhibit this case, where the scattering interaction strength is large compared to the fine-structure splitting. In the low- $n$  limit, the  $j = 3/2$  potential becomes notably deeper than the  $j = 5/2$  potential.

The binding energies of the vibrational ground states in the outermost potential wells,  $W_{i,v=0}$ , closely track the depth of

those wells and therefore mirror the transition of the molecule between the two Hund's cases. In Fig. 5(b), we plot  $W_{i,v=0}$  for the  $j = 3/2$  and  $5/2$  ( $nD_j + 5S_{1/2}$ ) molecules for a range of  $n$  from Hund's case (a) (low- $n$ ) to Hund's case (c) (high- $n$ ). In the high- $n$  limit, the molecular binding energies  $W_{i,v=0}$  for both fine-structure levels approximately scale as  $n^{-6}$ , inversely with the atomic volume. In the low- $n$  limit, the lowest binding energy for the lower fine-structure level ( $j = 3/2$ ) is larger and continues to scale as  $\sim n^{-6}$ , while that of the upper fine-structure level ( $j = 5/2$ ) trends towards a  $\sim n^{-3}$  scaling, approaching the scaling of the fine-structure splitting. For the  $\text{Rb}(nD_j + 5S_{1/2})$  molecules, the binding energies of the vibrational ground states in the outermost potential wells for  $j = 3/2$  and  $j = 5/2$  are approximately equal at  $n = 34$  [see Fig. 5(b)]. Further, due to the described Hund's case behavior, at sufficiently low  $n$  the inner wells of adiabatic potentials of the  $nD_{3/2} + 5S_{1/2}$  molecule become deep enough to support vibrational states that are more deeply bound and long lived than the ground states of the outermost well of the  $nD_{5/2} + 5S_{1/2}$  potentials.

## VI. ELECTRIC AND MAGNETIC DIPOLE MOMENTS

Rydberg molecules present the only known case of homonuclear molecules with permanent electric dipole moments [7,12]. For high- $\ell$  Rydberg molecules dipole moments on the order of  $10^3 ea_0$  are predicted to exist [12]. Smaller permanent dipole moments arise in low- $\ell$   $S$ -,  $P$ -, and  $D$ -type molecules from fractional admixing of high- $\ell$  state character. Permanent electric dipole moments of  $\sim 0.5ea_0$  have previously been measured in rubidium  $S$ -type Rydberg molecules [7]. Dipolar cesium Rydberg molecules with electric dipole moments of  $\sim 5 - 50ea_0$  [2] have also been prepared. In this section we calculate both the electric and magnetic dipole moments for  $nD$  Rydberg molecules, with all terms in the Hamiltonian in Eq. (1) included.

We obtain the adiabatic electric [ $d_{i,z}(Z)$ ] and magnetic [ $\mu_{i,z}(Z)$ ] dipole moments in the diagonalization of Eq. (1). The dipole moments of a molecular state  $v$  follow from the expectation values of  $d_{i,z}(Z)$  and  $\mu_{i,z}(Z)$  over the vibrational wave function densities,

$$d_{i,v} = \int |\Psi_{i,v}(Z)|^2 d_{i,z}(Z) dZ$$

$$\mu_{i,v} = \int |\Psi_{i,v}(Z)|^2 \mu_{i,z}(Z) dZ. \quad (2)$$

Electric dipole moments for the ground vibrational states of the  $j = 3/2$  and  $5/2$   $^{87}\text{Rb}(nD_j + 5S_{1/2}, F = 1, 2)$  deep (pure triplet) and shallow (mixed singlet-triplet) molecular potentials are shown in Fig. 6. In Figs. 6(a) and 6(b) we show the binding energies and representative potentials with wave functions, respectively, for all angular-momentum coupling cases that arise from Eq. (1). We note that for  $^{87}\text{Rb}(nD_j + 5S_{1/2}, F = 1, 2)$  molecules the hyperfine quantum numbers  $F$  are well defined because the hyperfine coupling is much larger than the molecular binding. As seen in Figs. 6(a) and 6(b), the delineation between Hund's cases (a) and (c) is shifted to lower  $n$  for the shallow potentials (which are due to hyperfine-induced mixing of singlet and triplet states at the  $5S_{1/2}$  atom). Essentially, the generally weaker scattering interaction

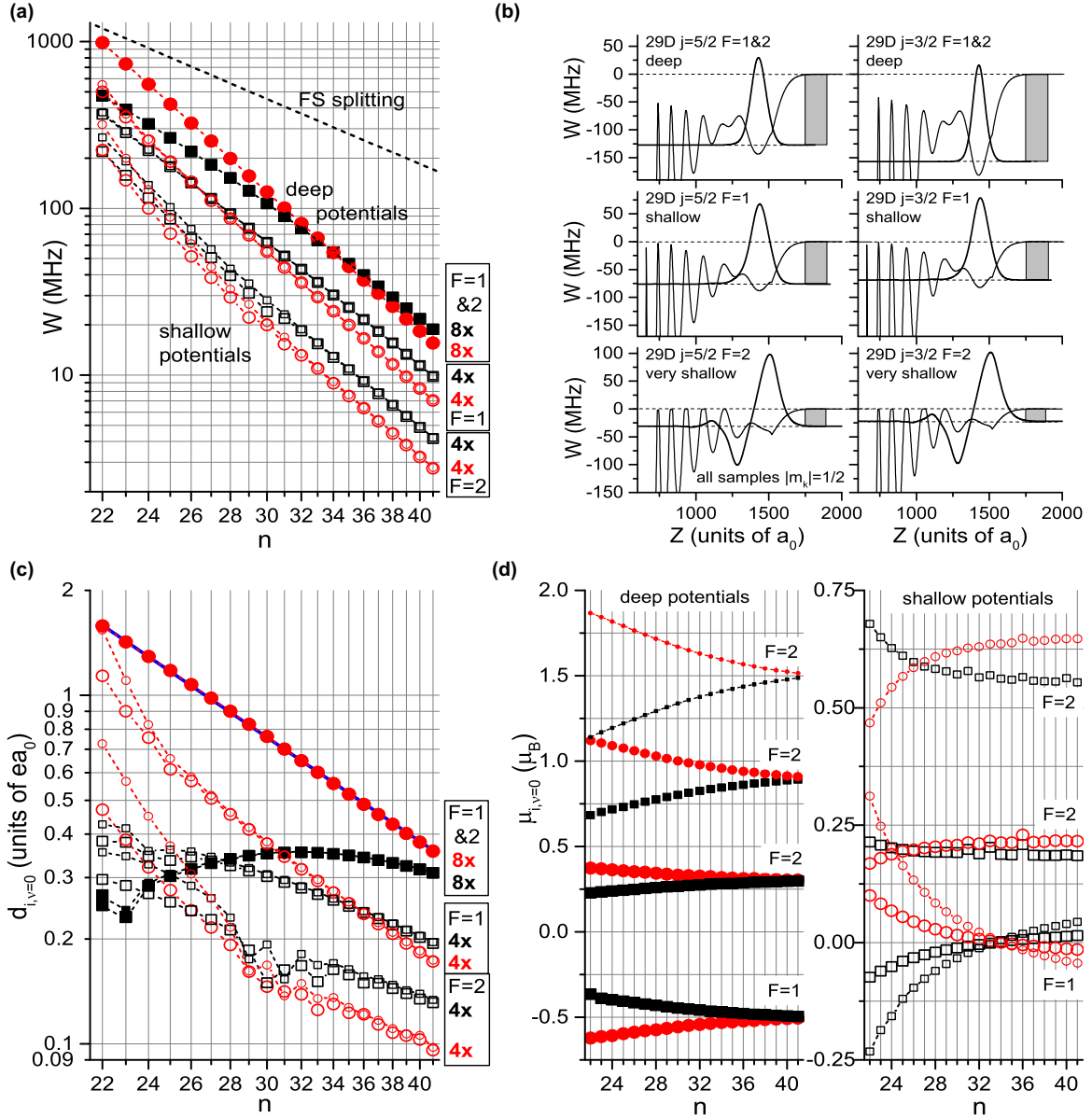


FIG. 6. (Color online) (a) Binding energies for  $v = 0$  in the outermost potential wells vs  $n$ , with all terms in Eq. (1) included. Symbol legend: Solid: deep, triplet potentials. These are identical for  $F = 1$  and  $F = 2$ . Hollow: shallow, mixed singlet-triplet potentials. These are different for  $F = 1$  and  $F = 2$ . Black squares:  $j = 5/2$ . Red circles:  $j = 3/2$ . Large size:  $|m_k| = 1/2$ . Medium size:  $|m_k| = 3/2$ . Small size:  $|m_k| = 5/2$ . The  $nD_j$  fine-structure splitting is plotted for reference. Numbers indicate degeneracies summed over all  $m_k$ . (b) Representative adiabatic potentials and wave functions for  $^{87}\text{Rb}(29D_j + 5S_{1/2}, F = 1, 2)(v = 0)$ , for  $j = 5/2$  (left column) and  $j = 3/2$  (right column). The pure triplet potentials are the same for  $F = 1$  and  $F = 2$  (top row), while the mixed singlet-triplet potentials are generally shallow and different for  $F = 1$  (middle row) and  $F = 2$  (bottom row). The gray bars on the right indicate binding energy, to visualize that the deep potentials are closer to Hund's case (a) ( $j = 3/2$  potential deeper than  $j = 5/2$  potential) than the shallow ones ( $j = 5/2$  potentials deeper than  $j = 3/2$  potentials). (c) Electric dipole moments  $d_{i,v}$  for  $v = 0$  in the outermost potential wells vs  $n$ , with all terms in Eq. (1) included. Symbol legend as in (a). The blue line through the data for the deep  $j = 3/2$  potentials is an allometric fit with exponent  $-2.4$ . (d) Magnetic dipole moments  $\mu_{i,v}$  for  $v = 0$  in the outermost potential wells vs  $n$ , with all terms in Eq. (1) included. Symbol legend as in (a). We only show data for positive  $m_k$  (results for negative  $m_k$  are the same with flipped sign). There are no degeneracies in  $\mu_{i,v=0}$ .

associated with the mixed singlet-triplet cases pushes those molecules more towards Hund's case (c).

The electric dipole moments of the deep molecular potentials are eightfold degenerate when summed over all  $m_k$ , and those of the shallow potentials are fourfold degenerate [see Fig. 6(c)]. It is noted that with decreasing  $n$  the degeneracies in energy and electric dipole moment become increasingly

lifted. This may be attributed to a stronger configuration mixing at low  $n$  caused by the relative increase of the  $e^- + \text{perturber}$  scattering term in Eq. (1). The only case in which the dipole moments of the  $^{87}\text{Rb}(nD_j + 5S_{1/2}, F = 1, 2)$  molecules exhibit a clear scaling behavior in  $n$  is for the  $j = 3/2$  deep potentials (which are the same for  $F = 1$  and  $F = 2$ ). A fit to the topmost data set in Fig. 6(c) gives an  $n^{-2.4}$  scaling,

similar to a result found previously for  $^{87}\text{Rb}_2$   $S$ -type Rydberg molecules [7]. Here, the scattering-induced mixing between the atomic Rydberg levels gives rise to a significant change in the electric dipole moments as a function of  $n$ . In the range  $n \gtrsim 30$ , the electric dipole moments for both types of shallow potentials of  $^{87}\text{Rb}(nD_{3/2} + 5S_{1/2}, F = 1, 2)$  also approximately scale as  $n^{-2.4}$ . The electric dipole moments for the upper fine-structure component  $j = 5/2$  have less clear scaling trends [squares in Fig. 6(c)]. In particular, the electric dipole moments for the deep  $^{87}\text{Rb}(nD_{5/2} + 5S_{1/2}, F = 1, 2)$  potentials do not exhibit a clear scaling behavior. This is likely a result of the transition from Hund's case (a) to Hund's case (c).

The magnetic moments for the molecular states are shown in Fig. 6(d). The magnetic moments are nondegenerate due to the different  $g$  factors of the involved types of spins. The  $n$  dependence again reflects the transition in angular-momentum coupling behavior between the two Hund's cases (a) and (c). We expect that experiments in weak electric and magnetic fields can reveal the electric and magnetic dipole moments of the vibrational states. The dipole moments computed in this work are for the weak-field limit, i.e., results are expected to be accurate as long as molecular Zeeman and Stark shifts are smaller than other relevant energy scales (such as the energy splitting between adjacent vibrational states).

## VII. HYPERFINE-STRUCTURE EFFECTS IN DEEP $^3S$ - AND $^3P$ -DOMINATED POTENTIALS

The trilobite molecules [12] generated by the  $^3S$  interaction are long range and on the order of 10 GHz deep, which is comparable to the hyperfine interaction of the  $5S_{1/2}$  perturber. It is therefore of interest to explore hyperfine effects on the trilobite adiabatic potentials. In Figs. 7(a) and 7(b) we show these potentials without and with hyperfine coupling for  $n = 30$ , for all relevant values of  $m_{j1} + m_{s2}$  and  $m_k = m_{j1} + m_{s2} + m_{i2}$ , respectively. While the hyperfine interaction does not affect the general shape and depth of the trilobite potentials, with hyperfine structure included there are three instead of only one. Since the number of  $^3P$  potential curves also triples, the crossing pattern between  $^3S$  and  $^3P$  potentials becomes considerably more complex, as seen in Fig. 7. Considering that the modulations near the bottom of the trilobite potentials are several 100 MHz deep, which is sufficient to support individual bound vibrational states, the hyperfine structure is expected to have profound effects on the detailed vibrational level structure of these molecules. In Fig. 7(b), one may expect to find long-lived  $^3S$ -dominated states in the gray regions. Further, as indicated by the circles in Fig. 7(b), the crossing locations and the detailed coupling behavior of  $\ell = 3$  Rydberg levels (which are optically accessible from low-lying atomic states) to molecular states in the long-range potentials also strongly depend on the hyperfine structure of the system under investigation.

In the present work we have not included the dependence of the  $^3P$   $e^- + \text{Rb}(5S_{1/2})$  scattering phase shift on  $J$  (where  $J = 0, 1, 2$ ) [17]. We have performed a preliminary calculation that indicates that the outermost several wells of the adiabatic potentials, which support the metastable molecular states, are not substantially altered by using  $J$ -dependent  $^3P$  scattering

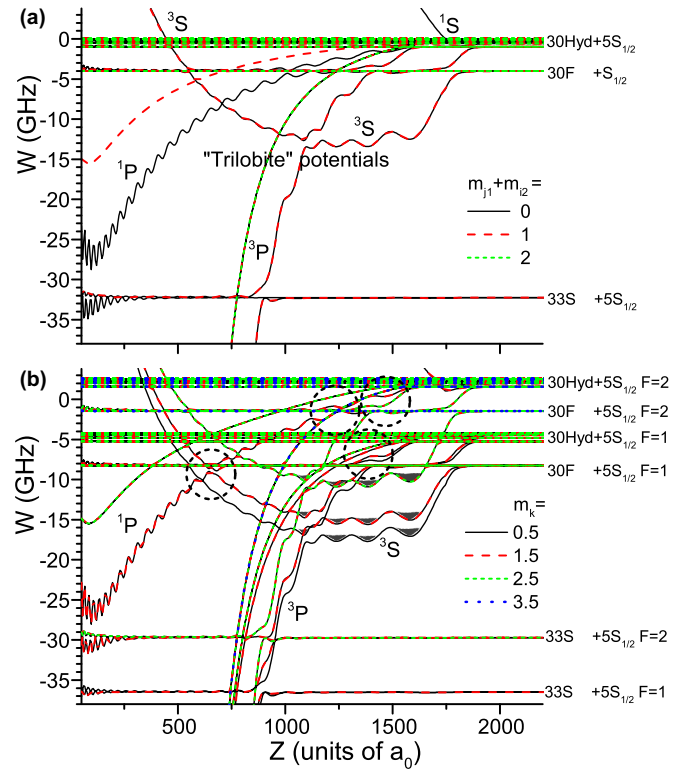


FIG. 7. (Color online) High- $\ell$  adiabatic potentials near  $n = 30$  of  $^{87}\text{Rb}_2$  (Rydberg +  $5S_{1/2}$ ) molecules (a) without and (b) with hyperfine structure included. The plots indicate the trilobite potentials [12], the dominant types of scattering interactions leading to deep potentials, the asymptotic states of the potentials, the regions where bound trilobite molecules may be found (gray areas), and the intersections between trilobite potentials and  $F$  ( $\ell = 3$ ) lines (dashed circles).

phase shifts. We also find that the crossings between the  $^3P$  potentials and the  $^3S$  trilobite potentials shift in position by amounts up to about  $50 a_0$ .

## VIII. CONCLUSION

In summary, we have systematically explored the role of fine-structure and hyperfine-structure couplings in  $^{87}\text{Rb}_2$  molecules formed between a Rydberg and  $5S_{1/2}$  ground-state atom. As has been done extensively in previous work, we have treated the  $e^- + 5S_{1/2}$  scattering with a Fermi model that includes  $S$ -wave and  $P$ -wave singlet and triplet scattering. The fine structure mostly influences the behavior of low- $\ell$  Rydberg molecules. We have explored in detail how  $^{87}\text{Rb}(nD + 5S_{1/2})$  molecules realize Hund's cases (a) and (c). The hyperfine structure originates in the perturber atom and therefore has consequences for all types (low- $\ell$  and high- $\ell$ ) of Rydberg molecules. In the case of  $^{87}\text{Rb}(nD + 5S_{1/2})$  molecules, mixing of singlet and triplet potentials results in a set of shallow adiabatic potentials, whose quasibound states should be experimentally observable (in addition to those in the hyperfine-independent pure triplet potentials). We have obtained electric and magnetic dipole moments, which could, in future work, be measured spectroscopically in weak electric



and magnetic fields. The hyperfine structure has also been seen to alter the deep,  $^3S$ -scattering-induced trilobite potentials as well as their crossing behavior with  $\ell = 3$  Rydberg states; experimental spectroscopic studies should reveal these details. Since molecular level energies and properties are very sensitive to the scattering phase shifts used in the Fermi model, we expect that spectroscopy of Rydberg molecules can serve as a sensitive tool to provide measurement-based input to future theoretical studies in low-energy electron scattering.

The effects of the  $J$  dependence of the  $^3P$  scattering phase shifts could also be addressed in future work.

### ACKNOWLEDGMENTS

We thank I. I. Fabrikant for providing scattering phase shifts used in our calculations. This work was supported by the AFOSR (Grant No. FA9550-10-1-0453) and the NSF (Grant No. PHY-1205559).

- 
- [1] V. Bendkowsky, B. Butscher, J. Nipper, J. P. Shaffer, R. Löw, and T. Pfau, *Nature (London)* **458**, 1005 (2009).
  - [2] J. Tallant, S. T. Rittenhouse, D. Booth, H. R. Sadeghpour, and J. P. Shaffer, *Phys. Rev. Lett.* **109**, 173202 (2012).
  - [3] M. A. Bellos, R. Carollo, J. Banerjee, E. E. Eyler, P. L. Gould, and W. C. Stwalley, *Phys. Rev. Lett.* **111**, 053001 (2013).
  - [4] D. A. Anderson, S. A. Miller, and G. Raithel, *Phys. Rev. Lett.* **112**, 163201 (2014).
  - [5] A. T. Krupp, A. Gaj, J. B. Balewski, P. Ilzhöfer, S. Hofferberth, R. Löw, T. Pfau, M. Kurz, and P. Schmelcher, *Phys. Rev. Lett.* **112**, 143008 (2014).
  - [6] B. Butscher, J. Nipper, J. B. Balewski, L. Kukota, V. Bendkowsky, R. Löw, and T. Pfau, *Nature Phys.* **6**, 970 (2010).
  - [7] W. Li, T. Pohl, J. M. Rost, S. T. Rittenhouse, H. R. Sadeghpour, J. Nipper, B. Butscher, J. B. Balewski, V. Bendkowsky, R. Löw, and T. Pfau, *Science* **334**, 1110 (2011).
  - [8] V. Bendkowsky, B. Butscher, J. Nipper, J. B. Balewski, J. P. Shaffer, R. Löw, T. Pfau, W. Li, J. Stanojevic, T. Pohl, and J. M. Rost, *Phys. Rev. Lett.* **105**, 163201 (2010).
  - [9] A. Gaj, A. T. Krupp, J. B. Balewski, R. Löw, S. Hofferberth, and T. Pfau, *Nature Comm.* **5**, 4546 (2014).
  - [10] E. Fermi, *Il Nuovo Cimento* **11**, 157 (1934).
  - [11] A. Omont, *J. Phys. (France)* **38**, 1343 (1977).
  - [12] C. H. Greene, A. S. Dickinson, and H. R. Sadeghpour, *Phys. Rev. Lett.* **85**, 2458 (2000).
  - [13] I. I. Fabrikant, *J. Phys. B* **19**, 1527 (1986).
  - [14] C. Bahrim and U. Thumm, *Phys. Rev. A* **61**, 022722 (2000).
  - [15] C. Bahrim, U. Thumm, and I. I. Fabrikant, *J. Phys. B* **34**, L195 (2001).
  - [16] E. L. Hamilton, C. H. Greene, and H. R. Sadeghpour, *J. Phys. B* **35**, L199 (2002).
  - [17] A. A. Khuskivadze, M. I. Chibisov, and I. I. Fabrikant, *Phys. Rev. A* **66**, 042709 (2002).
  - [18] M. I. Chibisov, A. A. Khuskivadze, and I. I. Fabrikant, *J. Phys. B* **35**, L193 (2002).
  - [19] D. Meschede, *J. Opt. Soc. Am. B* **4**, 413 (1987).
  - [20] A. Tauschinsky, R. Newell, H. B. van Linden van den Heuvell, and R. J. C. Spreeuw, *Phys. Rev. A* **87**, 042522 (2013).
  - [21] H. Sassmannshausen, F. Merkt, and J. Deiglmayr, *Phys. Rev. A* **87**, 032519 (2013).
  - [22] T. F. Gallagher, *Rydberg Atoms* (Cambridge University Press, New York, 1994), p. 349.
  - [23] U. Litzén, *Phys. Scr.* **1**, 253 (1970).
  - [24] H. R. Sadeghpour and S. T. Rittenhouse, *Mol. Phys.* **111**, 1902 (2013).
  - [25] J. J. Sakurai, *Modern Quantum Mechanics Revised Edition* (Addison-Wesley, Boston, 1994).
  - [26] E. P. Wigner, *Phys. Rev.* **98**, 145 (1955).
  - [27] B. Butscher, V. Bendkowsky, J. Nipper, J. B. Balewski, L. Kukota, R. Löw, T. Pfau, W. Li, T. Pohl, and J. M. Rost, *J. Phys. B* **44**, 184004 (2011).
  - [28] A. Junginger, J. Main, and G. Wunner, *J. Phys. B* **46**, 085201 (2013).
  - [29] J. M. Brown and A. Carrington, *Rotational Spectroscopy of Diatomic Molecules* (Cambridge University Press, Cambridge, 2003).

## Photoassociation of Long-Range $nD$ Rydberg Molecules

D. A. Anderson,<sup>\*</sup> S. A. Miller, and G. Raithel

*Department of Physics, University of Michigan, Ann Arbor, Michigan 48109, USA*

(Received 6 January 2014; published 23 April 2014)

We observe long-range homonuclear diatomic  $nD$  Rydberg molecules photoassociated out of an ultracold gas of  $^{87}\text{Rb}$  atoms for  $34 \leq n \leq 40$ . The measured ground-state binding energies of  $^{87}\text{Rb}(nD + 5S_{1/2})$  molecular states are larger than those of their  $^{87}\text{Rb}(nS + 5S_{1/2})$  counterparts, which shows the dependence of the molecular bond on the angular momentum of the Rydberg atom. We exhibit the transition of  $^{87}\text{Rb}(nD + 5S_{1/2})$  molecules from a molecular-binding-dominant regime at low  $n$  to a fine-structure-dominant regime at high  $n$  [akin to Hund's cases (a) and (c), respectively]. In the analysis, the fine structure of the  $nD$  Rydberg atom and the hyperfine structure of the  $5S_{1/2}$  atom are included.

DOI: 10.1103/PhysRevLett.112.163201

PACS numbers: 34.50.Cx, 31.10.+z, 33.80.Rv, 34.20.Cf

Cold atomic systems have opened new frontiers at the interface of atomic and molecular physics. Of particular interest are a recently discovered class of long-range, homonuclear Rydberg molecules [1,2]. Formed via an attractive interaction between a Rydberg electron and a ground-state atom [1], these molecules are among the largest ever observed with internuclear separations of several thousand Bohr radii. Their distinctive binding mechanism, which is unlike conventional covalent, ionic, and van der Waals bonds between ground-state atoms, results in loosely bound molecules whose properties mimic those of their constituent Rydberg atoms. The discovery of these molecular bonds has been likened to a new ultracold chemistry [3] and has spurred a significant amount of theoretical [4,5] and experimental interest [6–9]. Nondegenerate, low angular momentum Rydberg states (orbital angular momentum  $\ell \leq 2$  in rubidium) produce molecules with  $\sim \text{MHz}$  binding energies and permanent electric dipole moments of a few Debye. The  $\ell = 0$  molecules were first observed by photoassociation [10] of cold  $^{87}\text{Rb}$  atoms [2]. Recently, molecular states with  $\ell = 1$  and high electron energies have also been excited via bound-bound transitions in  $^{85}\text{Rb}_2$  [9]. For high- $\ell$  Rydberg states, so-called trilobite molecules with giant permanent electric dipole moments of several kilo-Debye and  $\sim \text{GHz}$  binding energies are predicted to exist [1]. These have yet to be observed, though dipolar molecules have been prepared in Rb [7] and Cs [8].

The relevant interaction was first described by Fermi [11] to help explain pressure-induced energy shifts of Rydberg absorption lines in a gas [12]. The de Broglie wavelength of the Rydberg electron (position  $\mathbf{r}$ ) is much larger than that of a heavy ground-state atom (position  $\mathbf{R}$ ) that lies within the Rydberg atom's volume, and their interaction can be approximated as a low-energy  $s$ -wave scattering process (scattering length  $a_s$ ). The interaction is described with a Fermi-type pseudopotential [1,13]  $V_{\text{pseudo}}(\mathbf{r}) = 2\pi a_s \delta^3(\mathbf{r} - \mathbf{R})$ , where  $p$ -wave and higher-order

scattering [4] are neglected. For negative  $a_s$ , the interaction can lead to bound molecular states [1,13].

The bond strengths and electric and magnetic moments of Rydberg molecules are strongly dependent on the angular-momentum couplings in the Rydberg and ground-state atom constituents. In the present work, we focus on long-range  $^{87}\text{Rb}_2$  molecules formed by an  $nD$  Rydberg and a  $5S_{1/2}$  ground-state atom. Within the low- $\ell$  class of these molecules, the  $nD$  ones have the highest binding energies, which generally increase with  $\ell$  due to the  $\sqrt{2\ell+1}$  scaling of the angular wave functions  $Y_{\ell}^{m=0}(\theta=0)$ . The angular-momentum coupling spans three Hund's cases as  $\ell$  varies from 0 to 2. The  $nS_{1/2} + 5S_{1/2}$  molecules are akin to Hund's case (b), because they have  $L = 0$  and total electron spin  $S = 1$ . The  $nP_j + 5S_{1/2}$  molecules are akin to Hund's case (c), because the fine structure coupling is larger than the scattering interaction energy. The  $nD_j + 5S_{1/2}$  molecules present a unique system, because they transition from Hund's case (c) at large  $n$  to Hund's case (a) at  $n \lesssim 30$ , where the scattering interaction energy becomes increasingly greater than the fine structure coupling. The  $F$  and higher- $\ell$  states of Rb intersect with a sole, deeply bound (trilobite) potential which accumulates most of the level shifts [1], negating the existence of potential wells similar to those below the  $S$ ,  $P$ , and  $D$  asymptotes. In our model, we include the fine structure of the Rydberg atom and the hyperfine structure of the  $5S_{1/2}$  perturber atom, both of which have observable effects.

To excite  $nD$  Rydberg molecules, we first prepare a sample of  $\sim 10^5$  magnetically trapped  $^{87}\text{Rb}$  atoms in their  $|F = 2, m_F = 2\rangle$  ground state at a temperature  $\leq 17 \mu\text{K}$  and peak density  $\gtrsim 5 \times 10^{11} \text{ cm}^{-3}$ . Optical excitation to  $nD$  Rydberg states is accomplished via a two-photon transition from the  $5S_{1/2}$  ground state by using 780- and 480-nm laser beams. The 780-nm laser frequency is fixed  $\sim 1 \text{ GHz}$  off resonance from the  $5S_{1/2}$  to  $5P_{3/2}$  transition, and the 480-nm laser frequency is scanned to excite either Rydberg atoms or

molecules. The combined excitation bandwidth is  $\approx 2$  MHz. The 780-nm laser has a power of  $\sim 500$   $\mu$ W and is collimated to a full width at half maximum (FWHM) of 3.5 mm. The 480-nm beam has a power of  $\sim 35$  mW and is focused to a FWHM of  $89 \pm 5$   $\mu$ m into the cigar-shaped atom sample, which has a FWHM diameter of 28  $\mu$ m and an aspect ratio of  $\approx 1:3$ .

The atom sample is enclosed by six individually addressable electrodes used to control the electric field at the excitation location, described in previous work [14]. We zero the electric field to within  $\lesssim 200$  mV/cm by Stark spectroscopy on  $59D$  Rydberg states [15]. This ensures that quadratic Stark shifts of the  $nD$  Rydberg levels in the  $n$  range of interest are  $\lesssim 2$  MHz. In a single experiment, the atom sample is illuminated by  $2 - 3$   $\mu$ s long laser pulses followed by electric-field ionization of Rydberg atoms and molecules [16]. The signal ions are extracted and detected by a microchannel plate located 10 cm away. We use one ground-state atom sample for a series of 55 individual experiments at a single 480-nm frequency step; density loss during one series is negligible.

The photoassociation of a Rydberg atom and ground-state atom pair into a bound molecular state occurs when the excitation laser is detuned from the atomic Rydberg line by an amount equal to the molecular binding energy. In Fig. 1, we show an experimental spectrum in the vicinity of the atomic  $35D_{5/2}$  Rydberg line. A prominent satellite line emerges at  $-38 \pm 3$  MHz, which is assigned to the  $(35D_{5/2} + 5S_{1/2})(\nu = 0)$  molecule, where  $\nu = 0$  denotes the vibrational ground state. This binding energy is  $\approx 1.6$  times larger than that of the  $(35S_{1/2} + 5S_{1/2})(\nu = 0)$  molecular state measured in previous experiments [2,6].

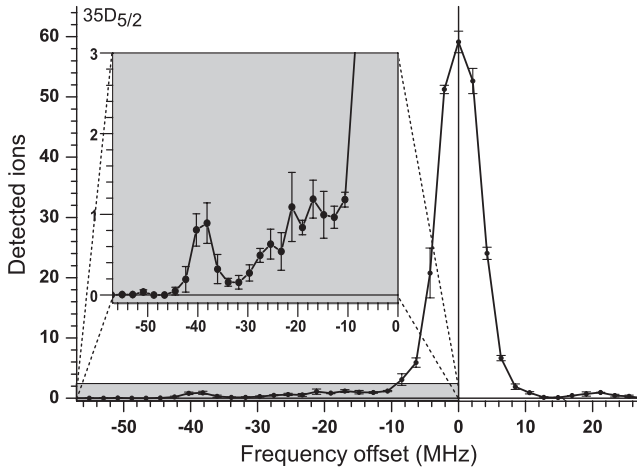


FIG. 1. Spectrum centered on the  $35D_{5/2}$  atomic Rydberg line showing the  $^{87}\text{Rb}(35D_{5/2} + 5S_{1/2})(\nu = 0)$  molecular line at  $-38 \pm 3$  MHz. The vertical error bars are the standard error of three sets of 55 individual experiments at each frequency step. The error in the binding energy is equal to the average long-term frequency drift observed over one full scan.

The larger binding energy reflects the deepening of the molecular potential with  $\ell$ .

A series of  $nD_{5/2}$  Rydberg spectra for  $34 \leq n \leq 42$  is shown in Fig. 2(a) (right). The lowermost, redshifted lines for  $n = 40$  and below are assigned to the molecular states. Molecular lines are not discernable in the  $n = 42$  and 41 spectra, because the line broadening due to residual fields and the laser linewidth exceeds the molecular binding energies for these states. Additional satellite lines are expected but are likely obscured in Figs. 1 and 2(a) by the broadening of the atomic lines as well as artificial signals at  $\pm 20$  MHz due to weak, symmetric side peaks in the 480-nm laser spectrum (caused by a Pound-Drever-Hall stabilization loop). Features near  $-20$  MHz are assigned to molecular lines only if they are significantly stronger than the artificial signal at  $+20$  MHz.

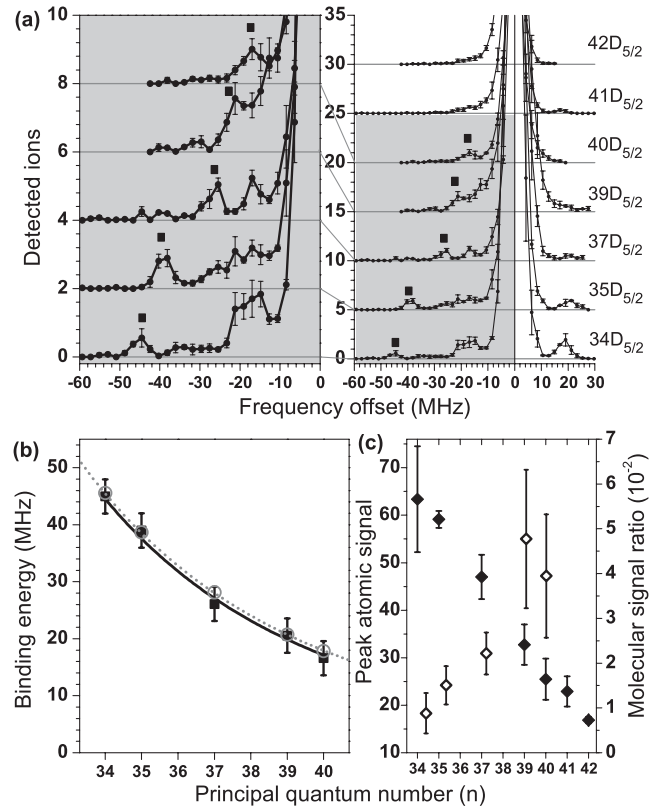


FIG. 2. (a) Right: Spectra centered on  $nD_{5/2}$  atomic Rydberg lines for the indicated values of  $n$  and identified molecular lines (squares). Left: Selected spectra from the plot on the right for states with identified molecular lines. Error bars are obtained as in Fig. 1. (b) Binding energies obtained from Gaussian fits to the molecular lines identified in (a) vs  $n$ . An allometric fit (solid curve) to the experimental binding energies yields a  $n^{-5.9 \pm 0.4}$  scaling. Also shown are theoretical binding energies for the  $^{87}\text{Rb}(nD_{5/2} + 5S_{1/2})(\nu = 0)$  molecular states with  $a_{s0} = -14a_0$  (hollow circles and dotted curve). (c) Peak number of detected ions on the  $nD_{5/2}$  atomic Rydberg line (solid diamonds, left axis) and ratio of molecular and atomic line strengths (hollow diamonds, right axis) vs  $n$ .

Figure 2(b) shows the molecular binding energies measured in Fig. 2(a) vs  $n$ . One may expect the binding energies to be proportional to the probability density of the Rydberg electron wave function, which scales as  $\sim n^{-6}$ . An allometric fit to the data in Fig. 2(b) qualitatively supports this expectation over the displayed range of  $n$ .

As shown in Fig. 2(c), the ratio of molecular and atomic line strengths ranges from  $\approx 1\% - 5\%$ . By taking our peak atomic density into consideration, this agrees quite well with the relative signal strengths found in Refs. [2,6]. One may expect the molecular-signal ratio to scale with the probability of finding a  $5S_{1/2}$  atom within the Rydberg-atom volume (which scales as  $n^6$ ), corresponding to an increase of about a factor of 2.5 over the  $n$  range in Fig. 2(c). The observed increase is about a factor of 5. This enhancement is likely due to a Rydberg excitation blockade caused by electrostatic Rydberg-atom interactions [17,18], which suppresses the atomic line [19]. Since the blockade's effectiveness increases with  $n$ , the molecular-signal ratio scales faster than  $n^6$ . This interpretation is corroborated by the atomic-signal strength, which drops by a factor of 4 over the  $n$  range in Fig. 2(c). In the absence of an excitation blockade, the atomic signal would drop as  $n^{-3}$ , i.e., by only a factor of 2 in Fig. 2(c).

Molecular states of the  $nD_j + 5S_{1/2}$  type exhibit a transition between Hund's case (a) at low  $n$  and Hund's case (c) at high  $n$ . Most of our data trend towards Hund's case (c), where the dominant molecular potentials carry spin-dependent factors  $|\langle m_\ell = 0, m_s = \pm 1/2 | j, m_j = \pm 1/2 \rangle|^2$  (detailed model below); these factors are  $\ell/(2\ell + 1)$  for  $j = \ell - 1/2$  and  $(\ell + 1)/(2\ell + 1)$  for  $j = \ell + 1/2$ . Hence, in Hund's case (c) (high  $n$ ) the  $\nu = 0$  binding-energy ratio for  $nD_j + 5S_{1/2}$   $j = 3/2$  and  $5/2$  molecules should be about  $2/3$ . For decreasing  $n$ , the fine structure splitting increases as  $n^{-3}$ , while the molecular binding energy increases as  $n^{-6}$ . The system then trends towards Hund's case (a), in which the  $\nu = 0$  binding energy ratio changes from  $2/3$  to  $\gg 1$  (see below). Therefore, the  $\nu = 0$  binding energy ratio is a convenient experimental measure to characterize the system. Figure 3 shows spectra of the two fine structure components of  $37D$ . Molecular peaks are present for both  $j = 3/2$  and  $5/2$ , with binding energies of  $24 \pm 3$  and  $26 \pm 3$  MHz, respectively, corresponding to a ratio of  $0.92 \pm 0.15$ . Since this is significantly larger than  $2/3$ , for  $n = 37$  the system is in the transition regime between Hund's cases (c) and (a).

Next we compare experimental data with a calculation. We consider  $s$ -wave triplet scattering and omit singlet scattering [1]. For low electron momenta  $k$ , the  $s$ -wave triplet scattering length is  $a_s^T(k) \approx a_{s0} + \frac{\pi}{3}\alpha k$ , where  $a_{s0} = a_s^T(k = 0)$  is the zero-energy scattering length and  $\alpha$  the Rb  $5S_{1/2}$  polarizability [13]. We fit  $a_{s0}$  to match the experimental data. In calculations not presented here we

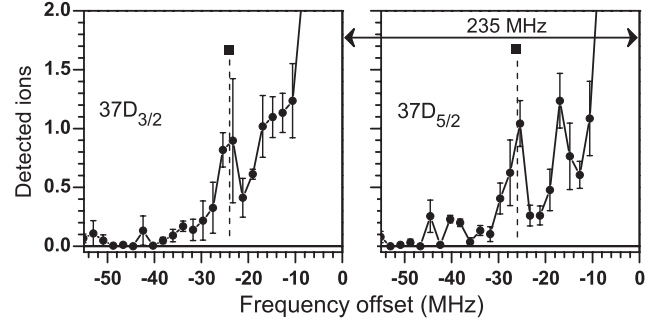


FIG. 3. Spectra centered on the  $37D_j$  atomic Rydberg lines for  $j = 3/2$  (left) and  $j = 5/2$  (right; the same as in Fig. 2).  $^{87}\text{Rb}(37D_j + 5S_{1/2})(\nu = 0)$  molecular signals are indicated by vertical dashed lines and squares.

have verified that  $p$ -wave scattering strongly influences the inner part of the molecular potentials [20] but leaves the outermost well, where the bound states relevant to our work are found, largely unaffected. The Rydberg atom's fine structure and the perturber's hyperfine structure are included, because they are on the same order or larger than the molecular binding. The much smaller hyperfine structure of the Rydberg atom is ignored. We include configuration mixing with neighboring Rydberg manifolds [5]. For the  $5S_{1/2}$  atom located at  $\mathbf{R} = Z\mathbf{e}_z$ , the Hamiltonian is

$$\hat{H}_0 + 2\pi a_s^T[k(r)]\delta^3(\hat{\mathbf{r}} - Z\mathbf{e}_z) \left( \hat{\mathbf{S}}_1 \cdot \hat{\mathbf{S}}_2 + \frac{3}{4} \right) + A\hat{\mathbf{S}}_2 \cdot \hat{\mathbf{I}}_2, \quad (1)$$

where the unperturbed Hamiltonian  $\hat{H}_0$  includes Rydberg quantum defects and fine structure [16]. The operators  $\hat{\mathbf{S}}_1$  and  $\hat{\mathbf{S}}_2$  are the spins of the Rydberg electron and  $5S_{1/2}$  atom, respectively. The  $^{87}\text{Rb}$   $5S_{1/2}$  atom has  $\ell_2 = 0$ , a nuclear spin  $\hat{\mathbf{I}}_2$  with  $I_2 = 3/2$ , and a hyperfine parameter  $A = h \times 3.4$  GHz (in SI units). The projector  $\hat{\mathbf{S}}_1 \cdot \hat{\mathbf{S}}_2 + \frac{3}{4}$  has the eigenvalue one (zero) for the triplet (singlet) states of  $\hat{\mathbf{S}}_1$  and  $\hat{\mathbf{S}}_2$ , enabling only triplet scattering. In the classically allowed range of the Rydberg electron  $k = \sqrt{-1/(n_{\text{eff},1}n_{\text{eff},2}) + 2/r}$  (atomic units), and  $k = 0$  elsewhere. There,  $n_{\text{eff},1}$  and  $n_{\text{eff},2}$  are the effective quantum numbers of the Rydberg states coupled by the scattering term. Since only states with  $m_{\ell 1} = 0$  are nonvanishing on the internuclear axis, the relevant Hilbert space is limited to  $\{|n, \ell_1, j_1, m_{j1} = \pm 1/2, m_{s2} = \pm 1/2, m_{i2} = \pm 1/2, \pm 3/2\rangle\}$ . Since the Hamiltonian in Eq. (1) conserves  $m_k := m_{j1} + m_{s2} + m_{i2}$ , the space breaks up into separated subspaces with  $m_k = \pm 5/2, \pm 3/2, \pm 1/2$ , where the scattering term couples states with the same  $m_{j1} + m_{s2}$ , while the hyperfine term couples states with the same  $m_{s2} + m_{i2}$ .

The Hamiltonian in Eq. (1) is diagonalized, resulting in adiabatic potential surfaces  $V_{ad,i}(Z)$  and electric  $[d_i(Z)]$  and magnetic  $[\mu_i(Z)]$  dipole moments of the adiabatic



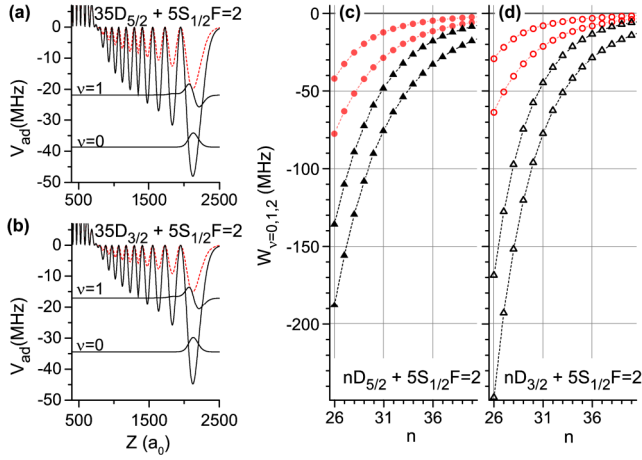


FIG. 4 (color online). (a),(b) Deep (solid lines) and shallow (dashed lines) potentials for  $35D_{5/2}$  and  $35D_{3/2}$ -type molecules, for  $a_{s0} = -14a_0$ , and vibrational wave functions for  $\nu = 0, 1$  in the deep potentials. (c),(d) Energy levels for  $\nu = 0, 1$  in the deep (triangles) and shallow (circles) potentials vs  $n$ .

states [ $i$  is an arbitrary label for the  $V_{ad}(Z)$ ]. The vibrational states  $W_{i,\nu}$  and their wave functions  $\Psi_{i,\nu}(Z)$  are found by solving the Schrödinger equation with potential  $V_{ad,i}(Z)$  and reduced mass  $87 \text{ amu}/2$ , and their electric and magnetic dipole moments are  $d_{i,\nu} = \int |\Psi_{i,\nu}(Z)|^2 d_i(Z) dZ$  and  $\mu_{i,\nu} = \int |\Psi_{i,\nu}(Z)|^2 \mu_i(Z) dZ$ , respectively.

In Figs. 4(a) and 4(b), we show all potentials  $V_{ad}(Z)$  for  $35D_{5/2}$  and  $35D_{3/2}$  that connect to the  $F = 2$  hyperfine level of the  $5S_{1/2}$  atom, as well as the vibrational states  $\nu = 0, 1$  of the deeper potentials. The deep and shallow potentials and their states have degeneracies of 6 and 4, respectively. The shallow potentials are due to hyperfine-induced mixing between the electronic singlet and a triplet state. In Figs. 4(c) and 4(d), we show the vibrational energies  $W_{i,\nu}$  for  $\nu = 0, 1$  over a range of  $n$  for  $nD_{5/2} + 5S_{1/2}$  and  $nD_{3/2} + 5S_{1/2}$  molecules.

In the experiment, we excite molecules below the  $F = 2$  asymptote, for which the states in the deep potential  $V_{ad}(Z)$  have the larger degeneracy and are easier to observe due to their larger binding energies. Hence, we adjust  $a_{s0}$  so that the  $\nu = 0$  levels in the deep  $V_{ad}(Z)$  match the experimental data in Figs. 1–3 and find  $a_{s0} = -14a_0 \pm 0.5a_0$  [see Fig. 2(b)]. (For  $37D_{5/2}$  the  $\nu = 0$  binding energy increases by about 4 MHz when changing  $a_{s0}$  from  $-13.5$  to  $-14.5a_0$ .) This  $a_{s0}$  value lies within the range of published values  $-13$  to  $-19.48a_0$  [2,6,21–23]. The experimental signals at about half the  $\nu = 0$  binding energies, seen in some of the plots in Fig. 2(a), may correspond to levels at about half the  $\nu = 0$  binding energies in Figs. 4(c) and 4(d).

In the high- $n$  limit in Fig. 5(a), the  $\nu = 0$  binding-energy ratio for  $D_{3/2}$  and  $D_{5/2}$  approaches  $2/3$ , as expected for Hund's case (c), and both sets of binding energies approximately scale inversely with the atomic volume (i.e., as

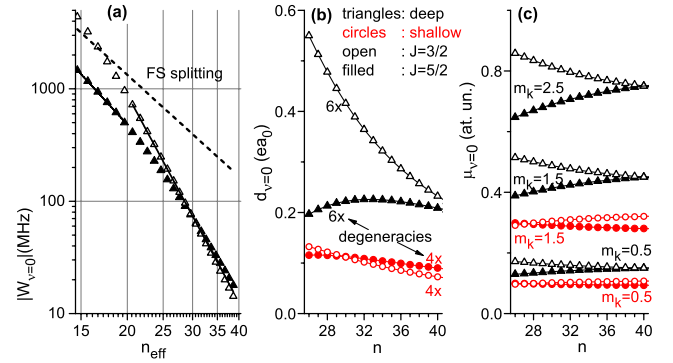


FIG. 5 (color online). (a)  $\nu = 0$  binding energies in the deep molecular potentials for  $nD_{5/2}$  (filled triangles),  $nD_{3/2}$  (open triangles), and the  $D$  fine structure splitting (dashed line) vs the effective quantum number. Solid lines are fits. The  $D_{3/2}$  energies are fit well by  $84.2 \text{ GHz}/n_{\text{eff}}^{6.13}$ . The  $D_{5/2}$  energies do not exhibit a global scaling; at low  $n$  they tend to scale as  $23 \text{ MHz}/n_{\text{eff}}^{3.6}$ . (b) Electric dipole moments for  $\nu = 0$  vs  $n$  for the deep (triangles) and shallow (circles)  $V_{ad}(Z)$  for  $j = 3/2$  (open) and  $j = 5/2$  (filled). (c) Magnetic dipole moments for the same states as in (b).

$n_{\text{eff}}^{-6}$ ). At low  $n$ , the system transitions into Hund's case (a), where the binding-energy ratio changes from  $2/3$  to  $\gg 1$ . Also, the  $\nu = 0$  binding energies for the lower ( $D_{3/2}$ ) fine structure level exceed the fine structure coupling and keep scaling as  $n_{\text{eff}}^{-6}$ , while those for the  $D_{5/2}$  level approach the fine structure splitting and its scaling ( $n_{\text{eff}}^{-3}$ ). The experimental data in Fig. 3 are in the transition regime between the two Hund's cases.

For  $nD$  Rydberg molecules the electric dipole moments  $d_{\nu=0}$  are somewhat smaller than for  $nS$  ones [see Fig. 5(b) and Ref. [7]]. As a result of the transition between two Hund's cases, the  $d_{\nu=0}$  of the  $nD_{5/2}$ -type molecules do not exhibit a clear scaling. Those for the  $nD_{3/2}$ -type molecules scale close to  $n_{\text{eff}}^{-2}$ , similar to  $S$ -type ones [7]. Noting that  $d_{\nu=0} \lesssim 0.25ea_0$  and that the stray electric field in our experiment is  $\lesssim 200 \text{ mV/cm}$ , the experimental permanent-electric-dipole shift is well below 1 MHz. The magnetic moments [Fig. 5(c)] exhibit a gradual change that reflects the change in angular-momentum coupling behavior between the two Hund's cases. In our  $< 1 \text{ G}$  magnetic field in the atom trap, the molecular lines could be broadened over a range  $\lesssim 4 \text{ MHz}$ , while the atomic lines have  $|m_j| \leq 5/2$  and could be broadened over a range  $\lesssim 8 \text{ MHz}$ . These estimates agree well with the linewidths seen in the spectra.

In summary, we have observed polar Rydberg molecules of the type  $nD_j + 5S_{1/2}$ . The binding energies are larger than those of previously observed  $nS_{1/2} + 5S_{1/2}$  molecules. The molecules undergo a transition between Hund's case (a) at low  $n$  to Hund's case (c) at high  $n$ . With improved spectroscopic resolution, one should be able to measure the electric dipole moments and to assign higher-lying vibrational levels in the deep potentials in Fig. 4 as well as levels in the shallow potentials. Recently, we became

aware of related work on  $nD$  molecular states in a higher-magnetic-field regime [24].

This work was supported by the AFOSR (FA9550-10-1-0453). We thank C.H. Greene, H.R. Sadeghpour, and S.T. Rittenhouse for helpful discussions.

---

\*anderda@umich.edu

- [1] C. H. Greene, A. S. Dickinson, and H. R. Sadeghpour, *Phys. Rev. Lett.* **85**, 2458 (2000).
- [2] V. Bendkowsky, B. Butscher, J. Nipper, J. P. Shaffer, R. Löw, and T. Pfau, *Nature (London)* **458**, 1005 (2009).
- [3] S. D. Hogan and F. Merkt, *ChemPhysChem* **10**, 2931 (2009).
- [4] A. A. Khuskivadze, M. I. Chibisov, and I. I. Fabrikant, *Phys. Rev. A* **66**, 042709 (2002).
- [5] H. R. Sadeghpour and S. T. Rittenhouse, *Mol. Phys.* **111**, 1902 (2013).
- [6] V. Bendkowsky, B. Butscher, J. Nipper, J. B. Balewski, J. P. Shaffer, R. Löw, T. Pfau, W. Li, J. Stanojevic, T. Pohl, and J. M. Rost, *Phys. Rev. Lett.* **105**, 163201 (2010).
- [7] W. Li, T. Pohl, J. M. Rost, S. T. Rittenhouse, H. R. Sadeghpour, J. Nipper, B. Butscher, J. B. Balewski, V. Bendkowsky, R. Löw, and T. Pfau, *Science* **334**, 1110 (2011).
- [8] J. Tallant, S. T. Rittenhouse, D. Booth, H. R. Sadeghpour, and J. P. Shaffer, *Phys. Rev. Lett.* **109**, 173202 (2012).
- [9] M. A. Bellos, R. Carollo, J. Banerjee, E. E. Eyler, P. L. Gould, and W. C. Stwalley, *Phys. Rev. Lett.* **111**, 053001 (2013).
- [10] K. M. Jones, E. Tiesinga, P. D. Lett, and P. S. Julienne, *Rev. Mod. Phys.* **78**, 483 (2006).
- [11] E. Fermi, *Nuovo Cimento* **11**, 157 (1934).
- [12] E. Amaldi and E. Segr, *Nuovo Cimento* **11**, 145 (1934).
- [13] A. Omont, *J. Phys. (Paris)* **38**, 1343 (1977).
- [14] D. A. Anderson, A. Schwarzkopf, R. E. Sapiro, and G. Raithel, *Phys. Rev. A* **88**, 031401 (2013).
- [15] J. Neukammer, H. Rinneberg, K. Vietzke, A. König, H. Hieronymus, M. Kohl, H. J. Grabka, and G. Wunner, *Phys. Rev. Lett.* **59**, 2947 (1987).
- [16] T. F. Gallagher, *Rydberg Atoms* (Cambridge University Press, Cambridge, England, 1994), pp. 220–221.
- [17] A. Reinhard, T. C. Liebisch, B. Knuffman, and G. Raithel, *Phys. Rev. A* **75**, 032712 (2007).
- [18] A. Schwarzkopf, R. E. Sapiro, and G. Raithel, *Phys. Rev. Lett.* **107**, 103001 (2011).
- [19] D. Tong, S. M. Farooqi, J. Stanojevic, S. Krishnan, Y. P. Zhang, R. Côté, E. E. Eyler, and P. L. Gould, *Phys. Rev. Lett.* **93**, 063001 (2004).
- [20] E. L. Hamilton, C. H. Greene, and H. R. Sadeghpour, *J. Phys. B* **35**, L199 (2002).
- [21] C. Bahrim and U. Thumm, *Phys. Rev. A* **61**, 022722 (2000).
- [22] C. Bahrim, U. Thumm, and I. I. Fabrikant, *J. Phys. B* **34**, L195 (2001).
- [23] I. I. Fabrikant, *J. Phys. B* **19**, 1527 (1986).
- [24] A. T. Krupp, A. Gaj, J. B. Balewski, P. Ilzhöfer, S. Hofferberth, R. Löw, T. Pfau, M. Kurz, and P. Schmelcher, *Phys. Rev. Lett.* **112**, 143008 (2014).

1.

**1. Report Type**

Final Report

**Primary Contact E-mail****Contact email if there is a problem with the report.**

graithe1@umich.edu

**Primary Contact Phone Number****Contact phone number if there is a problem with the report**

7346479031

**Organization / Institution name**

University of Michigan

**Grant/Contract Title****The full title of the funded effort.**

Interactions of ultracold impurity particles with Bose-Einstein Condensates

**Grant/Contract Number****AFOSR assigned control number. It must begin with "FA9550" or "F49620" or "FA2386".**

FA9550-10-1-0453

**Principal Investigator Name****The full name of the principal investigator on the grant or contract.**

Georg Raithel

**Program Manager****The AFOSR Program Manager currently assigned to the award**

Tatjana Curcic

**Reporting Period Start Date**

8/15/2010

**Reporting Period End Date**

2/14/2015

**Abstract**

Research on interactions between quantum gases and impurities (ions, other atoms etc.) has become an active area of AMO research over the past couple of years. Among the topics of interest one finds the formation of mesoscopic ions, charge hopping and quantum transport, self trapping of impurities in Bose-Einstein Condensate (BECs), and the effect of impurity particles on the BEC density distribution. To study ion-BEC interactions, a method must be used that allows one to hold a cold ion in a BEC for a sufficiently long time that these phenomena become observable, in a way that does not heat the ion.

In the project two setups have been constructed and operated towards these goals. In the first, more basic one, a metal tip (diameter 125 microns) is mounted close to a magneto-optic trap (MOT). Rydberg excitations are implanted in a cold-atom region (diameter about 10 microns, length about 50 microns). Interactions between the excitations cause excitation blockades, short- and medium-range order, as well as dynamics due to van-der-Waals interaction. All these topics have been studied. Two papers were published [one PRL, one PRA, one submitted to PRL].

The second setup is a double-trap system, in which we prepare magnetically trapped rubidium atom samples between 1 and 10 micro-Kelvin and densities of about  $10^{12} \text{ cm}^{-3}$ . We have prepared and

trapped, for the first time, cold circular Rydberg atoms in these traps. In addition to being able to study the dynamics of these highly dipolar atoms in the magnetic trap, we also observed a collision-induced loss we have traced back to collisions between the long-lived circular atoms and cold ground state atoms. These types of collisions are unexplored, to date. In this setup we also have prepared and studied D-type molecules between Rydberg and ground-state atoms. These are due to an attractive triplet s-wave low-energy scattering interaction between the Rydberg electron and a ground-state atom. We have published two papers, one in PRL, on in PRA.

#### **Distribution Statement**

This is block 12 on the SF298 form.

Distribution A - Approved for Public Release

#### **Explanation for Distribution Statement**

If this is not approved for public release, please provide a short explanation. E.g., contains proprietary information.

#### **SF298 Form**

Please attach your [SF298](#) form. A blank SF298 can be found [here](#). Please do not password protect or secure the PDF. The maximum file size for an SF298 is 50MB.

[AFD-070820-035.pdf](#)

**Upload the Report Document. File must be a PDF. Please do not password protect or secure the PDF. The maximum file size for the Report Document is 50MB.**

[AFOSR\\_Report\\_2015\\_all.pdf](#)

**Upload a Report Document, if any. The maximum file size for the Report Document is 50MB.**

#### **Archival Publications (published) during reporting period:**

[\* ] "Measurement of van-der-Waals interaction by atom trajectory imaging," N. Thaicharoen, A. Schwarzkopf, and G. Raithel (submitted to Phys. Rev. Lett., June 2015).

Posted on Arxiv.

[1] "Angular-momentum couplings in long-range Rb<sub>2</sub> Rydberg molecules," D. A. Anderson, S. A. Miller, G. Raithel, Phys. Rev. A 90, 062518 (2014).

[2] "Photoassociation of long-range nD Rydberg molecules," D. A. Anderson, S. A. Miller, and G. Raithel, Phys. Rev. Lett. 112, 163201 (2014).

[3] "Spatial correlations between Rydberg atoms in an optical dipole trap," A. Schwarzkopf, D. A. Anderson, N. Thaicharoen, and G. Raithel, Phys. Rev. A 88 , 061406(R) (2013); Editor's suggestion.

[4] "Production and trapping of cold circular Rydberg atoms," D. A. Anderson, A. Schwarzkopf, R. E. Sapiro, and G. Raithel, Phys. Rev. A 88 , 031401 (2013); Editor's suggestion.

[5] "Imaging Spatial Correlations of Rydberg Excitations in Cold Atom Clouds," A. Schwarzkopf, R. E. Sapiro, and G. Raithel, Phys. Rev. Lett. 107, 103001 (2011).

#### **Changes in research objectives (if any):**

The final results did not go as far as initially expected. Many goals were achieved, though, as evidenced by the publications.

#### **Change in AFOSR Program Manager, if any:**

None

#### **Extensions granted or milestones slipped, if any:**

There was a one-year additional funded period and a no-cost time extension.

#### **AFOSR LRIR Number**



**LRIR Title**

**Reporting Period**

**Laboratory Task Manager**

**Program Officer**

**Research Objectives**

**Technical Summary**

**Funding Summary by Cost Category (by FY, \$K)**

	Starting FY	FY+1	FY+2
Salary			
Equipment/Facilities			
Supplies			
Total			

**Report Document**

**Report Document - Text Analysis**

**Report Document - Text Analysis**

**Appendix Documents**

**2. Thank You**

**E-mail user**

Jun 09, 2015 14:49:24 Success: Email Sent to: graithel@umich.edu